Using Metamorphic Textures to Infer Deformation and Thermodynamic Histories

Kristen Elaine McCall

Thesis submitted to the faculty of the Virginia Polytechnic Institute and State University in partial fulfillment of the requirements for the degree of

Master of Science
In
Geosciences

Mark J. Caddick, Chair
Richard D. Law
Robert J. Tracy

April 23, 2014
Blacksburg, VA

Keywords: garnet, P-T conditions, chemical potential, metamorphic differentiation, Sutlej Valley

Using Metamorphic Textures to Infer Deformation and Thermodynamic Histories

Kristen Elaine McCall

Abstract

Garnet porphyroblasts are commonly used to determine P-T conditions in metamorphic rock assemblages. However, the actual process of porphyroblast nucleation is still poorly understood and garnet growth may occur at different conditions than those predicted by equilibrium thermodynamics. It is typically assumed that the Gibbs free energy of a system can be used to predict the growth of garnet at a given P and T, but here a new idea is proposed that in nature, growth does not occur until the chemical potential of each garnet-forming component departs from its equilibrium (pre-nucleation) state. Similar thermodynamic modeling results from a variety of metamorphic settings, rock types and apparent degrees of overstep indicate these deviations likely control the extent of overstep in the garnet-forming reaction in many natural samples. The process of metamorphic differentiation is then used to explain microstructures observed in the Haimanta Group, NW India that contain quartz-rich and mica-rich layers, with numerous garnet porphyroblasts appearing solely in the quartz-rich layers. This process is deformation-controlled, allowing the microstructures to be used as kinematic indicators to determine the deformation history of the Haimanta Group. The Elle Microstructural Modeling Program, the Basil deformation code and observed chemical zoning of garnets are used to prove metamorphic differentiation as the process responsible for garnet growth, meaning a singular, prograde event resulted in garnet growth in the Haimanta Group, in agreement with published monazite data for theses samples.

Acknowledgements

My interest in geology began at a very young age and I can remember collecting rocks and placing them in my rock tumbler that ran for hours in our garage, to what I can only image was my parent's immense amusement. Not coming from an area where a career as a geologist was common, I may never have become a geologist without the encouragement from my first mentor, Dr. Mark Steltenpohl, who took me on as a lab assistant after I completed his Physical Geology class at Auburn University my freshman year.

After working to digitize cross sections for a Norway mapping project, I became interested in deformation processes and how they were recorded in the rock record. This research experience, along with encouragement from Dr. Steltenpohl and support from my loving parents, led me to stop pursuing a career in corporate law and change my major to geology. Along the way I was lucky enough to receive an Undergraduate Research Fellowship to support my own trip to Norway and this experience continued to foster my interest in deformation and metamorphic processes, leading me to Virginia Tech, where I met my second mentor, Dr. Mark Caddick.

He has provided me with the freedom during my master's degree to explore my own interests in metamorphism, deformation and the linkage between the two from both a petrologic and thermodynamic aspect by allowing me to develop my own projects, with just the right amount of mentoring to help keep me on track. This has helped me to develop my own ideas, gain invaluable project management experience and truly develop as a scientist, and for this I am truly thankful.

To my other committee members, Dr. Richard "Rick" Law and Dr. Robert "Bob" Tracy, for the many useful discussions and for helping to enlighten me on numerous aspects of the geology field during my master's experience.

To Dr. Besim Dragovic, for helping with the construction and interpretation of thermodynamic models for the Sifnos samples in Chapter 2 of this thesis, useful reviews on the entirety of that chapter and for your overall good humor as a member of the petrology group.

To Dr. Greg Houseman at the University of Leeds, for taking the time to review the manuscript of Chapter 3 in this thesis and for the useful comments on the deformation modeling aspect of that chapter.

I also want to thank my boyfriend, John, who has supported me through all of my life decisions these past 3+ years. He has always encouraged me to do what is best for my future even though it has meant that the two of us have been apart for a large portion of my master's degree. I want to thank him for all he has sacrificed for our future and cannot wait to see what new adventures that future will bring.

Lastly, I want to thank my family and friends. To my parents, who have always supported and loved me through all of my life ups and downs and to my siblings, who never let me forget that I am the "golden child". To my office mates: Kristie Dorfler, Jen Gorce and Victor Guevara, for we will forever be the "Funky Bunch" and to other friends that have helped make this an amazing experience: Angela Gerhardt, Lyndsey Funkhouser and Hannah King.

Attributions

Chapter two will be submitted for publication in the Journal of Metamorphic Geology as "McCall, K.E., Caddick, M.J., and Dragovic, B. Chemical Potentials: the Key to Unlocking the Conditions of Garnet Nucleation?" K.E. McCall is responsible for all phase diagram calculations and the associated chemical potential and volume percent difference traverses. M.J. Caddick and B. Dragovic aided in thermodynamic modeling construction and interpretation of model results. K.E. McCall wrote the manuscript and drafted all of the figures.

Chapter three may be submitted for publication to a journal in the future as "McCall, K.E., Caddick, M.J., and Law, R.D. Metamorphic Differentiation of the Haimanta Group Metasediments, Sutlej Valley, northwestern India: Implications for Microstructural Evolution" K.E. McCall is responsible for all deformation models and chemical zoning maps. M.J. Caddick collected samples in the field and provided assistance with figures pertaining to geologic setting and sample description. R.D. Law assisted with stress value calculations and interpretation. K.E. McCall wrote the manuscript and drafted the remaining figures.

Table of Contents

List of Figures

CHAPTER 2

CHAPTER 3

APPENDIX

List of Tables

CHAPTER 2

CHAPTER 3

CHAPTER 1

Introduction to Garnet Crystallization Mechanisms

McCall, K.E.

1. Introduction

Garnet porphyroblasts are important because they occur in a wide variety of metamorphic terranes, covering an array of metamorphic conditions, and because element diffusion within them is often slow enough to preserve growth-zoning patterns. This allows garnet crystals to be useful tools in determining pressure-temperature (*P*-*T*) conditions during metamorphism and associated deformation. However, progressive changes in mineralogy during metamorphism often do not mimic spatial changes. For example, the idealized Barrovian sequence is not always followed in nature (e.g. isograd sequence and spacing may be contrary to expectations) and the effects of external fluids, diffusion and deformation can all act to complicate our reading of the metamorphic history of a given sample. A major goal of the projects within this thesis is to determine the linkage between those parameters that control metamorphic texture (focusing on garnet nucleation and growth) so that garnets can better be utilized as indicators of *P*-*T* histories in metamorphic rocks.

Porphyroblast nucleation has previously been shown to require a departure from thermodynamic equilibrium, but the specific mechanisms controlling this departure are still poorly understood. The method presented in Chapter 2 outlines the novel use of an equilibrium thermodynamics-based modeling program (Perple_X) to predict where in pressure-temperature space initial garnet growth occurs by focusing on the chemical potentials of the individual major garnet-forming oxides (μ_{Al2O3}, μ_{CaO}, μ_{FeO}, μ_{MgO}, μ_{MnO}). It is proposed that although the overall Gibbs free energy of the system can predict the stability of garnet at a given P and T, nucleation does not occur in nature until the chemical potential of each garnet-forming component departs from its equilibrium (pre-nucleation) state.

The diffusion of components from grains in the surrounding matrix to the growing (nucleating) crystal is commonly thought of as a controlling factor for porphyroblast growth because a crystal cannot grow until all of the necessary components have reached it from the surrounding matrix. This process is dependent on the concentration gradients of *all* diffusing components in the chemical system, and in Chapter 2 it is proposed that because diffusion is controlled by chemical potential gradients, an understanding of the differences in chemical potentials that develop if garnet nucleation is suppressed can lead to a better understanding of the conditions required for initial growth of garnet. The interdependence of components in the

diffusion process is similar to the driving force for the metamorphic differentiation process studied in Chapter 3, wherein the mean stress on a grain is dependent on the strength of the surrounding grains.

In Chapter 3, a group of thin sections taken from the Haimanta Group, NW India (Himalaya), were studied in attempts to determine the microstructural evolution of samples that contain prominent quartz-rich and mica-rich layers, with numerous garnet porphyroblasts appearing solely in the quartz-rich layers. A common assumption in metamorphic petrology is that porphyroblasts form in nutrient-rich areas in their host rock and these microstructures appear to contradict to this assumption (and must therefore be explained). It is proposed that these microstructures preserved in the Haimanta Group metasediments formed during the metamorphic differentiation process, with garnet growth resulting from the release of strain energy housed in the crenulated (S_1) foliation as the new, axial planar (S_2) foliation developed. The model results in Chapter 3 provide evidence of the stress differences that theoretically drive the metamorphic differentiation process and also show that heterogeneities in strain rate and dislocation density arise across the modeled microstructure upon deformation. These heterogeneities are then interpreted to represent areas with different growth potential for garnet nucleation.

The free energy of a metamorphic reaction (e.g. garnet growth) can be described by the relationship ($\Delta G = V\Delta P - S\Delta T$) and equilibrium thermodynamics predicts that reaction will occur when the free energy change (ΔG) associated with formation of product phases is negative. In Chapter 3 it is theorized that the areas in a microstructure with the largest values of strain rate and dislocation density, interpreted to have the largest nucleation potential, should be represented by mica-rich fold hinges in the crenulating foliation. At these points the release of strain energy during the (S_1-S_2) foliation transition should lead to the highest growth potential for garnet crystals, consistent with textures preserved in the Haimanta Group samples.

The material presented in the Appendix of this thesis is in accordance with the same goal presented for Chapters 2 and 3 of using equilibrium thermodynamics-based models to better understand the mechanisms controlling garnet growth. The specific microstructural simulation presented in the Appendix was created to study the garnet-biotite (Fe-Mg) exchange reaction, with a goal of simulating the breakdown of garnet (using the exchange reaction) to better understand the diffusion processes occurring after porphyroblast nucleation. These models assume that the observed diffusion mechanisms should be similar to the processes controlling the

diffusion of components to the growing (nucleating) crystal. The model and results were not included as a major chapter in the thesis because the experimental results do not contribute significantly to the understanding of diffusion processes, but are included in the Appendix because they contain a more detailed outline of the Elle Microstructural Modeling program that was also used to model the evolution of the simulated microstructure in Chapter 3.

CHAPTER 2

Chemical Potentials: the Key to Unlocking the Conditions of Garnet Growth?

McCall, K.E., Caddick, M.J., and Dragovic, B.

Abstract

Porphyroblast nucleation has previously been shown to require a departure from thermodynamic equilibrium, but the specific mechanisms controlling this departure are still poorly understood. Here we examine the role of chemical potentials of individual components that combine to nucleate a garnet crystal and propose that although, as typically assumed, the overall Gibbs free energy of the system can predict the growth of garnet at a given P and T, nucleation does not occur until the chemical potential of each garnet-forming component departs from its equilibrium (pre-nucleation) state. Previous studies have looked at barriers to nucleation from a cumulative free energy standpoint, rather than this element-by-element basis.

We use published garnet crystal core compositions to determine the P-T at which garnet nucleated and thermodynamic modeling to examine the energetic consequences of suppressed nucleation. Samples were chosen from areas with a previously reported significant degree of reaction overstepping: two regionally metamorphosed terranes (Pomfret Dome, VT and Central Maine Belt, ME), one contact aureole (Nelson Aureole, B.C.) and one paleo-subduction terrane (Cycladic Blueschist Unit, Sifnos). Two isochemical phase diagrams were calculated for each sample, one allowing all phases to form and a second arbitrarily prohibiting garnet (and staurolite where applicable). Chemical potential and phase abundance differences between each were then examined. Results routinely show that a deviation in the chemical potentials of *all* garnet-forming elements does not occur at the equilibrium garnet-in reaction, but instead coincides with the P and T of inferred crystal growth (based on the garnet core composition). Our models produced similar results over a wide variety of metamorphic settings, rock types, and apparent degree of overstep, indicating that these deviations likely controlled the extent of overstep of garnet-forming reactions in many natural samples.

1. Introduction

Progressive changes in mineralogy upon metamorphism often do not mimic spatial changes, but is there a way we can determine a linkage between the two and define accurate P-T-t paths for metamorphic events with only equilibrium thermodynamics as our model base? The primary goal of this paper is to use thermodynamic modeling to determine the P-T conditions

during the first recorded garnet growth. Our focus is specifically on the role of chemical potentials in the garnet growth process and we attempt to use them to predict where in P-T space growth occurs in a wide variety of geological settings.

To identify metamorphic reactions, the current energy state is compared with the equilibrium state and the reaction is predicted to progress in the direction that lowers the system's Gibbs free energy (Bons et al., 2008). However, one of the main difficulties in using thermodynamics to model metamorphic reactions is that they are, by definition, the result of a non-equilibrium stage in the development of the rock. In porphyroblast-forming reactions, there is often a buildup in energy that develops between the thermodynamically stable, but not yet crystallized products and the metastable reactants. This energy, termed "reaction affinity", is a function of the thermal overstep (in temperature, ΔT) and the difference in entropy (ΔS) between the two states. Therefore reactions that release large quantities of H_2O, e.g. chlorite-consuming (garnet-forming) reactions involve a higher entropy change per unit of temperature overstep and therefore have larger values of reaction affinity (Pattison and Tinkham, 2009; Carlson, 2011). Nucleation rates are known to increase exponentially with the degree of thermal overstepping of the reaction (Carlson, 1999) and here we focus on the overstepping of the equilibrium predicted garnet-forming reaction boundary in an attempt to understand the processes controlling these exponential increases in nucleation rates (greater probability of garnet nucleation) with the degree of thermal overstepping.

It is well documented that a departure from equilibrium is required to gain energy for the formation of the interface between reactants and products (Volmer and Weber, 1926; Gibbs, 1928; Kaischew and Stranski, 1934; Winter, 2010; Gaidies et al., 2011). This nucleation difficulty is known to be an important and possibly leading cause of reaction overstepping in metamorphic systems (Rubie, 1998; Waters and Lovegrove, 2002; Pattison and Tinkham, 2009), but the specific mechanisms controlling these departures are still poorly understood. In metamorphic environments, mechanisms of nucleation and growth are sometimes incapable of keeping pace with heating rates (Fisher, 1978; Joesten and van Horn, 1999; Waters and Lovegrove, 2002; Pattison and Tinkham, 2008; Carlson, 2011), suggesting that the input of thermal energy into a deforming system is rarely the rate-limiting factor in contact metamorphism and often in regional metamorphism as well. Instead, because of the exponential

response of crystallization rate to thermal overstepping, the most fundamental control on the rate of prograde metamorphism is the rate of temperature increase (Carlson, 2011).

The equation describing the magnitude of the energy barrier to nucleation, referred to as the "critical energy barrier" that must be overcome to form a nucleus is described by the equation: $\Delta G^* = [16\pi\nabla^2\sigma^3/3(\Delta G_v)^2]$ (Gaidies et al., 2011). The term ∇ is the volume of a garnet molecule, σ the isotropic interfacial free energy per unit of interfacial area, and ΔG_v, the maximum volumetric Gibbs free energy difference between the reactant and product phase or the chemical driving force. While this equation exists, the actual magnitude of the critical energy barrier (ΔG^*) is not a constant for any specific metamorphic reaction. Equilibrium thermodynamics can thus be used as the template to derive an equation used to describe the behavior of rocks and the formation of new minerals, but the actual process and amount of overstepping necessary to achieve the departure from equilibrium to form a new crystal is still unknown.

Gaidies et al. (2011) mentions that chemical potential differences ($\Delta\mu$) at the garnet-matrix interface are required for trans-interface interdiffusion driving crystal growth (Hillert, 1999; Hillert and Rettenmayr, 2003), or that the $\Delta\mu$ of one component must be different than the $\Delta\mu$ of another component in the system in order to drive diffusion. Our simulations aim to look at the buildup in Gibbs free energy necessary to induce nucleation from a chemical potential standpoint (the free energy associated with the addition of one mole of a component/oxide to the developing system). This is different from the work done by others (e.g. Gaidies et al., 2011; Pattison et al., 2011; Pattison and Tinkham, 2009; Waters and Lovegrove, 2002), that looked at barriers to nucleation from a whole-rock free energy standpoint. Our goal is to use the difference in free energy of individual components that come together to nucleate and grow a garnet porphyroblast, represented by the chemical potentials of the major garnet forming oxides (Al_2O_3, CaO, FeO, MgO and MnO), as a proxy for the energy barrier to nucleation. We propose that although the overall Gibbs free energy of the system may be such that equilibrium thermodynamics predicts the growth of a garnet porphyroblast [$\Delta G_{reaction} = < 0$], nucleation does not occur in natural samples until the chemical potential of each garnet-forming oxide departs from its equilibrium (pre-nucleation) state.

2. Chemical Potentials: Why They May Be Better Indicators of the P-T Conditions of Garnet Growth

Gibbs free energy is defined by the sum of the chemical potentials contributed by each of the components (oxides) in a system. In the case of transient chemical potential gradients, the transformation of a given volume of rock from one equilibrium state to another involves an intermediate disequilibrium state, driven by the fact that such mineral transformations and diffusion cannot be instantaneous (Carmichael, 1969; Foster, 1986; Carlson, 2002; White et al., 2008b). Our study focuses on determining the conditions (P and T) during the first garnet growth event recorded along the prograde metamorphic path. Delayed porphyroblast nucleation is a commonly observed phenomenon in prograde metamorphism because porphyroblasts usually nucleate and grow distal to reactant phases, resulting in chemical potential gradients between where the new minerals are, and distal to them (White et al., 2008a).

Decrease of the total system free energy is achieved through the migration (diffusion) of a component with a large chemical potential and addition of it to a phase with a small chemical potential. A final equilibrium state is reached when there are no remaining gradients in chemical potential. This can involve the partial breakdown of a phase in which chemical potential of a component is higher than in the equilibrium condition, resulting in a decrease of the total free energy in the system. If a new mineral does not nucleate with increasing P-T conditions, the new equilibrium will be a metastable one and minerals in the assemblage will no longer be in equilibrium with each other as chemical potential gradients are established between them (Stipska et al., 2010). These gradients then drive diffusion and often result in metamorphic reaction(s), as the system attempts to flatten chemical potential gradients. In fact, the defining 'characteristic' of diffusion-controlled nucleation and growth (DCNG) crystallization is the presence of local gradients in the chemical affinity (energy) for the garnet-forming reaction within the intergranular medium around growing crystals (Carlson, 1999). This is unlike interface-controlled nucleation and growth (ICNG), that assumes rapid diffusion precludes the development of any appreciable gradients in intergranular concentration, resulting in a spatially uniform intergranular medium and a uniform distribution of potential nucleation sites throughout the matrix (Carlson, 2011). Petrologic evidence for diffusion-controlled growth is also commonly observed in the spatial ordering of phases (Chernoff and Carlson, 1997; Carlson,

1999; Hirsch and Carlson, 2006; Carlson, 2011). If diffusion controls the resultant metamorphic textures that develop from changing P-T conditions and this diffusion is controlled by chemical potential gradients, then by understanding the differences (buildups) in chemical potential that develop when garnet nucleation is suppressed, we should be able to understand the driving force for garnet nucleation.

In a multi-component system, such as that of a deforming rock body, the diffusive flux of any component does not only depend on its own concentration, and thus its chemical potential gradient, but also on those of *all* other diffusing components (Ganguly, 2002). This is because in an n-component system of fixed mass and volume, the concentration of one component is fixed by those of others at any given point (Ganguly, 2002). While this theory is accepted in terms of volume diffusion within a crystal, the diffusional controls in the surrounding grain boundary network (i.e. matrix), are still relatively unknown. Carlson (2011), however, states that the rate of porphyroblast growth is limited by the component that exhibits the lowest diffusive flux. Specifically, here we are focusing on the diffusion of components from grains in the surrounding matrix to the growing (nucleating) crystal. By using a thermodynamic modeling program such as Perple_X (Connolly, 1990; Connolly and Petrini, 2002) we can study the interaction of the chemical potentials of all thermodynamic components involved in the formation of a garnet crystal and hopefully gain new information about the energetic changes necessary to nucleate and grow a new crystal.

Chemical potential differences have been used in the past to schematically describe the Gibbs free energy that builds up during the formation of a garnet porphyroblast (Gaidies et al., 2011; Pattison et al., 2011), but to our knowledge no one has looked at the individual values of component-specific chemical potential differences and how they relate to the P and T of porphyroblast growth. Our hope is that the calculated chemical potential differences will parallel the chemical potential differences developed in natural samples during nucleation suppression and relate to the energetic controls on the delayed growth of garnet porphyroblasts often observed in nature. The energy that builds up when nucleation is suppressed is represented in the following thermodynamic models by the chemical potential differences of the major garnet forming oxides between a system where porphyroblast phases are allowed to grow and a system in which garnet is prohibited from forming. By studying these energetic deviations we hope to learn more about the driving force(s) for this nucleation suppression. We theorize that garnet

nucleation cannot occur in nature until all components needed to create the mineral are present, so if diffusion of the slowest species controls when nucleation occurs, because diffusion is driven by chemical potential gradients, nucleation cannot occur until the last major garnet-forming oxide experiences a change in chemical potential.

Gibbs free energy versus composition diagrams, often referred to as "G-X diagrams", are used in petrology to show stable mineral assemblages based on Gibbs free energy minimization. Each mineral has a potentially complex G-X curve and the tangent to the curves with the lowest energy configuration is used to determine the stable mineral assemblage. Scenario 1 (Figure 2.1) represents a simple, two component system that according to the phase rule should have a resulting two stable phases (Garnet and Mineral 2). This diagram displays for a simple system how Perple_X (Connolly, 1990; Connolly and Petrini, 2002) and other thermodynamic modeling programs calculate phase diagrams for more complicated systems (more components and phases) across a range of pressures and temperatures. These diagrams schematically depict the two scenarios that can arise when garnet is excluded from the stable mineral assemblage and demonstrate the rationale for the method applied in the following figures. In Scenario 1 (Figure 2.1) when garnet is excluded from the stable mineral assemblage, a new mineral is predicted to become stable in its place, resulting in a new energy configuration and change in chemical potential values as indicated by the new (black) vs. red dashed (old) tangent positions. Scenario 2 (Figure 2.1), displays a system wherein no new mineral become stable to replace garnet, but there is still a shift in energy because of a change in the amount of the two remaining phases (more of Mineral 1 and less of Mineral 2). This scenario is diagrammatically more difficult to portray because if a phase is removed from the system and no new mineral becomes stable in its place, in order to display the G-X diagram in an equilibrium configuration, a variable must be added (P, T), or a component removed from the diagram (because once garnet is removed, phases $\neq$ components). In this example μ_{MnO} was removed, reducing this system from a three component to a two components system so that phases = components.

Our method utilizes published garnet crystal core compositions to determine the P and T at which garnet growth occurred and thermodynamic modeling to calculated phase diagrams allowing and excluding garnet (and staurolite where applicable). We then used this information to construct traverses of the difference in chemical potential and phase abundances between each calculation to examine the energetic and petrologic consequences of suppressed garnet

nucleation. Some limitations of this method are that it relies on numerous assumptions, first that that the garnet core chemistry used to determine the P-T conditions of garnet growth records the geometric core of the crystal (nucleus) and the true nucleation conditions of the crystal, that the bulk rock composition used for the phase diagram calculations accurately represents the chemical system the rock grew from, and closed system behavior with H_2O present in excess. Furthermore, the mixing models used for each phase diagram calculation are assumed to be a true representation of the mineral compositions present in the environment garnet nucleated in and the effects of compositional variation between phases present in the allowed versus excluded phase diagrams on this environment is assumed to be minimal.

3. Sample Choices and Overstep Parameters

Sample choices were made based on published data in areas known to have a significant degree of overstepping involved in the formation of porphyroblasts and with published core garnet and bulk rock compositions in order to determine the P-T conditions of garnet growth. We are cognizant of the fact that there could be other potential nucleation events not recorded by core data used for this study due to only sampled garnets being considered when determining nucleation conditions. Different metamorphic terranes were used to ensure that the relationship of chemical potential differences to the predicted garnet growth conditions were representative of a natural process occurring in a wide variety of metamorphic settings. Sample choices include two regionally metamorphosed terranes (Pomfret Dome, VT and Central Maine Belt, ME), one contact aureole (Nelson Aureole, B.C.), and one paleo-subduction terrane (Cycladic Blueschist Unit, Sifnos). The addition of the Sifnos, Greece samples added in an additional rock type to be considered for these calculations, as all samples except those from Sifnos are pelitic assemblages, while the samples from Sifnos are mafic blueschists, likely from an altered basaltic protolith (Dragovic et al., 2012).

The samples from the Central Maine Belt are ideal examples to explore the relationship of chemical potential buildups and garnet growth conditions because this thrust system experienced deformation, plutonism, and metamorphism contemporaneously (Solar et al., 1998; Solar and Brown, 2001a, b; Sanislav and Bell, 2011) meaning a single garnet growth period should be recorded. Sanislav and Bell (2011) report garnet growth is overstepped by up to 100

°C and that the episodic nature of garnet growth did not result from the effects of bulk composition on mineral stability fields, but instead was controlled by the manner in which deformation partitioned through the outcrop. Furthermore, the samples are reported to preserve typical growth zoning for a pelitic garnet that grew during prograde metamorphism (Hirsch et al., 2003; Sanislav and Bell, 2011) and thus the core composition should preserve the chemistry at the time of garnet growth.

The tectonic history for the Pomfret Dome samples is unique in that garnet growth was not only overstepped in temperature, but also in pressure. This stratigraphic sequence experienced such thick thrust loading that the first schistosity, and resulting porphyroblast nucleation and growth, did not develop until a depth of 20 km (Bell et al., 2013) or pressures between 6 and 8 kbar, as indicated by the intersection of the garnet core chemical isopleths values. The presence of overthickened thrust sheets suppressing the effects of deformation (i.e. porphyroblast growth) is not unique to these samples and is also reported by (Laubach and Diaz-Tushman, 2009) wherein thrust sheets between 8 and 12 km thick are reported to leave the sediments below undeformed. Further evidence that the overstepping associated with the Pomfret Dome samples is the result of deformation is verified by the CaO contents. Low CaO contents mean that overstepping is unlikely to have resulted from a change in bulk composition due to carbonate or plagioclase loss through dissolution, solution transfer, and volume loss accompanying foliation development (Bell and Bruce, 2006, 2007; Bell et al., 2013).

In the two study areas containing regionally metamorphosed rocks, the Central Maine Belt and Pomfret Dome samples (Sanislav and Bell, 2011; Bell et al., 2013), porphyroblast growth is interpreted to occur during crenulation of a previously developed foliation that lies at a high angle to the newly developing foliation (Bell and Hayward, 1991), preserved in the measured Foliation Intersection/Inflection Axes (FIAs). This petrologic observation is important for our study because no porphyroblast growth should occur during the re-use of a pervasively developed foliation due to the fact that crenulations do not develop; implying later stages of deformation should not result in new garnet growth. The preserved core garnet chemistry should thus preserve the initial conditions of garnet growth and no later growth should be present in these samples to invalidate this theory. Furthermore, in samples from the Pomfret Dome, garnet growth is reported to have occurred for the first time in only one of the five FIA sets measured

from the area (Bell et al., 2013), further evidence that these samples record only a single period of garnet growth and hence a single P and T of garnet nucleation.

Samples from the Nelson Aureole were chosen along two transects (B and D) described by Pattison and Vogl (2005) and Tomkins and Pattison (2007). Along both transects, garnet porphyroblasts appear to have experienced delayed nucleation until temperatures coincident with those of the higher temperature porphyroblast phases, as indicated by the sequence of mineral-in isograds within the aureole and the textures and chemical zoning reported for samples within the aureole suggesting no garnet dissolution (Pattison and Tinkham, 2009). Garnet porphyroblasts from Transect B occur as euhedral crystals in both andalusite inclusions and in the matrix, suggesting that garnet was not involved significantly in the modal changes associated with the development of andalusite and sillimanite (Pattison and Vogl, 2005). Garnet porphyroblasts from Transect D appear to have behaved as a passive phase that was not involved significantly in the development of staurolite due to the lack of observed dissolution, even though garnet is predicted to dissolve significantly during staurolite production (Pattison and Tinkham, 2009).

Garnets from the Cycladic Blueschist Unit from the island of Sifnos were chosen as the subduction zone example to test this method because they are the first subduction-zone garnets that have been dated from core to rim (Dragovic et al., 2012). For the geochronology work, chemically contoured microsampling of crystals was performed using the methods outlined in Pollington and Baxter (2011) to ensure the geometric centers of each garnet were within the sampled wafer. This method, similar to the FIA method described above, allowed for the core isopleth values used in our study to be representative of the true crystal core chemistry of each garnet porphyroblast. Furthermore, core to rim transects of spot analyses of the Ca, Fe, Mg and Mn concentrations across Sifnos sample 06MSF-6C imply undisturbed prograde growth for the garnet with no significant diffusive re-equilibration (Dragovic et al., 2012). This observation gives confidence regarding our assumption that although the Sifnos samples underwent exhumation, the core garnet chemistry can still be used to accurately deduce the P-T conditions of garnet growth.

4. P-T Phase Diagram Calculations

In order to make accurate predictions from phase diagrams, the bulk composition used for modeling must equal the effective composition that the preserved texture (mineral assemblage) grew from. An assumption made in this paper is that all of the bulk rock data taken from published literature and used for the following thermodynamic models was in agreement with this principle. Pressure-temperature phase diagram calculations were modeled to be as close as possible to the published data for samples using the thermodynamic modeling program Perple_X (Connolly, 1990; Connolly and Petrini, 2002). Published thermodynamic modeling data (if any) for each sample and the chemical system, mixing models, and P-T constraints used for phase diagram calculations for this paper are summarized in Table 2.1 and whole rock compositions and garnet core chemistries used for core isopleth calculations are listed in Table 2.2, according to data found in Bell et al. (2013); Dragovic et al. (2012); Sanislav and Bell (2011) and Tomkins and Pattison (2007).

To be in agreement with the observation of ilmenite in the Nelson Aureole samples and with other published thermodynamic models of samples from the aureole, reported by Pattison and Tinkham (2009) in phase diagrams of the average Nelson Aureole metapelite, the ilmenite (*ideal) mixing model was added (Table 2.1) and to accompany the addition of ilmenite, TiO_2 was added to the chemical system (Table 2.2). Our calculations differ from those presented by Pattison and Tinkham (2009) in that we consider margarite as a component in white mica in order to model as closely as possible the natural system.

In the phase diagrams calculated for each sample, first a calculation was made allowing formation of all phases as described above for each sample. Following this, another calculation was made excluding the garnet (and staurolite where applicable) end members from the stable mineral assemblage (abbreviated in the Perple_X input file as: spss, alm, gr, py, mnst, mst, fst). By excluding these end members from forming, we are, in essence, calculating metastable phase diagrams to determine the energetic driving force for the garnet-forming reaction. The exclusion of only the garnet (and staurolite where applicable) end-members limits this method to accurately addressing only chemical potential differences up to the stability fields of higher temperature and pressure porphyroblast phases (e.g. the Al_2SiO_5 polymorphs and cordierite). Therefore these calculations are limited to the P-T conditions prior to values within the predicted

stability fields of these phases and the P-T paths (traverses) for each sample thus end after the equilibrium predicted staurolite-in P and T (or at the stability field following the chemically predicted garnet-in P and T). This is unlike the calculations made by Pattison and Tinkham (2009) who excluded all high temperature phases from forming in order to calculate reaction affinity maps. We acknowledge that if garnet (and staurolite where applicable) are excluded from forming, over time as pressure and temperature increase new phases will be predicted to be stable as new stability fields are encountered, but because these higher pressures and temperatures are not reached at the inferred conditions of garnet growth, we chose not to exclude other high-temperature phases in our calculations.

Compositional changes arise between minerals present in the two phase diagram calculations for the allowed and excluded systems. These compositional differences are small for chlorite and biotite (Table 2.3), two of the major phases that break down to form garnet and therefore we assume that these compositional changes should have little effect on the accuracy of this method to thermodynamically predict the conditions during garnet nucleation.

4.1 Garnet Core Isopleth Calculations

In garnets, diffusion of major elements is slow enough to preserve growth-induced zoning until moderate grades of metamorphism are achieved (Loomis, 1983; Elphick et al., 1985; Carlson, 2006). A major assumption in this paper is that the composition of each sampled crystal has not been significantly modified by diffusion subsequent to its crystallization (Chakraborty and Ganguly, 1992). This assumption implies that the garnet core composition is in equilibrium with the whole rock composition used for thermodynamic modeling and based on a specific whole rock composition, the core chemistry of a garnet can be used to calculate the precise P-T conditions of garnet growth (Tinkham and Ghent, 2005a) using the intersection of the core isopleths of X_{Grs}, X_{Alm}, X_{Sps} (Vance and Mahar, 1998; Spear et al., 2002; Evans, 2004; Tinkham and Ghent, 2005b; Cihan et al., 2006; Sayab, 2007; Chambers et al., 2009; Ali, 2010; Sanislav and Bell, 2011; Dragovic et al., 2012; Bell et al., 2013). Hereafter, this will be referred to as the ***"chemical-in"*** or the chemically predicted garnet growth P and T.

The Nelson Aureole samples are the only samples used in this study with no published information from the authors to ensure that the exact crystal core chemistry was measured;

therefore we chose to use the core isopleth intersections (excluding X_{Grs}, if too small to contour for) in conjunction with pressure estimates for the transect each sample was taken from based on Figure 3 in Tomkins and Pattison (2007) to determine the P-T conditions of garnet growth. A pressure of 4.0 kbar was assumed for samples from Transect D (03-CW-04A, 93-CW-23) and 3.5 kbar for Transect B (03-OC-04). Furthermore, published data on the Ca concentrations in Nelson Aureole garnets suggests calcium zonation that appears to be inconsistent with the other major oxide zonation patterns, possibly implying this element preserves thin-section scale disequilibrium (Spear and Daniel, 2001; Hirsch and Carlson, 2006; Pattison and Tinkham, 2009). We acknowledge the potential disequilibrium between major oxide chemistry for these samples and while core isopleth intersections are included on Figures 2.8, 2.9, and 2.12, they may not be an accurate representation of the P-T conditions during garnet growth.

4.2 Comparisons of Calculated Phase Diagrams with Published Work

Phase diagrams for the Central Maine Belt samples reported by Sanislav and Bell (2011, using Thermocalc [Powell and Holland, 1988]) do not include a feldspar phase (Figure 8, Sanislav and Bell, 2011), although the paper reports plagioclase was considered as a phase for thermodynamic modeling. The phase diagrams we calculated for the same samples include albite at low temperatures and plagioclase and potassium feldspar at high temperatures (Figures 2.2 and 2.5). This omission of a key mineral in their phase diagram calculations explains the differences in pressures of the "chemical-in" between our calculations and the ones presented in their paper. Differences in pressure of roughly 2.0 kbar for core isopleth pressure estimates (IS2, Figure 2.2: **5.1 kbar** and 549 °C vs. **3.8 kbar** and 545 °C and IS95, Figure 2.5: **5.4 kbar** and 540 °C vs. **3.2 kbar** and 535 °C) are most likely due to some of the calcium going into forming plagioclase in our calculations, making garnet stable at higher pressures then predicted in the phase diagrams published by Sanislav and Bell (2011).

Bell et al. (2013) report all garnet porphyroblasts around the Pomfret Dome to have first nucleated at 535 °C ± 25 °C and 6-8 kbar for every FIA set. Our isopleth values indicate for sample AV29, garnet nucleation occurred at 6.5 kbar and 527 °C (Figure 2.6) and for sample V396, at 6.2 kbar and 528 °C (Figure 2.7). We attribute the close match of our calculated P-T conditions of garnet nucleation with those of Bell et al. (2013) for the Pomfret Dome samples in

comparison to core isopleth estimates for the Central Maine Belt samples to the inclusion of feldspar in their calculated phase diagrams (Figure 6, Bell et al., 2013), unlike those of Sanislav and Bell (2011).

The difference in the geometry of the Pomfret Dome phase diagrams presented in this paper and those published by Bell et al. (2013) using the same mixing models is most likely the result of Holland and Powell's "Equipartition Constraint" (http://www.perplex.ethz.ch/perplex_updates.html). These differences arise because of the way Fe and Mg partition between muscovite, biotite, chlorite and garnet in Thermocalc versus Perple_X. A consequence of this is that the mineral assemblage stability fields calculated for Fe-bearing systems are not consistent between the two programs. Because of the excellent match of the estimated P-T conditions of garnet growth when using Perple_X and Thermocalc for the Pomfret Dome samples we conclude that the geometric differences in phase diagrams do to not affect the overall thermodynamic information that can be deduced from the phase diagram calculations for the purposes of this study.

4.3 Chemical Potentials and Phase Proportions along P-T Paths

Traverses along a 1-D path in P-T space were made for each sample using the two phase diagrams calculated for each chemical system in order to analyze differences between the two systems graphically. Traverses were calculated by subtracting values of the system wherein garnet (and staurolite where applicable) were excluded from the stable mineral assemblage from the calculation where all phases were allowed to form. The P-T path for each sample was determined based on the published tectonic and thermal history described in the literature for each sample. For the Central Maine Belt and Nelson Aureole samples, isobaric traverses were applied to be in accordance with the observed overstep in only temperature at a relatively constant pressure during garnet growth. For the Sifnos and the Pomfret Dome samples, loading traverses were applied in order to better replicate the temperature and pressure overstep associated with the formation of garnets.

Traverses of chemical potential differences between the two phase diagrams were calculated for each of the major garnet-forming oxides (μ_{Al2O3}, μ_{CaO}, μ_{FeO}, μ_{MgO}, μ_{MnO}) and normalized to the mol% of each oxide in the system along the specified traverse. The chemical

potential of SiO_2 was not considered because although it is a major garnet-forming oxide, the chemical potential of SiO_2 is fixed in the system as quartz is in excess, meaning the difference in chemical potential of SiO_2 would always be zero for our calculations. Traverses of volume percent differences in phases only include phases that experienced a change along each traverse (increased or decreased in abundance). For one sample, (IS2), diagrams were created to show the difference in certain system properties (discussed above, with the addition of Gibbs free energy and entropy) over the entire P-T interval used for the phase diagram calculation.

5. Results and Discussion

The figures presented for each sample include the phase diagram with no excluded phases, showing the stable mineral assemblage based on the bulk rock chemistry over a specific P-T interval with a traverse imposed on each that intersects the chemically predicted garnet growth P-T conditions, "chemical-in", based on the intersection of the garnet core isopleth values (Table 2.2). Along each traverse there are two plots, the top showing the difference in chemical potential ($\Delta\mu$) of the major garnet-forming oxides and the bottom showing the difference in volume percent of phases between the two phase diagram calculations. On both traverses, the position of the equilibrium predicted garnet growth P-T conditions ***"equilibrium-in"*** and the chemically predicted garnet growth P-T conditions ***"chemical-in"*** are denoted by dashed lines. The numbered boxes refer to the numbered stability fields on the traverse for each phase diagram. The equilibrium predicted staurolite-in P-T is included on the traverse and phase diagram (yellow line) if it is intersected during the respective P-T interval for each sample.

Chemical potential is a measure of the free energy change associated with the gain or loss of one mole of a specific element (oxide) to a chemical system. A positive chemical potential difference ($\Delta\mu_{component} > 0$) in the following traverses (i.e. Figures 2.2, 2.5-2.12), indicates that adding one mole of that component to the system wherein porphyroblast phases have been excluded should contribute less to the total system free energy and thus be more energetically favorable in the system. This is due to a more negative free energy value for the component in the system wherein porphyroblast phases have been excluded than in the system where porphyroblast phases were allowed to form. A negative chemical potential difference of a component ($\Delta\mu_{component} < 0$), indicates that the component should contribute more to the total

system free energy (due to a less negative free energy value) in the system wherein porphyroblast phases were excluded from the stable mineral assemblage and thus be less energetically favorable. Any Δμ values should be zero before the "equilibrium-in" reactions because before these conditions, the energetic configuration of each system is identical. After the conditions of the garnet-in reaction, as predicted in the system where porphyroblast phases are allowed as part of the stable mineral assemblage, the two systems begin to differ. The chemical potential difference (Δμ) for the MnO component ($\Delta\mu_{MnO}$) acts as the major indicator of when this boundary has been crossed because MnO has a large affinity for garnet and when this mineral is not allowed as part of the stable mineral assemblage, the ($\Delta\mu_{MnO}$) between the two systems is always negative. This negative chemical potential difference ($\Delta\mu_{MnO} < 0$), after the "equilibrium-in" conditions have been overstepped, indicates that MnO is less energetically favorable in the system where porphyroblast phases have been excluded from the stable mineral assemblage (Figure 2.2 and 2.3f).

A positive volume percent difference in a phase means that less of a phase is predicted to be stable when porphyroblast phases are excluded from the stable mineral assemblage (e.g. biotite at the staurolite-in line, Figure 2.2 and 2.4c). The opposite is true for a negative volume percent difference, meaning that more of a phase is predicted to be stable if porphyroblast phases are excluded from the stable mineral assemblage (e.g. chlorite, Figure 2.2 and 2.4d). The volume percent difference in chlorite is negative for every calculation because chlorite is one of the main minerals that breaks down to form garnet and when this was prohibited from happening, more chlorite was predicted to be stable in the excluded phase diagram calculation, resulting in a negative volume percent difference.

In Figures 2.3 and 2.4, the changes in certain system properties over the entire P-T interval used to calculate the phase diagram for sample IS2 are displayed. These P-T maps are similar to those published by Pattison et al. (2011) and are presented with a goal of highlighting the fact that although the traverses imposed for each sample only focus on a narrow P-T interval, the changes observed at the "chemical-in" are present in the entire system and not just in the narrow interval highlighted in the following figures. Furthermore, these diagrams are presented to show the limitations of this method. For this particular sample, after the conditions of the equilibrium predicted staurolite-in reaction (Figure 2.3a, field 8) have been reached, the difference in total system Gibbs free energy (ΔG) reduces towards zero. This is because at higher

temperatures, new minerals are predicted to be stable (e.g. the Al_2SiO_5 polymorphs), that were not included as porphyroblasts phases in the excluded calculation. Therefore, at the conditions these minerals are predicted to be stable represent the conditions this method loses its ability to accurately predict energetic and volume percent differences between the two systems.

In Figure 2.3a, there is an exponential change in ΔG that is coincident with the position of the "chemical-in". The positive ΔG at this point indicates that the total system Gibbs free energy is more negative if porphyroblast phases are excluded from the stable mineral assemblage. The chemical potential difference diagrams of $\Delta\mu_{Al2O3}$, $\Delta\mu_{FeO}$, and $\Delta\mu_{MgO}$ (Figure 2.3b,d,e) follow the same pattern, but the diagrams for $\Delta\mu_{CaO}$ and $\Delta\mu_{MnO}$ (Figure 2.3c,f) do not. $\Delta\mu_{CaO}$ begins to change after the zoisite-out reaction (field 4-5, Figure 2.3c) because zoisite acts as a host for the excess calcium in the system that would have gone into forming garnet (buffering $\Delta\mu_{CaO}$), resulting in more zoisite in the excluded calculation (see negative volume difference in zoisite, Figure 2.4f), but only until the zoisite-out reaction is encountered. MnO is the only component that has a large difference in chemical potential right at the "equilibrium-in" (dashed line, Figure 2.3f). This change in energy is not mirrored in the ΔG diagram (Figure 2.3a) because MnO is only present in a small amount in this system (0.150 wt%, Table 2.2) so the energy change associated with this oxide only contributes a small amount to the total system Gibbs free energy.

The pattern of exponential increase in ΔG (Figure 2.3a) is matched in the diagrams for entropy (Figure 2.4a) and volume percent difference in chlorite (Figure 2.4d). The negative entropy difference at the "chemical-in" (Figure 2.4a) is a result of the system entropy having a less negative value in the excluded calculation, due to less fluid being released into the system because chlorite is not breaking down to form garnet. The lack of volume percent difference in other hydrous phases (biotite, white mica, and zoisite; Figure 2.4c,e,f) near the entropy change at the "chemical-in" indicates that these phases are not undergoing significant changes between the two systems at these conditions and instead chlorite is the key phase involved in the difference between the two systems at the "chemical-in".

The Central Maine Belt traverses (Figures 2.2 and 2.5) both depict a relatively flat volume percent difference in phases until the "chemical-in" is reached, wherein both display a negative volume percent difference in chlorite. This delay in volume percent difference in chlorite is nearly coincident with the large change in $\Delta\mu_{Al2O3}$ in both figures. In sample IS2, the zoisite-out reaction occurs at 461 °C (Figure 2.2, inset and stability field 4 to 5). This mineral

assemblage stability field represents the point where $\Delta\mu_{CaO}$ begins to deviate from a non-zero value and then remains at a plateau for the rest of the traverse. A similar pattern is seen in sample IS95 (Figure 2.5, inset and stability field 2 to 3) however, these two samples differ in that albite is predicted to be in the stable mineral assemblage only for sample IS2 and not for sample IS95. If zoisite and albite are present (Figure 2.2, sample IS2), then only $\Delta\mu_{CaO}$ experiences a change at the zoisite-out reaction and $\Delta\mu_{Al2O3}$ plateaus at a near zero value, appearing to be buffered by the presence of albite. The chemical potential difference traverse for sample IS95 shows the same pattern of the $\Delta\mu_{CaO}$ change at the zoisite-out reaction (stability field 2 to 3 on traverse, Figure 2.5), but because no albite is predicted to be stable along the traverse, a change in the $\Delta\mu_{Al2O3}$ begins at the "equilibrium-in" with an increase in the $\Delta\mu_{Al2O3}$ at the zoisite-out reaction. This $\Delta\mu_{Al2O3}$ is only present until stability field 3 (Figure 2.5) and then drops back to a near zero value until the "chemical-in" where the $\Delta\mu_{Al2O3}$ goes from a slightly positive value to a large negative value, indicating a significant change between the two systems and where we predict to be the most likely garnet growth conditions.

The $\Delta\mu_{Al2O3}$ and $\Delta\mu_{CaO}$ observed in the early stages of both traverses for the Central Maine Belt samples is most likely explained by the traverses of modal proportion zoisite in these samples. The insets in Figures 2.2 and 2.5 show a negative volume percent difference in zoisite following the "equilibrium-in", meaning that more zoisite is predicted to be stable if porphyroblast phases are excluded from the stable mineral assemblage, sequestering some of the Al_2O_3 and CaO that would usually go in to forming garnet, but only until the zoisite-out reaction is encountered. The $\Delta\mu_{CaO}$ and $\Delta\mu_{Al2O3}$ then reach a plateau for each sample (later for sample IS95) until the "chemical-in" wherein $\Delta\mu_{Al2O3}$ changes from a slightly positive value to a large negative value in both samples. This is also the point for both samples where $\Delta\mu_{FeO}$ and $\Delta\mu_{MgO}$ experience exponential increases in value that parallel the large volume percent change in chlorite at the "chemical-in".

Sample AV29 from the Pomfret Dome (Figure 2.6) is ideal for our study because the "equilibrium-in" and the "chemical-in" are located in the same mineral assemblage stability field. The chemical potential difference traverse (Figure 2.6) displays a delay in the onset of the change in $\Delta\mu_{Al2O3}$ until the "chemical-in" is reached. The volume percent difference in phases traverse shows that with this energetic deviation in the middle of a stability field (field 2, Figure

2.6), there is an increase in the volume percent difference of chlorite and plagioclase. Along the loading traverse for sample V396, stability field 3 (Figure 2.7) represents the location of the calculated muscovite-paragonite solvus. This phase transition is the cause of the jump in phase abundance difference of biotite, chlorite, muscovite, and paragonite as some of the muscovite is converted to paragonite and also represents the plagioclase-out reaction, hence the decrease to zero in the volume percent difference of plagioclase after this field. All of these phase transitions appear to have little effect on the chemical potential difference graph above, showing no appreciable change in $\Delta\mu_{Al2O3}$ until the "chemical-in" (Figure 2.7).

Similar to the Central Maine Belt samples, differences in whole rock chemistry result in different mineral assemblages predicted for the two Pomfret Dome samples, allowing us to study how chemical potential changes reflect petrologic changes as predicted by equilibrium thermodynamics. At the "chemical-in" for sample AV29 (Figure 2.6) there is a positive $\Delta\mu_{Al2O3}$ due to the stability of plagioclase (field 2, Figure 2.6). This positive $\Delta\mu_{Al2O3}$ is a result of more plagioclase predicted to be stable in the excluded calculation (negative volume percent difference in plagioclase, Figure 2.6), resulting in a more negative value of the free energy necessary to add one mole of Al_2O_3 to the system (or that Al_2O_3 is more energetically favorable in the excluded system). In sample V396, plagioclase is not present in the "chemical-in" stability field (field 4, Figure 2.7). Instead, biotite and paragonite are present in greater amounts in the system where porphyroblast phases have been excluded from the stable mineral assemblage, indicated by the negative volume percent difference in biotite and paragonite (Figure 2.7). This increase in abundance of micaceous minerals that contain less Al_2O_3 than plagioclase leads to free energy necessary to add one mole of Al_2O_3 to the system being less negative (or that Al_2O_3 is less energetically favorable in the excluded system), resulting in the negative $\Delta\mu_{Al2O3}$ at the "chemical-in" for this sample.

In sample 03-CW-04A from Transect D of the Nelson Aureole (Figure 2.8) the "chemical-in" temperature occurs at 548 °C along the traverse. When compared to the equilibrium predicted staurolite-in temperature at 551 °C, this yields a temperature difference of only 3 °C. The proximity of these two temperatures, in comparison with a 21 °C difference between the "equilibrium-in" and the "chemical-in" temperatures (527 °C vs. 548 °C), and the delay in change of $\Delta\mu_{CaO}$ and large deviations in $\Delta\mu_{Al2O3}$, $\Delta\mu_{FeO}$, $\Delta\mu_{MgO}$ and volume percent difference in chlorite at the staurolite-in temperature (Figure 2.8) lead us to conclude that garnet

growth in nature did not begin until all of the chemical potentials associated with the growth of garnet experienced a change in chemical potential difference, near the equilibrium predicted staurolite-in temperature. The coincidence of the temperature of garnet formation with that of staurolite formation is also in agreement with field observations recorded around the Nelson Aureole (Pattison and Tinkham, 2009; Pattison and Vogl, 2005), further supporting our decision to use the conditions wherein all Δμ are experiencing a deviation from zero values to determine the conditions of garnet growth in nature.

The published literature for the Nelson Aureole samples does not mention a method used to ensure the intersection of the exact garnet core was measured. This is unlike other samples used for this study (Central Maine Belt, Pomfret Dome and Sifnos), and could explain why the isopleth values for the Nelson Aureole samples do not line up with the field, chemical potential, and volume percent difference in chlorite observations for these samples. The difference in temperature between the "chemical-in" and the equilibrium predicted staurolite-in temperature for sample 93-CW-23 (Figure 2.9) is higher than that of sample 03-CW-04A (548 °C vs. 560 °C, 12 °C), but this discrepancy can be attributed to the larger spread in the value of core isopleth contours for this sample (phase diagram, Figure 2.9). We conclude that garnet growth occurred at a temperature closer to that of the staurolite-in reaction, based on the similar pattern in Δμ and difference in calculated chlorite abundance to sample 03-CW-04A, and with field observations for this aureole.

Along the traverse for sample 93-CW-23, the top of a muscovite-paragonite solvus is encountered between stability fields 9 and 10 (Figure 2.9) at the same point the equilibrium predicted staurolite-in reaction is encountered. This phase transition results in a large volume percent change in paragonite and muscovite, accompanied by a change in the volume percent difference of biotite and chlorite. Although a volume percent difference is present here due to location of the phase transition encountered, the pattern of $\Delta\mu_{CaO}$ and volume percent difference in chlorite is the same in this sample as for sample 03-OC-04A described above where the traverse does not encounter the calculated muscovite-paragonite solvus. The similar pattern for these two samples gives evidence to our claim that these chemical potential differences are related to the growth of garnet and not merely a relic of the encountered muscovite-paragonite solvus.

The "chemical-in" for Sifnos sample 06MSF-6C (Figure 2.10) coincides with the negative $\Delta\mu_{FeO}$ and $\Delta\mu_{MgO}$. Differences in chemical potential remain near zero for each of these major garnet-forming oxides until more than 100 °C from the "equilibrium-in" along the loading traverse for this sample. The change in chemical potential differences occurs near, but a few degrees below, the transition from stability field 7 to field 8 (Figure 2.10), where chlorite is lost from the stable mineral assemblage. Sample 23E (Figure 2.11) is unique in that all of the chemical potential differences experience a slight change at the "equilibrium-in", but not until near the "chemical-in" conditions do they all experience a large deviation from zero. The location of the "chemical-in" position occurs in the middle of a stability field (field 3, Figure 2.11) at the point where $\Delta\mu_{FeO}$ goes from a slightly positive value to a large negative value and near the conditions where chlorite and lawsonite, both hydrous phases, begin to experience a large negative volume percent difference.

Deformation is known to assist nucleation by building up strain energy in the reactant phases, contributing to the energy needed to overcome activation energy barriers, and by providing energetically favorable sites for nucleation (Pattison and Tinkham, 2009). Our study utilizes equilibrium thermodynamics phase diagram modeling that is based on Gibbs free energy minimization and does not take into account the potential addition of energy to a system due to strain energy upon deformation. Although our method does not immediately address the effect of elastic strain energy on nucleation, there are some theories that diffusivities are governed by the elastic-strain energies associated with the motion of ions through the host crystal (Carlson, 2006), so while our simulations do not directly address the issue of strain energy, by understanding the changes in chemical potential that develop in a deforming system, we can understand the diffusion processes (driven by chemical potential gradients) and thus at least to the second order the effect large amounts of elastic strain energy may have on a deforming system.

5.1 Evidence for Rapid Porphyroblast Growth

Some theories presented by Dragovic et al. (2012) to explain the rapid garnet growth observed in samples from Sifnos (occurring in less than 1.0 Ma and more likely spanning only tens to hundreds of thousands of years) are rapid overstepping (in P and T) and the involvement

of a kinetic catalyst, perhaps via the infiltration of an externally derived fluid. The presence of a fluid, either externally or internally derived, is thought to allow an overstepped reaction to rapidly run to completion by reducing kinetic barriers to nucleation and growth (Carlson et al., 1995; Baxter, 2003; Carlson, 2010; Dragovic et al., 2012). Porphyroblast-forming reactions often do not have a large initial driving force for reaction and due to this kinetic limitation, this process is well documented in a wide variety of metamorphic terranes including contact metamorphism, subduction zones, and regional orogenic systems (Austrheim, 1987; Carlson, 1989; Carlson et al., 1995; John and Schenk, 2003; Camacho et al., 2005; Ague and Baxter, 2007; Pattison and Tinkham, 2009; Carlson, 2010; Pollington and Baxter, 2010; Carlson, 2011; Pattison et al., 2011;Vorhies and Ague, 2011; Dragovic et al., 2012).

In both samples from Transect D of the Nelson Aureole, the "chemical-in" temperature is almost coincident with the equilibrium predicted staurolite-in temperature. This is in agreement with published field and petrologic observations for rocks surrounding the aureole (Pattison and Vogl, 2005; Tomkins and Pattison, 2007; Pattison and Tinkham, 2009). The chemical potential deviation at the equilibrium predicted staurolite-in temperature for the Nelson Aureole samples could possibly reflect the "cascade effect" as described by Pattison and Tinkham (2009), which proposes that once H_2O is released into the grain boundary medium due to the dehydration reaction associated with the formation of garnet, the kinetic barriers to nucleation and growth of other high-temperature porphyroblast phases (staurolite, andalusite) are lowered, resulting in most of the porphyroblast growth occurring over a small temperature interval. The "cascade effect" is a positive-feedback mechanism in which the first fluid evolved along a prograde path accelerates the rate of future reaction, generating additional fluid to accelerate reaction even more (Carlson, 2010). While this effect has been postulated for a number of metamorphic settings, the literature lacks evidence as to how we can use the laws of equilibrium thermodynamics to determine when this "cascade effect" begins in natural settings.

5.2 Petrological Implications of Suppressed Garnet Nucleation

Sample 03-OC-04 from Transect B in the Nelson Aureole (Figure 2.12) is used as a case study to examine the petrologic results that one might expect in a natural system if garnet nucleation were suppressed to such a degree that numerous mineral assemblage stability fields

were passed before the final garnet growth conditions were reached. A major difference in this sample compared to other samples used for this study is the more complex geometry of the phase diagrams between the "equilibrium-in" and the "chemical-in" conditions. In sample 03-OC-04, the "chemical-in" is present more than 200 °C up-temperature from the "equilibrium-in". A temperature overstep of this magnitude is much larger than predicted for the other two samples used from the Nelson Aureole, but those samples were collected along a different transect (Transect D) at a greater distance from the aureole. Sample 03-OC-04 was collected 320 meters from the aureole and the other two samples were taken from 1340 and 1130 meters (03-CW-04 and 93-CW-23, respectively) Tomkins and Pattison (2007). The proximity to the contact aureole could mean sample 03-OC-04 was exposed to a more rapid heating rate than the other samples used from the Nelson Aureole, explaining the larger overstep in temperature before garnet growth conditions were reached.

At the "equilibrium-in" there is a small oscillation in the $\Delta\mu_{Al2O3}$ that we attribute to being the result of the loss of an Al_2O_3 buffer (albite) during the transition between stability field 2 to 3 on the traverse (Figure 2.12) that also coincides with the intersection of two stability fields above the numbered traverse fields that end near the equilibrium predicted garnet-in reaction, most likely also contributing to some of this oscillation effect. The zoisite-out reaction is encountered along the traverse around 400 °C (stability field 5 to 6, Figure 2.12), accompanied by a change in the $\Delta\mu_{CaO}$ similar to those in samples IS2 and IS95 from the Central Maine Belt (Figures 2.1 and 2.2). However, in this sample, the zoisite-out reaction on the phase diagram wherein porphyroblast phases were permitted (Figure 2.12) does not occur at the same conditions as the zoisite-out reaction on the phase diagram wherein porphyroblast phases were excluded. Instead, the zoisite stability field continues up-temperature in the second phase diagram calculation, past stability field 5 to 6 in Figure 2.12. If the zoisite-out reaction would have occurred at the same conditions in both phase diagram calculations, the difference in modal proportion of zoisite would reduce to zero after stability field 5 to 6 (Figure 2.12). These results imply that when porphyroblast phases are excluded from the stable mineral assemblage, at this stability field boundary, more zoisite is predicted to be stable. These conditions remain until 427 °C, stability field 6 to 7 (Figure 2.12), wherein zoisite is finally removed from the stable mineral assemblage in the excluded phase diagram calculation (where the volume percent difference in zoisite goes to zero).

At this point, due to the still suppressed nucleation of garnet and staurolite, more plagioclase is predicted to be stable, represented by a negative volume percent difference in plagioclase (taking some of the Ca and Al that would have went in to forming garnet) and less albite and muscovite, represented by a positive volume percent difference. This is due to plagioclase taking some of the free Na and Ca in the system and is accompanied by changes in $\Delta\mu_{Al2O3}$ and $\Delta\mu_{CaO}$. The $\Delta\mu_{Al2O3}$ and $\Delta\mu_{CaO}$ then go back to near zero values until right before the "chemical-in", where chlorite is lost from the stable mineral assemblage (fields 13 to 14, Figure 2.12). This represents the only conditions along this traverse where all of the major garnet-forming oxides are experiencing a deviation from zero in chemical potential difference. The calculated muscovite-paragonite solvus is encountered at stability field 11 to 12 (Figure 2.12), but appears to have no appreciable effect on the chemical potential difference values.

If all chemical potentials must experience a change from their pre-nucleation conditions (represented by a $\Delta\mu$) in order for garnet to nucleate and grow, then only a few degrees before the "chemical-in" (stability field 13 to 14, Figure 2.12), where all of the oxides associated with the formation of garnet are experiencing a change in chemical potential difference, do we predict garnet growth will finally take place. The small temperature span between the "chemical-in" position and the deviation from zero in chemical potential difference, compared to the much larger temperature span between the "equilibrium-in" and the "chemical-in" for this sample (277 °C, Figure 2.12), and the potential for published core compositions to not represent the exact chemistry of the garnet crystal cores as discussed above give confidence in our decision to use these conditions as the "true" nucleation conditions for garnet in nature.

The "chemical-in" (Figure 2.12) is coincident with the beginning of an andalusite-bearing stability field and also represents the conditions where chlorite is lost from the stable mineral assemblage in the phase diagram where porphyroblast phases are excluded from the stable mineral assemblage. This is represented by the negative volume percent difference in andalusite and the volume percent difference in chlorite reducing to zero at these conditions. The proximity of the "chemical-in" to the stability of higher temperature porphyroblast phases when garnet and staurolite are excluded from the stable mineral assemblage (andalusite followed by cordierite) calls in to question the accuracy of this method when using the "chemical-in" to determine nucleation conditions for this sample as opposed to the lower temperature corresponding to the changes in $\Delta\mu_{Al2O3}$ and $\Delta_{CaO,}$ further supporting our decision to use the $\Delta\mu$ pattern to determine

the garnet nucleation conditions for this sample. While the phase diagram and associated traverses for sample 03-OC-04 are less simplistic than those presented for other samples in this study, the published mineral assemblage associated with Transect B from the Nelson Aureole is: And + Bt + Grt (Tomkins and Pattison, 2007). Stability fields 14 and 15 (Figure 2.12) that we attribute to being near the energetically favorable growth conditions for garnet include both garnet and biotite and while neither field includes andalusite, up temperature only slightly is the equilibrium predicted andalusite-in reaction following stability field 15. Furthermore, if porphyroblast phases are excluded from the stable mineral assemblage, paralleling the observed nucleation suppression reported in the literature for this sample, the predicted stability field containing andalusite occurs right at the "chemical-in", along with the chlorite-out reaction, indicating that the proximity of the "chemical-in", chemical potential differences, and volume percent difference in chlorite and andalusite must somehow be related to when the garnet growth conditions were reached in nature during the metamorphic history of this sample.

6. Conclusions

If we have demonstrated that the delay in the onset of the garnet-forming reaction is indeed directly related to the chemical potential differences that build up when garnet nucleation is suppressed, then we have accomplished two major goals through this study. First, by discovering a method that allows the usage of equilibrium thermodynamics based modeling programs to predict where in pressure-temperature space a garnet porphyroblast grew. Second, the phases that are major players in the garnet-forming reaction in a natural system should be the phases experiencing a volume percent change in the above calculations.

There are numerous scenarios when this method would not accurately describe the energetic changes undergone in a natural system as the garnet-forming reaction is overstepped. One is that the garnet core chemistry used for the isopleth calculation does not record the true growth conditions of the crystal, making the "chemical-in" inaccurate. This could be due to a sectioning problem (as discussed for the Nelson Aureole samples) or because of diffusional modification of the core chemistry after crystal growth. Another issue could be that the bulk rock composition used for the phase diagram calculation does not accurately represent the chemical system the rock grew from. Fluids are another important parameter in metamorphism and here a

closed system was assumed with H_2O in excess. This means that the effects of H_2O activity on the kinetics of metamorphic reactions, a known factor that can affect diffusion rates of cations and equilibration time and length scales (Carlson, 2010) are not accurately represented by the above calculations.

The effect of a kinetic control (e.g. fluids) on the reaction rate and other factors that can affect reaction rates (e.g. heating rates) cannot be directly studied using this method. However, Carlson (2011) states that the most fundamental control on the rate of prograde metamorphism is heating rate and by measuring the amount of thermal overstepping, we should at least to a second order be able to infer the effects of heating rate on reaction mechanisms. A last, but important issue is the mixing models used for each phase diagram calculation. The compositional variables in the mixing models may not be representative of the true mineral chemistry because mixing models are usually simplified representations of a more chemically complex natural phase. Furthermore, the parameters within with each mixing model (energy, entropy, end-members) may not represent the conditions during the natural metamorphic reactions simulated by the phase diagram calculations. The effects of compositional variation between phases present in the allowed and excluded phase diagram calculations on the environment we assume garnet nucleated in is also not addressed in detail by this study.

The consistent pattern of the last change (deviation from zero) in the chemical potential difference of a major garnet-forming oxide matching up with the chemically predicted garnet nucleation P-T conditions, "chemical-in", based on the intersection of core isopleths is consistent in all of the above samples from a variety of metamorphic terranes and mineral assemblages. The thermal overstepping of the garnet-forming reaction is known to be larger during fast, low pressure contact metamorphism settings than in regional metamorphic settings, characterized by slower heating rates (Gaidies et al., 2011). Our models show that regardless of the rock type, metamorphic terrane, chemical system, mixing models, and amount of temperature and/or pressure overstep, there is always one chemical potential that experiences a delay in the onset of a buildup in free energy that corresponds to the "chemical-in".

The similar patterns of chemical potential differences in samples experiencing a temperature overstep or a temperature and pressure overstep of the equilibrium predicted garnet forming reaction does not violate any of the previously proposed thermodynamic laws regarding nucleation and growth rates because oversteps in pressure can be explained by the same

thermodynamic laws, although less commonly reported in metamorphic systems. In fact, after pressure exceeds that of T_m(max), increasing pressure at a fixed temperature is thought to enhance the diffusion kinetics in a mineral since it would bring the mineral progressively closer to T_m (Ganguly, 2002). For the purposes of our study, this means that a sample undergoing an overstep in temperature and/or pressure of the equilibrium predicted garnet-in reaction will experience enhanced diffusion as recorded by the chemical potentials of diffusing components in the system. Thus, the observed changes in chemical potential (that control diffusion) relate equally to overstep in pressure and in temperature.

Volume percent difference in phases traverses show that the "chemical-in" usually lines up with the conditions where chlorite begins to experience a large increase in negative volume percent difference. This does not occur at a phase boundary (as represented by the numbered stability fields along each traverse) and instead the "chemical-in" for most samples occurs either in the middle of a stability field, or coincident with the staurolite-in P-T as predicted by equilibrium thermodynamics (Nelson Aureole samples: Figures 2.8 and 2.9). The change in volume percent difference in chlorite near the "chemical-in" is present in all samples (in Sifnos samples and 03-OC-04, where chlorite is lost from the stable mineral assemblage). The conditions where there begins to be a major negative volume percent difference in chlorite between the two calculations is a result of more chlorite predicted to be stable in the excluded calculation and thus represents the point where most of the chlorite breakdown to form garnet occurred in the allowed calculation.

This pattern of chlorite volume percent change near the "chemical-in" is mirrored in the entropy difference diagram for sample IS2 (Figure 2.3a), further supporting our claim that this is most likely the point in nature where most of the breakdown of chlorite to form garnet occurred, resulting in the release of H_2O into the system and increasing the system entropy (more negative) in the allowed phase diagram calculation, resulting in the negative entropy difference at these conditions. The change in chemical potential difference of the major garnet-forming oxides, and major changes in the difference calculations for volume percent chlorite, total system Gibbs free energy, and entropy (Figure 2.3 and 2.4) all coinciding with the "chemical-in" could be the first evidence of the "cascade effect" (Pattison and Tinkham, 2009; Carlson, 2010) in equilibrium thermodynamics based modeling. If this method is recording when the garnet-forming reaction occurred at disequilibrium conditions (natural settings), then it also highlights the most important

mixing models in the equilibrium thermodynamics based modeling programs that record these differences between equilibrium and nature. Future work would be to dig deeper into the mixing models used to calculate phase diagrams in order to alleviate this discrepancy between the conditions during natural reactions and the conditions a reaction is predicted to occur at based on equilibrium thermodynamics.

For a nucleus to grow, equilibrium thermodynamics predicts the point in P-T space (reaction line) to occur where the overall Gibbs free-energy change associated with its formation has a negative value ($\Delta G_{reaction} < 0$). Basic chemistry, however tells us that a reaction cannot proceed until all of the reactants are present. Our results imply that the garnet-forming reaction cannot occur in nature until the Gibbs free energy of all the chemical potentials (reactants) involved in the formation of a garnet porphyroblast are experiencing a change from their pre-nucleation states (μ_{Al2O3}, μ_{CaO}, μ_{FeO}, μ_{MgO}, μ_{MnO}) and not merely the sum of the total system free energy being a negative value. This means that while the reaction affinity can be used to describe the size of the barrier to nucleation in terms of free energy (Waters and Lovegrove, 2002), the chemical potential differences explain why this buildup is happening. This is because chemical potentials control diffusion and the diffusive flux of a component is dependent on the chemical potential gradient within the system. The pattern in chemical potential differences and the continuation of this pattern in the location of the large changes in volume percent difference in chlorite for all samples, leads us to the conclusion that this method records the true conditions of the garnet forming reaction (when it is energetically favorable) that occurred at disequilibrium conditions in nature for the above samples.

References

Ague, J. J., and Baxter, E. F., 2007, Brief thermal pulses during mountain building recorded by Sr diffusion in apatite and multicomponent diffusion in garnet: Earth and Planetary Science Letters, v. 261, no. 3-4, p. 500-516.

Ali, A., 2010, The tectono-metamorphic evolution of the Balcooma Metamorphic Group, north-eastern Australia: a multidisciplinary approach: Journal of Metamorphic Geology, v. 28, p. 397-422.

Andersen, D. J., and Lindsley, D. H., 1988, Internally consistent solution models for Fe-Mg-Mn-Ti oxides - Fe-Ti oxides: American Mineralogist, v. 73, no. 7-8, p. 714-726.

Austrheim, H., 1987, Eclogitization of lower crustal granulites by fluid migration through shear zones: Earth and Planetary Science Letters, v. 81, no. 2-3, p. 221-232.

Baxter, E. F., 2003, Natural constraints on metamorphic reaction rates, *in* Vance, D., Muller, W., and Villa, I. M., eds., Geochronology: Linking the Isotopic Record with Petrology and Textures, Volume 220, p. 183-202.

Bell, T. H., and Bruce, M. D., 2006, The internal inclusion trail geometries preserved within a first phase of porphyroblast growth: Journal of Structural Geology, v. 28, no. 236-252.

Bell, T.H., and Bruce, M.D., 2007, Progressive deformation partitioning and deformation history: evidence from millipede structures: Journal of Structural Geology, v. 29, p. 18-35.

Bell, T. H., and Hayward, N., 1991, Episodic metamorphic reactions during orogenesis: the control of deformation partitioning on reaction sites and duration: Journal of Metamorphic Geology, no. 9, p. 619-640.

Bell, T. H., Rieuwers, M. T., Cihan, M., Evans, T. P., Ham, A. P., and Welch, P. W., 2013, Inter-relationships between deformation partitioning, metamorphism and tectonism: Tectonophysics, v. 587, p. 119-132.

Bons, P. D. D., Koehn, D., and Jessell, M. W., 2008, Microdynamics Simulation, Springer.

Camacho, A., Lee, J. K. W., Hensen, B. J., and Braun, J., 2005, Short-lived orogenic cycles and the eclogitization of cold crust by spasmodic hot fluids: Nature, v. 435, no. 7046, p. 1191-1196.

Carlson, W. D., 1989, The significance of intergranular diffusion to the mechanisms and kinetics of porphyroblast crystallization: Contributions to Mineralogy and Petrology, v. 103, no. 1, p. 1-24.

Carlson, W.D., 1999, The case against Ostwald ripening of porphyroblasts: Canadian Mineralogist, v. 37, p. 403-413.

Carlson, W. D., 2002, Scales of disequilibriumn and rates of equilibration during metamorphism: American Mineralogist, v. 87, p. 185-204.

Carlson, W. D., 2006, Rates of Fe, Mg, Mn, and Ca diffusion in garnet: American Mineralogist, v. 91, no. 1, p. 1-11.

Carlson, W.D., 2010, Dependence of reaction kinetics on H2O activity as inferred from rates of intergranular diffusion of aluminium: Journal of Metamorphic Geology, v. 28, no. 7, p. 735-752.

Carlson, W. D., 2011, Porphyroblast crystallization: linking processes, kinetics, and microstructures: International Geology Review, v. 53, no. 3-4, p. 406-445.

Carlson, W. D., Denison, C., and Ketcham, R. A., 1995, Controls on the nucleation and growth of porphyroblasts: Kinetics from natural textures and numerical models: Geological Journal, v. 30, no. 3-4, p. 207-225.

Carmichael, D. M., 1969, On the mechanism of prograde metamorphic reactions in quartz-bearing pelitic rocks: Contributions to Mineralogy and Petrology, v. 20, p. 24.

Chakraborty, S., and Ganguly, J., 1992, Cation diffusion in aluminosilicate garnets - experimental-determination in spessartine-almandine diffusion couples, evaluation of effective binary diffusion-coefficients, and applications: Contributions to Mineralogy and Petrology, v. 111, no. 1, p. 74-86.

Chambers, J., Caddick, M., Argles, T., Horstwood, M., Sherlock, S., Harris, N., Parrish, R., and Ahmad, T., 2009, Empirical constraints on extrusion mechanisms from the upper margin of an exhumed high-grade orogenic core, Sutlej valley, NW India: Tectonophysics, v. 477, p. 16.

Chernoff, C. B., and Carlson, W. D., 1997, Disequilibrium for Ca during growth of pelitic garnet: Journal of Metamorphic Geology, v. 15, no. 4, p. 421-438.

Cihan, M., Evins, P. M., Lisowiec, N. J., and Blake, K. L., 2006, Time constraints on deformation and metamorphism from EPMA dating of monazite in the Proterozoic Robertson River Metamorphics, NE Australia: Precambrian Research, no. 145, p. 1-23.

Coggon, R., and Holland, T. J. B., 2002, Mixing properties of phengitic micas and revised garnet-phengite thermobarometers: Journal of Metamorphic Geology, v. 20, p. 683-696.

Connolly, J. A. D., 1990, Multivariable phase diagrams: an algorithm based on generalized thermodynamics: American Journal of Science, v. 290, p. 666-718.

Connolly, J. A. D., and Petrini, K., 2002, An automated strategy for calculation of phase diagram sections and retrieval of rock properties as a function of physical conditions: Journal of Metamorphic Geology, v. 20, p. 697-708.

Dale, J., Holland, T., and Powell, R., 2000, Hornblende-garnet-plagioclase thermobarometry: a natural assemblage calibration of the thermodynamics of hornblende: Contributions to Mineralogy and Petrology, v. 140, no. 3, p. 353-362.

Dale, J., Powell, R., White, R. W., Elmer, F. L., and Holland, T. J. B., 2005, A thermodynamic model for Ca-Na clinoamphiboles in Na2O-CaO-FeO-MgO-Al2O3-SiO2-H2O-O for petrological calculations: Journal of Metamorphic Geology, v. 23, no. 8, p. 771-791.

Dragovic, B., Samanta, L. M., Baxter, E. F., and Selverstone, J., 2012, Using garnet to constrain the duration and rate of water-releasing metamorphic reactions during subduction: An example from Sifnos, Greece: Chemical Geology, v. 314–317, no. 0, p. 9-22.

Elphick, S. C., Ganguly, J., and Loomis, T. P., 1985, Experimental-determination of cation diffusivities in aluminosilicate garnets .1. Experimental methods and interdiffusion data: Contributions to Mineralogy and Petrology, v. 90, no. 1, p. 36-44.

Evans, T. P., 2004, A method for calculating effective bulk composition modification due to crystal fractionation in garnet-bearing schist: implications for isopleth thermobarometry: Journal of Metamorphic Geology, v. 22, p. 547-557.

Fisher, G. W., 1978, Rate laws in metamorphism: Geochimica Et Cosmochimica Acta, v. 42, no. 7, p. 1035-&.

Foster, C. T., 1986, Thermodynamic models of reactions involving garnet in a sillimanite staurolite schist: Mineralogical Magazine, v. 50, no. 357, p. 427-439.

Fuhrman, M. L., and Lindsley, D. H., 1988, Ternary-feldspar modeling and thermometry: American Mineralogist, v. 73, no. 3-4, p. 201-215.

Gaidies, F., Pattison, D. R. M., and de Capitani, C., 2011, Toward a quantitative model of metamorphic nucleation and growth: Contributions to Mineralogy and Petrology, v. 162, no. 5, p. 975-993.

Ganguly, J., 2002, Diffusion kinetics in minerals: Principles and applicatinos to tectono-metamorphic processes: EMU Notes in Mineralogy, v. 4, p. 39.

Gibbs, J. W., 1928, The collected works, New York, Longmans & Green, Thermodynamics.

Green, E., Holland, T., and Powell, R., 2007, An order-disorder model for omphacitic pyroxenes in the system jadeite-diopside-hedenbergite-acmite, with applications to eclogitic rocks: American Mineralogist, v. 92, no. 7, p. 1181-1189.

Hillert, M., 1999, Solute drag, solute trapping and diffusional dissipation of Gibbs Energy: Acta Mater, v. 47, p. 4481-4505.

Hillert, M., and Rettenmayr, M., 2003, Deviation from local equilibrium at migrating phase interfaces: Acta Mater, v. 51, p. 2803-2809.

Hirsch, D. M., and Carlson, W. D., 2006, Variations in rates of nucleation and growth of biotite porphyroblasts: Journal of Metamorphic Geology, v. 24, no. 8, p. 763-777.

Hirsch, D. M., Prior, D. J., and Carlson, W. D., 2003, An overgrowth model to explain multiple, dispersed high Mn regions in the cores of garnet porphyroblasts: American Mineralogist, v. 73, p. 20-47.

Holland, T., Baker, J., and Powell, R., 1998, Mixing properties and activity-composition relationships of chlorites in the system MgO-FeO-Al2O3-SiO2-H2O: European Journal of Mineralogy, v. 10, no. 3, p. 395-406.

Holland, T. J. B., and Powell, R., 1998, An internally consistent thermodynamic dataset for phases of petrological interest: Journal of Metamorphic Geology, v. 16, p. 309-343.

Holland, T.J.B., and Powell, R., 2003, Activity-composition relations for phases in petrological calculations: an asymmetric multicomponent formulation: Contributions to Mineralogy and Petrology, v. 145, p. 492-501.

Joesten, R., and van Horn, S. R., 1999, Numerical modeling of calcite coarsening in the aureoles of en echelon dikes: Analysis of the kinetic control of isograd geometry in contact metamorphism, Kluwer Academic, Growth, dissolution and pattern formation in geosystems:, 109-141 p.:

John, T., and Schenk, V., 2003, Partial eclogitisation of gabbroic rocks in a late Precambrian subduction zone (Zambia): prograde metamorphism triggered by fluid infiltration: Contributions to Mineralogy and Petrology, v. 146, no. 2, p. 174-191.

Kaischew, R., and Stranski, I. N., 1934, Concerning the mechanism of the equilibrium of small crystals: Zeitschrift fur Physikalische Chemie-Abteilung B-Chemie der Elementaprozesse Aufbau der Materie, v. 26, p. 312-316.

Laubach, S. E., and Diaz-Tushman, K., 2009, Laurentian paleostress trajectories and ephemeral fracture permeability, Cambrian Eriboll Formation sandstones west of the Moine Thrust Zone, NW Scotland: Journal of the Geological Society of London, no. 166, p. 349-362.

Loomis, T. P., 1983, Compositional zoning of crystals. In: Saxena SK (ed) A record of growth and reaction history: Adv Phys Geochem, v. 3, p. 1-60.

Mahar, E. M., Baker, J. M., Powell, R., Holland, T. J. B., and Howell, N., 1997, The effect of Mn on mineral stability in metapelites: Journal of Metamorphic Geology, v. 15, no. 2, p. 223-238.

Pattison, D. R. M., De Capitani, C., and Gaidies, F., 2011, Petrological consequences of variations in metamorphic reaction affinity: Journal of Metamorphic Geology, v. 29, no. 9, p. 953-977.

Pattison, D. R. M., and Tinkham, D. K., 2008, Equilibrium and kinetics in metamorphism of pelites in the Nelson aureole, British Columbia: Geochimica Et Cosmochimica Acta, v. 72, no. 12, p. A728-A728.

Pattison, D. R. M., and Tinkham, D. K., 2009, Interplay between equilibrium and kinetics in prograde metamorphism of pelites: an example from the Nelson aureole, British Columbia: Journal of Metamorphic Geology, v. 27, no. 4, p. 249-279.

Pattison, D. R. M., and Vogl, J. J., 2005, Contrasting sequences of metapelitic mineral-assemblages in the aureole of the tilted Nelson Batholith, British Columbia: Implications for phase equilibria and pressure determination in andalusite-sillimanite-type settings: Canadian Mineralogist, v. 43, p. 51-88.

Pollington, A. D., and Baxter, E. F., 2010, High resolution Sm-Nd garnet geochronology reveals the uneven pace of tectonometamorphic processes: Earth and Planetary Science Letters, v. 293, no. 1-2, p. 63-71.

Pollington, A. D., and Baxter, E. F., 2011, High precision microsampling and preparation of zoned garnet porphyroblasts for Sm-Nd geochronology: Chemical Geology, v. 281, no. 3-4, p. 270-282.

Powell, R., and Holland, T., 1990, Calculated mineral equilibria in the pelite system, KFMASH (K_2O-FeO-MgO-Al_2O_3-SiO_2-H_2O): American Mineralogist, v. 75, no. 3-4, p. 367-380.

Powell, R., and Holland, T., 1999, Relating formulations of the thermodynamics of mineral solid solutions: Activity modeling of pyroxenes, amphiboles, and micas: American Mineralogist, v. 84, no. 1-2, p. 1-14.

Powell, R., and Holland, T. J. B., 1988, An internally consistent dataset with uncertainties and correlations; 3, Applications to geobarometry, worked examples and a computer program: Journal of Metamorphic Geology, v. 6, p. 173-204.

Rubie, D. C., 1998, Disequilibrium during metamorphism: the role of nucleation kinetics, *in* Taylor, P. J., and Obrien, P. J., eds., What Drives Metamorphism and Metamorphic Reactions?, Volume 138, p. 199-214.

Sanislav, I. V., and Bell, T. H., 2011, The inter-relationships between long-lived metamorphism, pluton emplacement and changes in the direction of bulk shortening during orogenesis: Journal of Metamorphic Geology, v. 29, no. 5, p. 513-536.

Sayab, M., 2007, Correlating multiple deformation events across the Mesoproterozoic NE Australia using foliation intersection axes (FIA) preserved within porphyroblasts: Gondwana Research, v. 13, p. 331-351.

Smye, A. J., Greenwood, L. V., and Holland, T. J. B., 2010, Garnet-chloritoid-kyanite assemblages: eclogite facies indicators of subduction constraints in orogenic belts: Journal of Metamorphic Geology, v. 28, no. 7, p. 753-768.

Solar, G. S., and Brown, M., 2001a, Deformation partitioning during transpression in response to Early Devonian oblique convergence, northern Appalachian orogen, U.S.A.: Journal of Structural Geology, v. 22, p. 1043-1065.

Solar, G. S., and Brown, M., 2001b, Petrogenesis of migmatites in Maine, U.S.A.: possible source of peraluminous granite in plutions: Journal of Petrology, v. 42, p. 789-823.

Solar, G. S., Pressley, R. A., Brown, M., and Tucker, R. D., 1998, Granite ascent in convergent orogenic belts: Testing a model: Geology, v. 26, no. 8, p. 4.

Spear, F. S., and Daniel, C. G., 2001, Diffusion control of garnet growth, Harpswell Neck, Maine, USA: Journal of Metamorphic Geology, v. 19, no. 2, p. 179-195.

Spear, F. S., Kohn, M. J., Cheney, J. T., and Florence, F., 2002, Metamorphic, thermal, and tectonic evolution of central New England: Journal of Petrology, v. 43, no. 11, p. 2097-2120.

Stipska, P., Powell, R., White, R. W., and Baldwin, J. A., 2010, Using calculated chemical potential relationships to account for coronas around kyanite: an example from the Bohemian Massif: Journal of Metamorphic Geology, v. 28, no. 1, p. 97-116.

Tinkham, D. K., and Ghent, E. D., 2005, Estimating P-T conditions of garnet growth with isochemical phase-diagram sections and the problem of effective bulk-composition: Canadian Mineralogist, v. 43, p. 35-50.

Tinkham, D. K., Zuluaga, C. A., and Stowell, H. H., 2001, Metapelite phase equilibria modeling in MnNCKFMASH: the effect of variable Al_2O_3 and MgO/(MgO+FeO) on mineral stability: Geological Materials Research, v. 3, p. 1-35.

Tomkins, H. S., and Pattison, D. R. M., 2007, Accessory phase petrogenesis in relation to major phase assemblages in pelites from the Nelson contact aureole, southern British Columbia: Journal of Metamorphic Geology, v. 25, no. 4, p. 401-421.

Vance, D., and Mahar, E., 1998, Pressure-temperture paths from P-T pseudosections and zoned garnets: potential, limitations and examples from the Sanskar Himalayas, NW India: Contributions to Mineralogy and Petrology, v. 132, p. 225-245.

Volmer, M., and Weber, A., 1926, Keimbildung in ubersattigten Gebilden: Zeitschrift fur Physikalische Chemie-Abteilung B-Chemie der Elementaprozesse Aufbau der Materie, v. 119, p. 277-301.

Vorhies, S. H., and Ague, J. J., 2011, Pressure-temperature evolution and thermal regimes in the Barrovian zones, Scotland: Journal of the Geological Society, v. 168, no. 5, p. 1147-1166.

Waters, D. J., and Lovegrove, D. P., 2002, Assessing the extent of disequilibrium and overstepping of prograde metamorphic reactions in metapelites from the Bushveld Complex aureole, South Africa: Journal of Metamorphic Geology, v. 20, no. 1, p. 135-149.

White, R. W., Pomroy, N. E., and Powell, R., 2005, An in situ metatexite-diatexite transition in upper amphibolite facies rocks from Broken Hill, Australia: Journal of Metamorphic Geology, v. 23, no. 7, p. 579-602.

White, R. W., Powell, R., and Baldwin, J. A., 2008, Calculated phase equilibria involving chemical potentials to investigate the textural evolution of metamorphic rocks: Journal of Metamorphic Geology, v. 26, no. 2, p. 181-198.

White, R. W., Powell, R., and Holland, T.J.B., 2001, Calculation of partial melting equilibria in the system Na_2O-CaO-K_2O-FeO-MgO-Al_2O_3-SiO_2-H2O (NCKF-MASH): Journal of Metamorphic Geology, v. 19, no. 139-153.

Whitney, D. L., and Evans, B. W., 2010, Abbreviations for names of rock-forming minerals: American Mineralogist, v. 95, no. 1, p. 185-187.

Winter, J. D., 2010, An introduction to igneous and metamorphic petrology, New Jersey, Pearson Education, Inc., 702 p.:

Figures

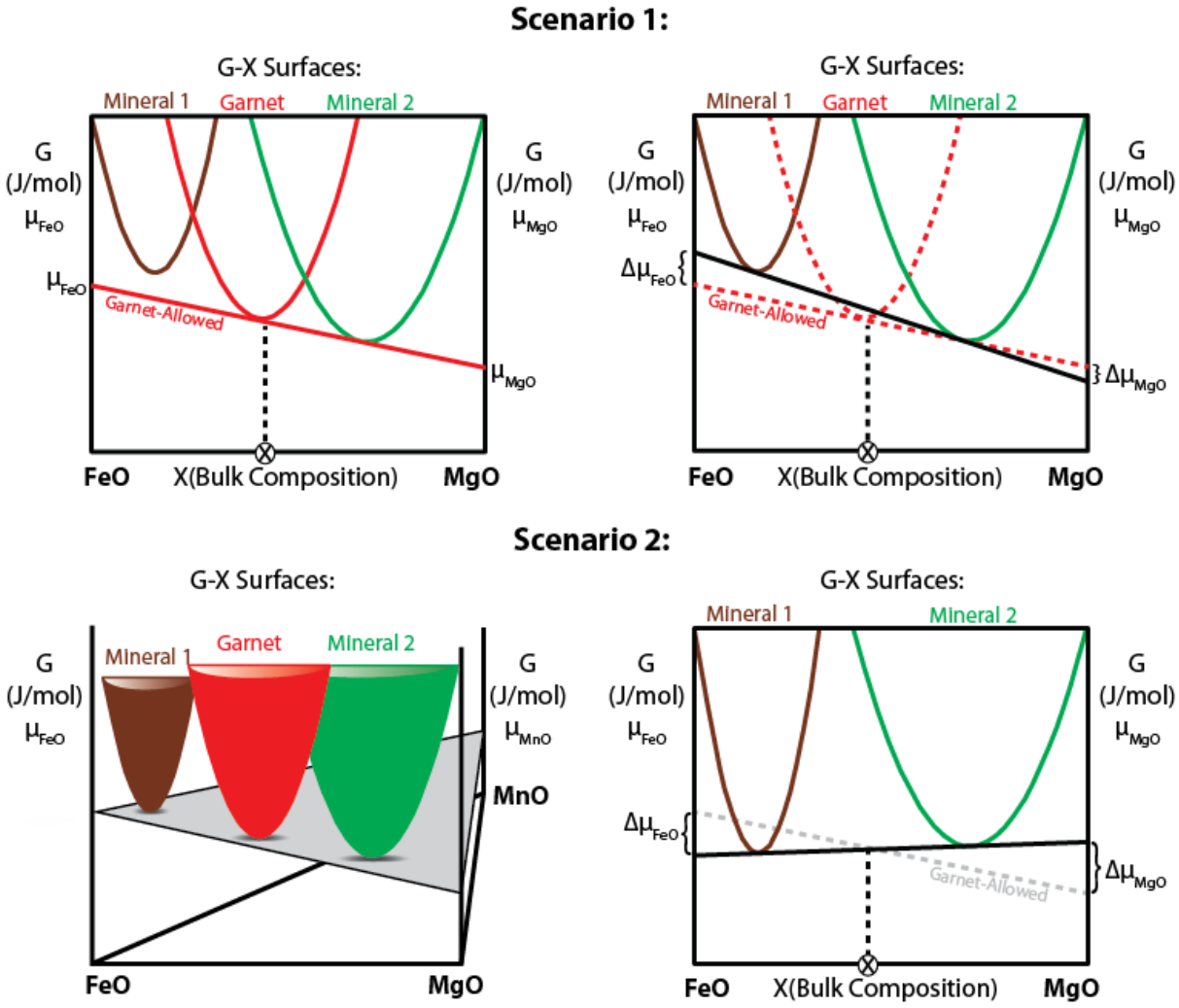

Figure 2.1. Free Energy-Composition (G-X) diagrams depicting the two possible scenarios for chemical systems where garnet is allowed as part of the stable mineral assemblage and where garnet has been excluded from the stable mineral assemblage. P, T, and X are fixed. The point where the tangent to the minerals' G-X surfaces intersect the chemical potential axes represent the chemical potential of each component at the lowest energy configuration for the system (equilibrium state). In Scenario 1, red line represents the tangent to the G-X surfaces of Garnet and Mineral 2 to achieve the lowest energy configuration for the system. In right diagram, red dashed lines represent the original tangent and the G-X surface of garnet to represent garnet being removed from the stable mineral assemblage (as is done in the second phase diagram calculation for all of the following examples). The difference between the chemical potential values ($\Delta\mu_{FeO}$ and $\Delta\mu_{MgO}$) for the garnet allowed and garnet excluded systems is what is calculated in the following figures for all samples. In Scenario 1, to satisfy the phase rule, a new phase must become stable in order to keep (C = P = 2), resulting in the new lowest energy configuration consisting of Mineral 1 and Mineral 2. In Scenario 2, the left diagram depicts a 3-

D, G-X diagram to represent the stable energy configuration for a three component system and the gray planar surface represents the tangent to the three minerals G-X surfaces (C = P = 3). In right diagram, the system has been reduced from a three component system to a two component system in order to describe a new stable mineral assemblage when garnet is removed from the stable mineral assemblage and no new mineral forms in its place. To describe the new, two component system, the G-X diagram must also be reduced from 3-D to 2-D. Gray dashed line represents the original planar tangent and black line represents the new tangent to the two stable minerals G-X surfaces (C = P = 2) and the new lowest energy configuration.

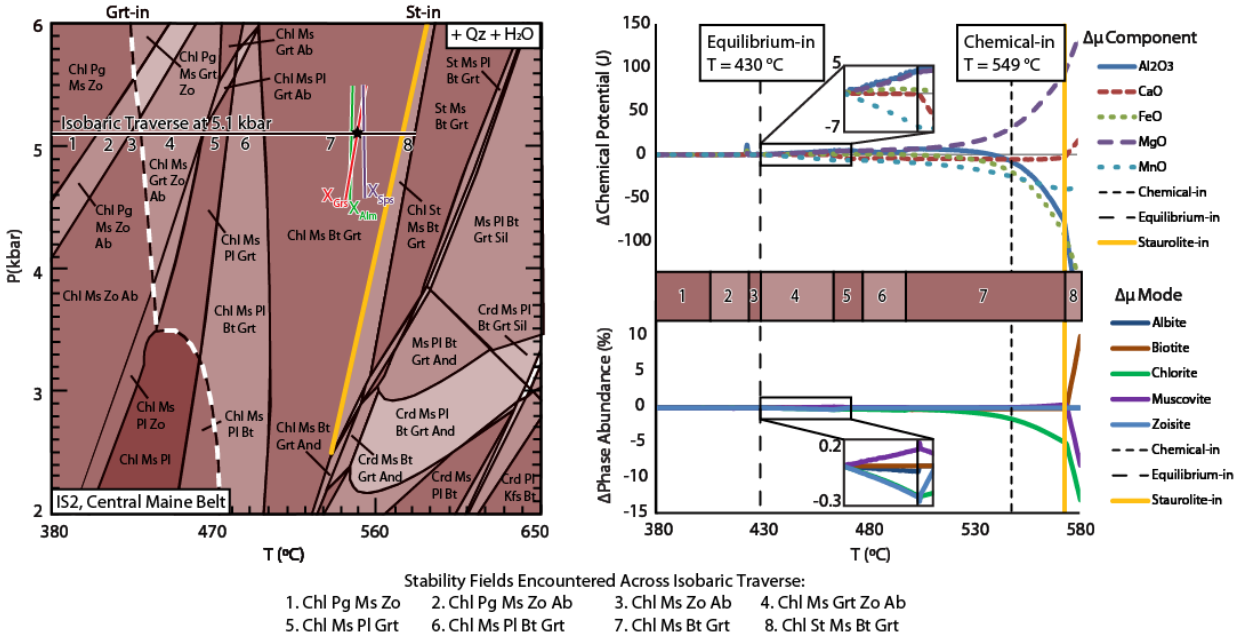

Figure 2.2. All data for sample IS2 from the Central Maine Belt. On phase diagram, dashed line represents the equilibrium predicted garnet-in reaction boundary and star represents the "chemical-in", determined using the intersection of core isopleths (labeled). The top graph displays the chemical potential difference of all major garnet forming oxides, normalized to the mol% of each oxide present in the chemical system and the bottom graph represents the volume percent difference in phases. On phase diagram, increasingly darker shades of color represent domains of increasing Gibbs phase rule variancy and mineral abbreviations are according to Whitney and Evans (2010).

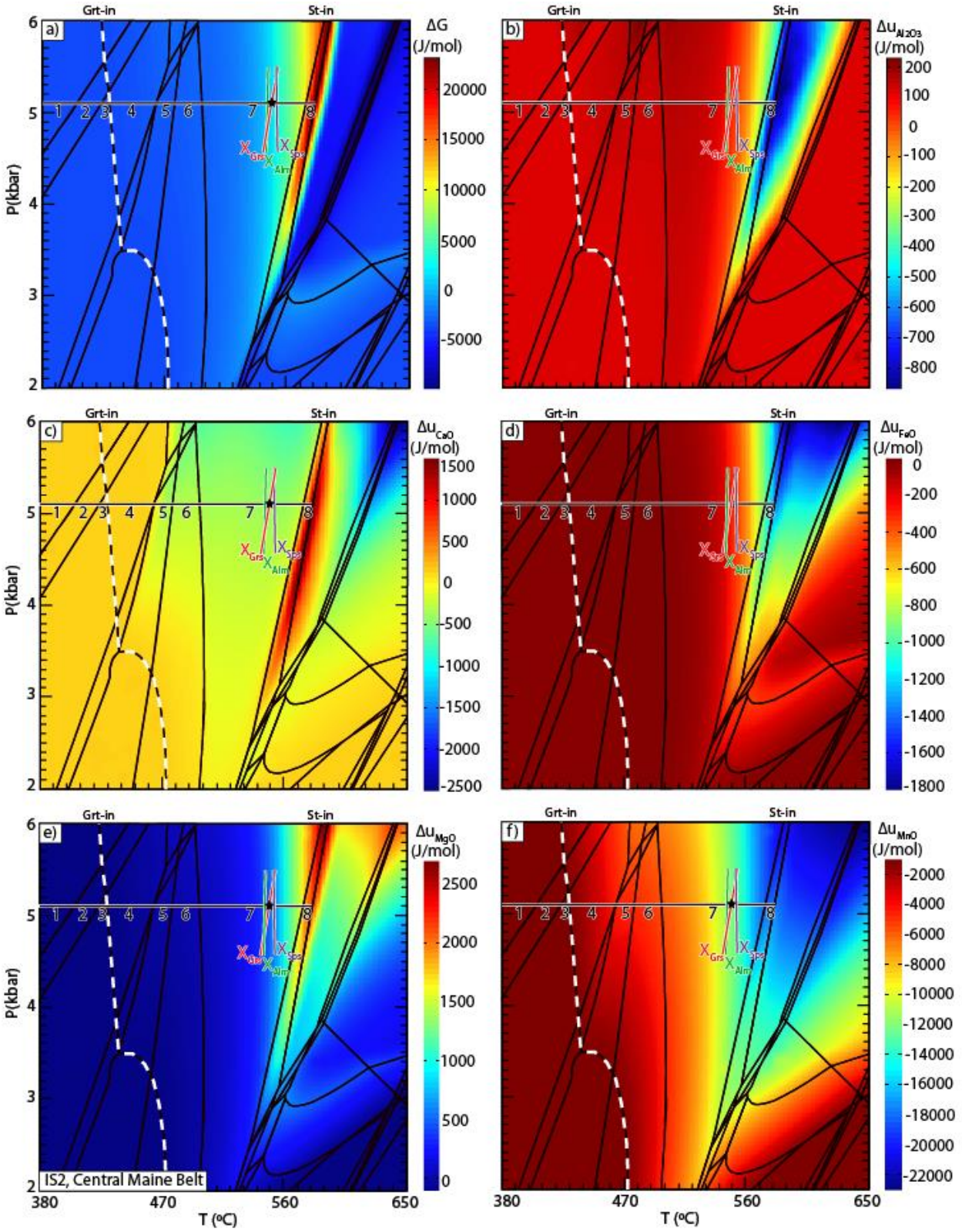

Figure 2.3. P-T maps of the difference between system properties for the garnet and staurolite allowed phase diagram calculation vs. excluded calculation for sample IS2 from the Central

Maine Belt. Phase stability fields, isobaric traverse line (with numbered stability fields), and the "chemical-in" from Figure 2.2 are superimposed. (a) ΔG, (b) $\Delta\mu_{Al2O3}$, (c) $\Delta\mu_{CaO}$, (d) $\Delta\mu_{FeO}$, (e) $\Delta\mu_{MgO}$ and (f) $\Delta\mu_{MnO}$

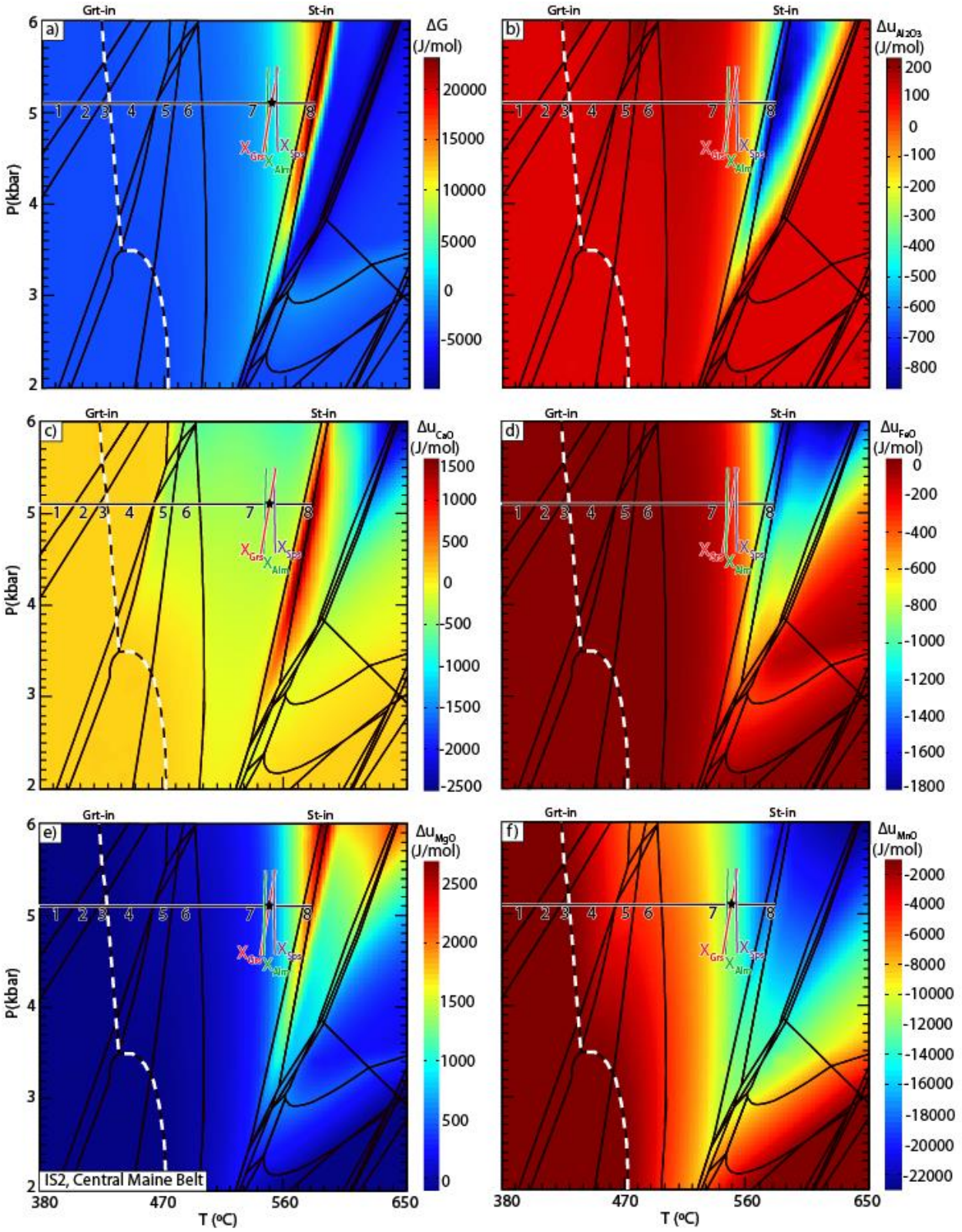

Figure 2.4. P-T maps of the difference between system properties for the garnet and staurolite allowed phase diagram calculation vs. excluded calculation for sample IS2 from the Central

Maine Belt. Phase stability fields, isobaric traverse line (with numbered stability fields), and the "chemical-in" from Figure 2.2 are superimposed. (a) Entropy, (b) ΔAlbite, (c) ΔBiotite, (d) ΔChlorite, (e) ΔWhite Mica and (f) ΔZoisite.

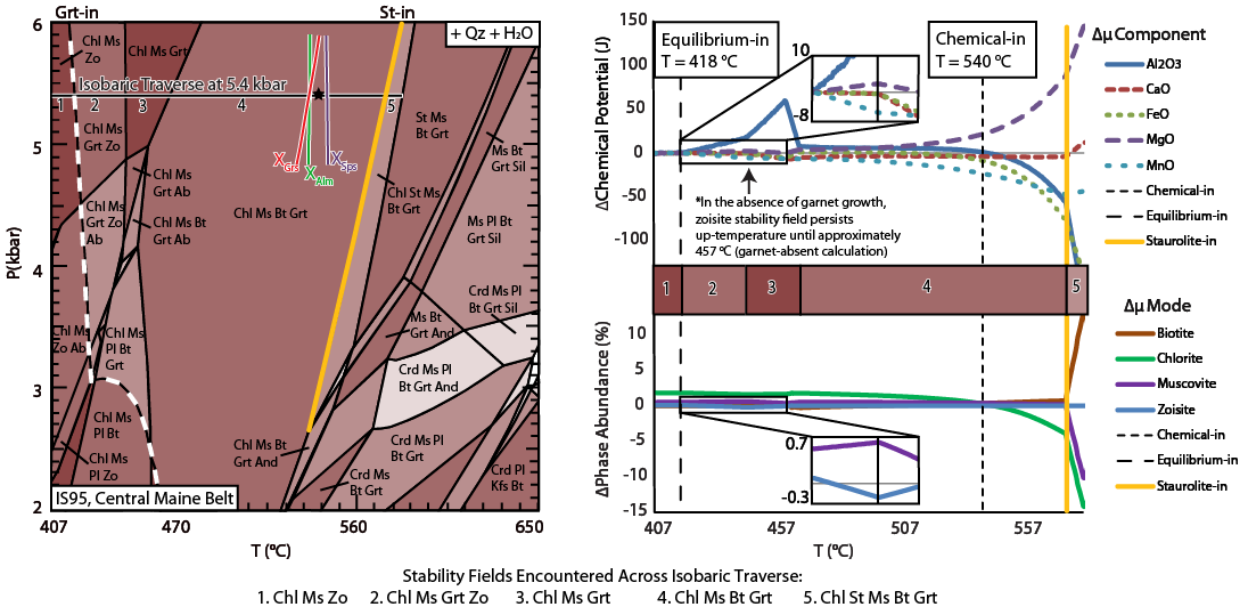

Figure 2.5. All data for sample IS95 from the Central Maine Belt. On phase diagram, dashed line represents the equilibrium predicted garnet-in reaction boundary and star represents the "chemical-in", determined using the intersection of core isopleths (labeled). The top graph (right) displays the chemical potential difference of all major garnet forming oxides, normalized to the mol% of each oxide present in the chemical system and the bottom graph represents the volume percent difference in phases. On phase diagram, increasingly darker shades of color represent domains of increasing Gibbs phase rule variancy and mineral abbreviations are according to Whitney and Evans (2010).

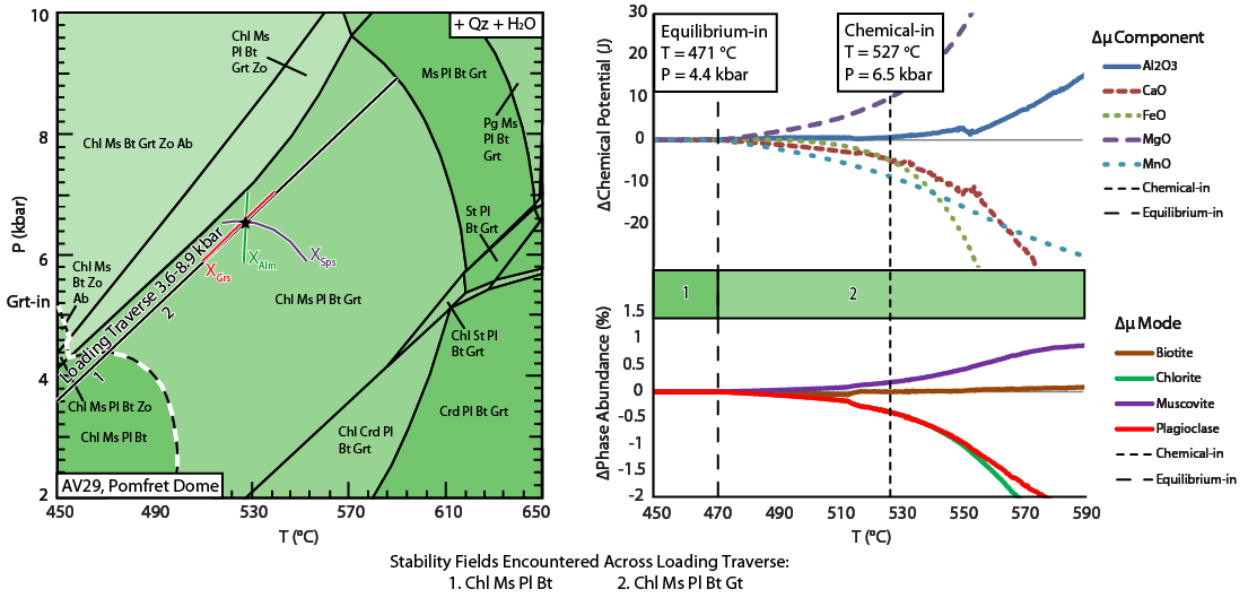

Figure 2.6. All data for sample AV29 from the Pomfret Dome. On phase diagram, d dashed line represents the equilibrium predicted garnet-in reaction boundary and star represents the "chemical-in", determined using the intersection of core isopleths (labeled). The top graph (right) displays the chemical potential difference of all major garnet forming oxides, normalized to the mol% of each oxide present in the chemical system and the bottom graph represents the volume percent difference in phases. On phase diagram, increasingly darker shades of color represent domains of increasing Gibbs phase rule variancy and mineral abbreviations are according to Whitney and Evans (2010). *White Mica to indicate composition is muscovite (K^+) dominant at low temperatures and paragonite (Na^+) dominant at high temperatures.

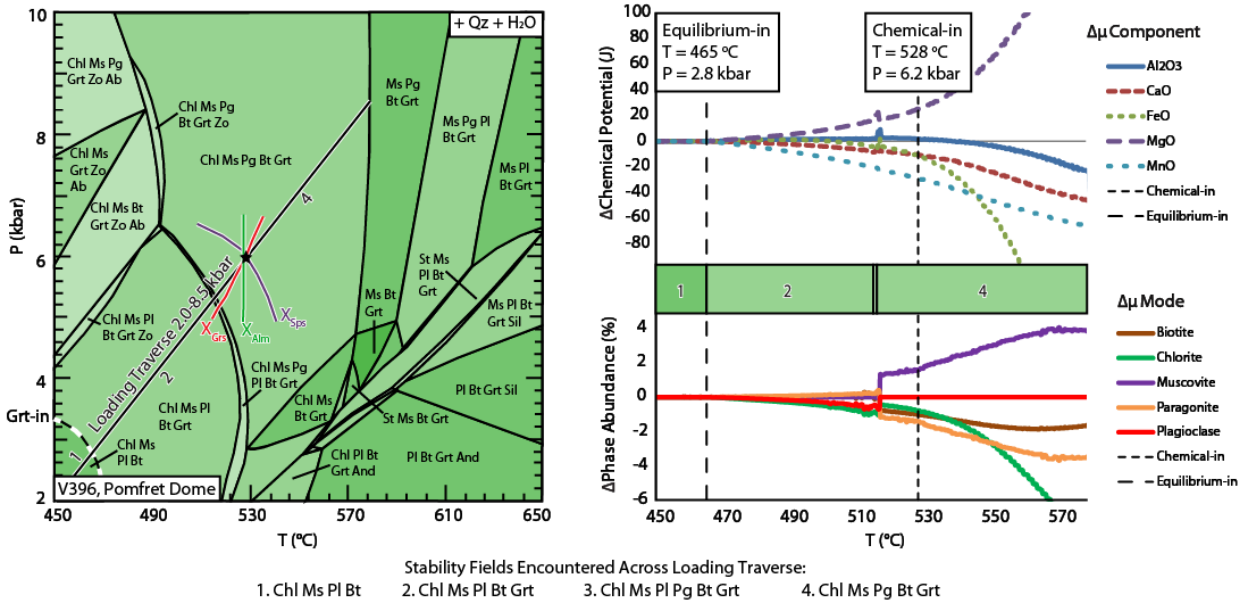

Figure 2.7. All data for sample V396 from the Pomfret Dome. On phase diagram, dashed line represents the equilibrium predicted garnet-in reaction boundary and star represents the

"chemical-in", determined using the intersection of core isopleths (labeled). The top graph (right) displays the chemical potential difference of all major garnet forming oxides, normalized to the mol% of each oxide present in the chemical system and the bottom graph represents the volume percent difference in phases. On phase diagram, increasingly darker shades of color represent domains of increasing Gibbs phase rule variancy and mineral abbreviations are according to Whitney and Evans (2010).

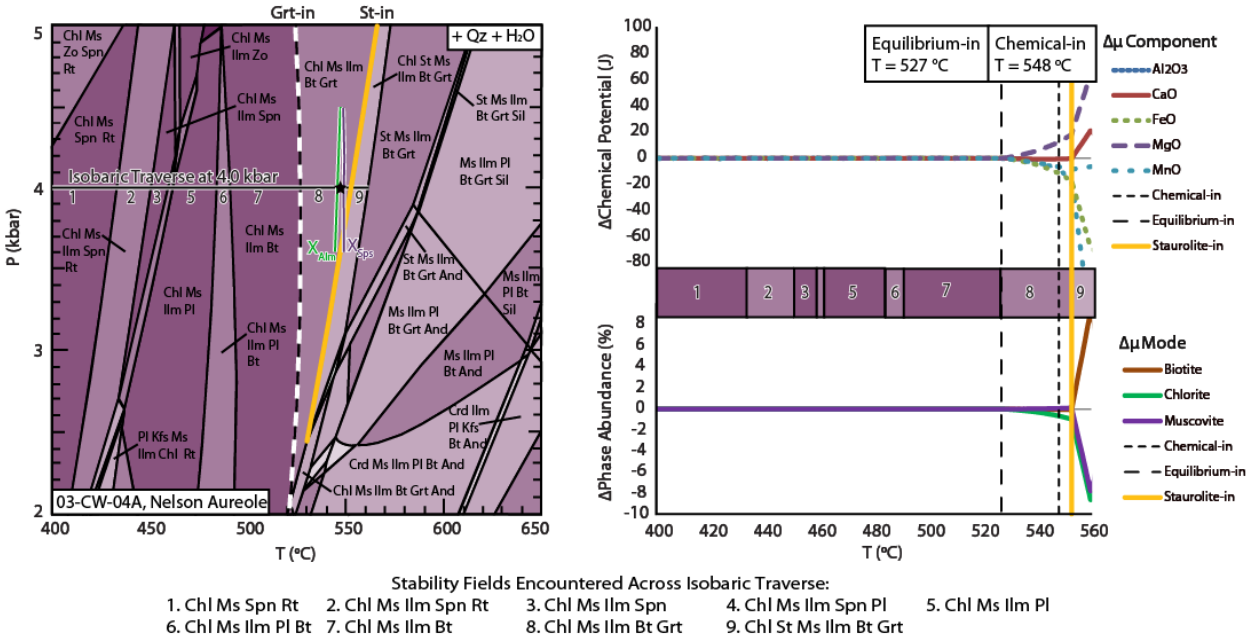

Figure 2.8. All data for sample 03-CW-04A from the Nelson Aureole. On phase diagram, dashed line represents the equilibrium predicted garnet-in reaction boundary and star represents the "chemical-in", determined using the intersection of core isopleths (labeled). The top graph (right) displays the chemical potential difference of all major garnet forming oxides, normalized to the mol% of each oxide present in the chemical system and the bottom graph represents the volume percent difference in phases. On phase diagram, increasingly darker shades of color represent domains of increasing Gibbs phase rule variancy and mineral abbreviations are according to Whitney and Evans (2010).

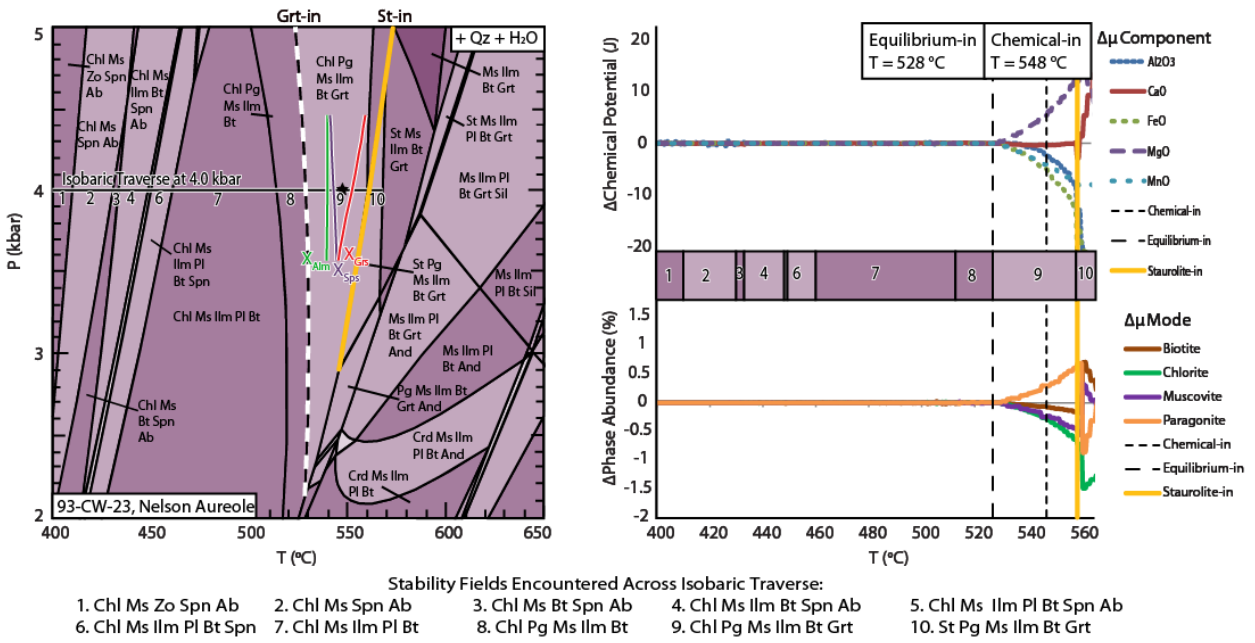

Figure 2.9. All data for sample 93-CW-23 from the Nelson Aureole. On phase diagram, dashed line represents the equilibrium predicted garnet-in reaction boundary and star represents the "chemical-in", determined using the intersection of core isopleths (labeled). The top graph (right) displays the chemical potential difference of all major garnet forming oxides, normalized to the mol% of each oxide present in the chemical system and the bottom graph represents the volume percent difference in phases. On phase diagram, increasingly darker shades of color represent domains of increasing Gibbs phase rule variancy and mineral abbreviations are according to Whitney and Evans (2010).

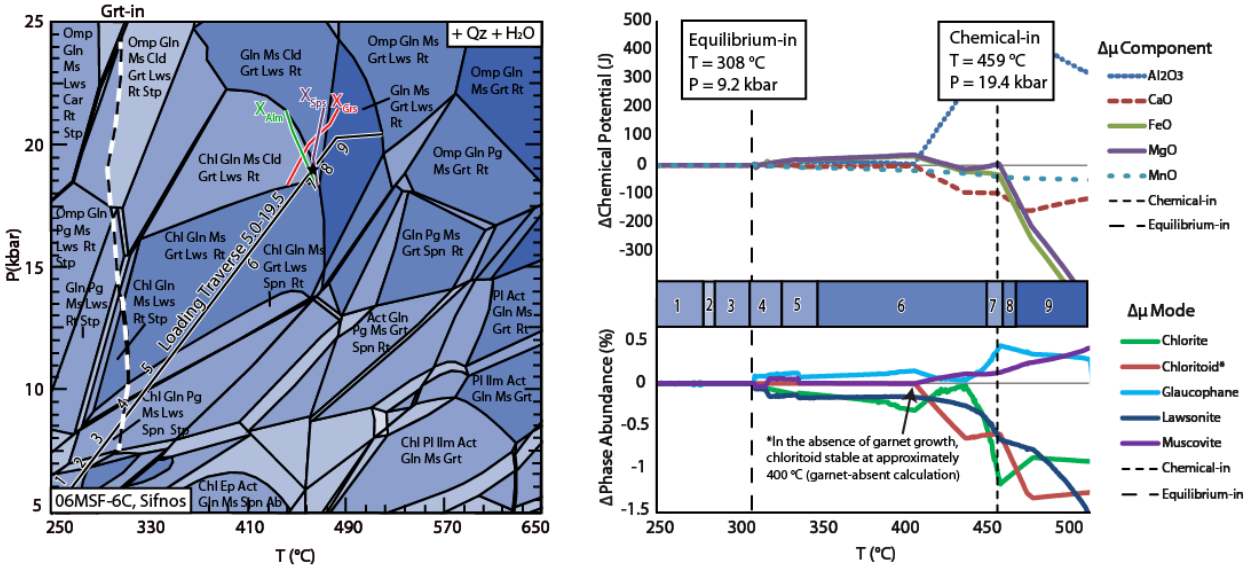

Figure 2.10. All data for sample 06MSF-6C from Sifnos. On phase diagram, dashed line represents the equilibrium predicted garnet-in reaction boundary and star represents the "chemical-in", determined using the intersection of core isopleths (labeled). The top graph (right) displays the chemical potential difference of all major garnet forming oxides, normalized to the mol% of each oxide present in the chemical system and the bottom graph represents the volume percent difference in phases. On phase diagram, increasingly darker shades of color represent domains of increasing Gibbs phase rule variancy and mineral abbreviations are according to Whitney and Evans (2010).

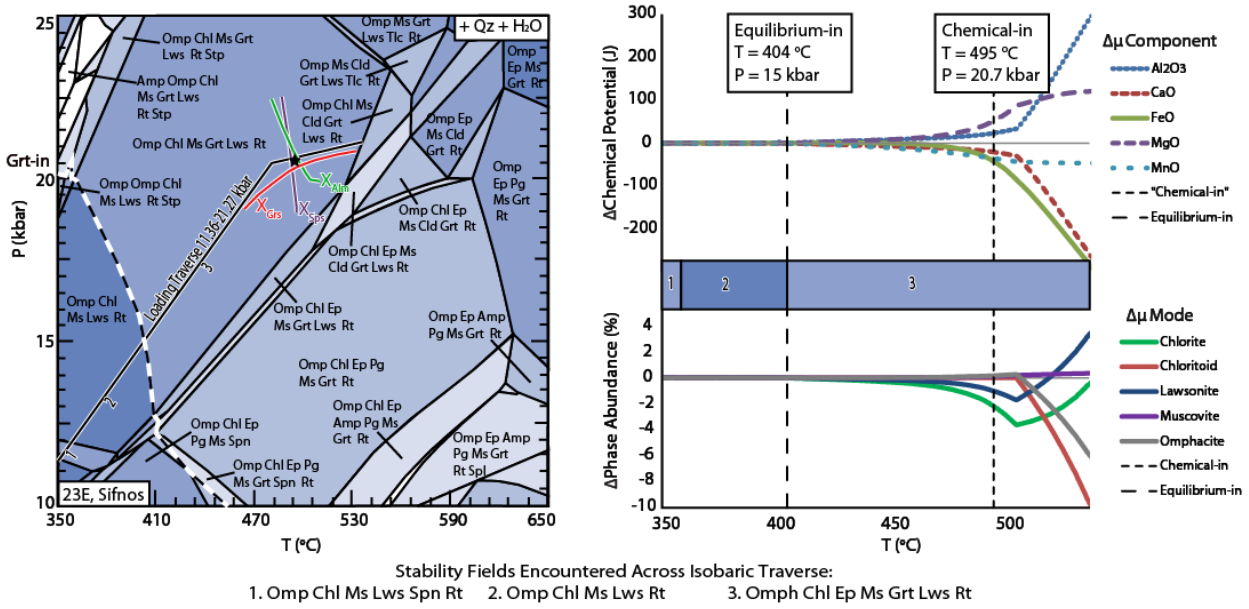

Stability Fields Encountered Across Isobaric Traverse:
1. Omp Chl Ms Lws Spn Rt 2. Omp Chl Ms Lws Rt 3. Omph Chl Ep Ms Grt Lws Rt

Figure 2.11. All data for sample 23E from Sifnos. On phase diagram, dashed line represents the equilibrium predicted garnet-in reaction boundary and star represents the "chemical-in", determined using the intersection of core isopleths (labeled). The top graph (right) displays the chemical potential difference of all major garnet forming oxides, normalized to the mol% of each oxide present in the chemical system and the bottom graph represents the volume percent difference in phases. On phase diagram, increasingly darker shades of color represent domains of increasing Gibbs phase rule variancy and mineral abbreviations are according to Whitney and Evans (2010).

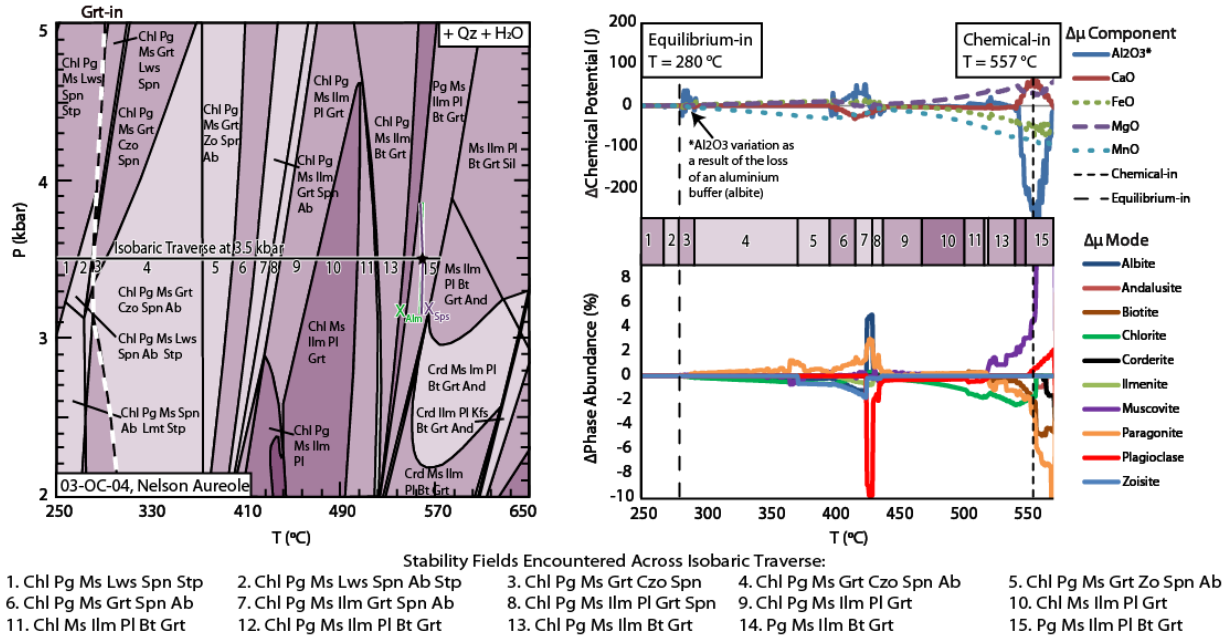

Stability Fields Encountered Across Isobaric Traverse:

1. Chl Pg Ms Lws Spn Stp
2. Chl Pg Ms Lws Spn Ab Stp
3. Chl Pg Ms Grt Czo Spn
4. Chl Pg Ms Grt Czo Spn Ab
5. Chl Pg Ms Grt Zo Spn Ab
6. Chl Pg Ms Grt Spn Ab
7. Chl Pg Ms Ilm Grt Spn Ab
8. Chl Pg Ms Ilm Pl Grt Spn
9. Chl Pg Ms Ilm Pl Grt
10. Chl Ms Ilm Pl Grt
11. Chl Ms Ilm Pl Bt Grt
12. Chl Pg Ms Ilm Pl Bt Grt
13. Chl Pg Ms Ilm Bt Grt
14. Pg Ms Ilm Bt Grt
15. Pg Ms Ilm Pl Bt Grt

Figure 2.12. All data for sample 03-OC-04 from the Nelson Aureole. On phase diagram, dashed line represents the equilibrium predicted garnet-in reaction boundary and star represents the "chemical-in", determined using the intersection of core isopleths (labeled). The top graph (right) displays the chemical potential difference of all major garnet forming oxides, normalized to the mol% of each oxide present in the chemical system and the bottom graph represents the volume percent difference in phases. On phase diagram, increasingly darker shades of color represent domains of increasing Gibbs phase rule variancy and mineral abbreviations are according to Whitney and Evans (2010).

Sample Locality/ Aureole	Published Chemical System	Published Mixing Models	Published P-T Constraints	Perple_X Chemical System	Perple_X Mixing Models	Perple_X P-T Constraints
Central Maine Belt	Na_2O-CaO-MnO-K_2O-FeO-MgO-Al_2O_3-SiO_2-H_2O	(Holland and Powell, 1998), including the update (Holland and Powell, 2003); (Tinkham et al., 2001), (White, 2001), feldspar (Holland and Powell, 2003), and white mica (Coggon and Holland, 2002)	2-6 kbar, 430-650°C	Na_2O-CaO-MnO-K_2O-FeO-MgO-Al_2O_3-SiO_2-H_2O	Biotite (Powell and Holland, 1999), chlorite (Holland et al., 1998), cordierite (Powell and Holland, 1990) with update (Mahar et al., 1997), feldspar (Holland and Powell, 2003), garnet (White et al., 2005), staurolite (Powell and Holland, 1990) with update (Mahar et al., 1997), white mica (Coggon and Holland, 2002), H_2O in excess	2-6 kbar, 380-650°C (IS2) 2-6 kbar, 407-650°C (IS95)
Pomfret Dome	See above	None	2-10 kbar, 450-650°C	See above	See above	2-10 kbar, 450-650°C
Nelson Aureole	None	None	None	See above with the addition of TiO_2	See above with the addition of ilmenite (ideal*)	2-5 kbar, 400-650°C; 250-650°C for (03-OC-04)
Sifnos 06MSF-6C	Na2O-CaO-MnO-K_2O-FeO-Fe_2O_3-MgO-Al_2O_3-SiO_2-H_2O-TiO_2	Ca- and Na-amphibole (Dale et al., 2000), chlorite (Holland et al., 1998), chloritoid (Smye et al., 2010), epidote (Holland and Powell, 1998), feldspar (Fuhrman and Lindsley, 1988), Fe-oxides (Andersen and Lindsley, 1988), garnet (White et al., 2005), omphacite (Green et al., 2007), white mica (Smye et al., 2010), H2O in excess	10-25 kbar; 400-650°C	Na2O-CaO-MnO-K_2O-FeO-Fe_2O_3-MgO-Al_2O_3-SiO_2-H_2O-TiO_2	Ca- and Na-amphibole (Dale et al., 2000), chlorite (Holland et al., 1998), chloritoid (Smye et al., 2010), epidote (Holland and Powell, 1998), feldspar (Fuhrman and Lindsley, 1988), Fe-oxides (Andersen and Lindsley, 1988), garnet (White et al., 2005), omphacite (Green et al., 2007), white mica (Smye et al., 2010), H2O in excess	5-25 kbar, 250-650°C
Sifnos 23E	None	None	None	See above	Amphibole (Dale et al., 2005), chlorite (Holland et al., 1998), chloritoid (Smye et al., 2010), epidote (Holland and Powell, 1998), feldspar (Holland and Powell, 2003), garnet (White et al., 2005), ilmenite (*ideal) omphacite (Green et al., 2007), white mica (Coggon and Holland, 2002), H_2O in excess	10-25 kbar, 350-650°C

Table 2.1. Published data (if any) for the samples used in this study and the chemical system, mixing models, and P-T constraints used to calculate the phase diagrams presented in this paper using Perple_X (Connolly, 1990; Connolly and Petrini, 2002). Published phase diagrams for the Central Maine Belt and Pomfret Dome were calculated using Thermocalc (Powell and Holland, 1988). Only Sanislav and Bell (2011) report phases considered: chlorite, zoisite, muscovite, plagioclase, biotite, garnet, staurolite, andalusite, sillimanite, kyanite, cordierite, and H_2O. The only Sifnos sample with a published phase diagram (06MSF-6C) was also calculated using Perple_X and therefore our phase diagrams should be identical except for the slight change in P-T conditions imposed. *ilmenite mixing model used was an ideal ilmenite-geikielite-pyrophanite ternary solution.

Sample Name	IS2	IS95	AV29	V396	03-OC-04	03-CW-04A	93-CW-23	06MSF-6C	23E
Locality/ Aureole	Central Maine Belt	Central Maine Belt	Pomfret Dome	Pomfret Dome	Nelson Aureole	Nelson Aureole	Nelson Aureole	Sifnos	Sifnos
SiO_2	62.140	60.370	73.200	60.000	53.620	62.320	64.720	53.150	50.740
TiO_2	-	-	-	-	1.250	0.930	0.830	1.070	1.150
Al_2O_3	19.230	19.460	11.920	17.300	23.860	20.030	17.530	13.770	17.940
FeO	7.063	7.430	4.140	9.360	6.250	5.780	5.660	9.987	7.955
Fe_2O_3	-	-	-	-	-	-	-	4.150	4.740
MnO	0.150	0.190	0.090	0.200	0.490	0.090	0.080	0.140	0.160
MgO	2.170	2.580	2.110	2.630	2.020	1.710	1.740	5.650	5.070
CaO	0.500	0.320	1.920	0.930	1.490	0.660	0.740	2.720	8.800
Na_2O	0.600	0.380	2.770	1.220	1.760	0.610	0.760	5.300	2.850
K_2O	4.000	4.460	1.380	3.130	3.730	4.090	4.090	0.990	1.080
X_{Grs}	0.067	0.068	0.277	0.173	0.031	0.035	0.059	0.145	0.180
X_{Alm}	0.749	0.676	0.511	0.648	0.643	0.771	0.688	0.666	0.690
X_{Sps}	0.094	0.166	0.176	0.137	0.217	0.105	0.160	0.118	0.080

Table 2.2. Whole-rock compositions used for phase diagram modeling for each sample and garnet core compositions in mole fraction used for core isopleth calculations. If Fe_2O_3 was originally published in the whole rock composition for a sample (Central Maine Belt, Pomfret Dome and Nelson Aureole), these values were converted to weight percent FeO in order to calculate phase diagrams. TiO_2 and Fe_2O_3 were only included for samples if these oxides were used to create phase diagrams (Nelson Aureole and Sifnos samples).

Name	Phases	ΔVol%	ΔSiO2	ΔAl_2O_3	ΔFeO	ΔMnO	ΔMgO	ΔCaO	ΔNa_2O	ΔK_2O	ΔH_2O
IS2	Biotite	-0.14	0.01787	-0.01787	-0.0512	-0.02544	0.09451	0	0	0	0
	Chlorite	-1.64	0.00334	-0.00334	-0.09221	-0.05934	0.1549	0	0	0	0
IS95	Biotite	-0.02	0.00797	-0.00797	-0.02218	-0.02697	0.05712	0	0	0	0
	Chlorite	-1.11	0.0025	-0.0025	-0.03585	-0.05944	0.09779	0	0	0	0
AV29	Biotite	0	0.00193	-0.00193	-0.0164	-0.02024	0.03857	0	0	0	0
	Chlorite	-0.38	0.00119	-0.00119	-0.03202	-0.03944	0.07265	0	0	0	0
V396	Biotite	-1.17	0.00663	-0.00663	-0.02899	-0.03008	0.06571	0	0	0	0
	Chlorite	-0.77	0.00193	-0.00193	-0.04584	-0.06196	0.10973	0	0	0	0

Name	Phases	ΔVol%	ΔSiO2	ΔTiO_2	ΔAl_2O_3	ΔFeO	ΔMnO	ΔMgO	ΔCaO	ΔNa_2O	ΔK_2O	ΔH_2O
03-CW-04A	Biotite	-0.04	0.00825	0.00219	-0.01262	-0.03756	-0.00522	0.05103	0	0	0	0
	Chlorite	-0.65	0.00122	0	-0.00122	-0.06432	-0.01399	0.07952	0	0	0	0
93-CW-23	Biotite	-0.08	0.00263	0.00129	-0.0052	-0.01713	-0.00452	0.02426	0	0	0	0
	Chlorite	-0.3	0.00089	0	-0.00089	-0.02614	-0.01131	0.03834	0	0	0	0
03-OC-04	Biotite*	-1.97	0.0476	0.01332	-0.07426	-0.10069	-0.04439	0.19269	0	0	0	0

Name	Phases	ΔVol%	ΔSiO2	ΔTiO_2	ΔAl_2O_3	ΔFeO	ΔFe_2O_3	ΔMnO	ΔMgO	ΔCaO	ΔNa_2O	ΔK_2O	ΔH_2O
06MSF-6C	Chlorite	-1.03	-0.00236	0	0.00236	0.11493	0	-0.20771	0.09043	0	0	0	0
23E	Chlorite	-2.19	0.00047	0	-0.00047	-0.14479	0	-0.06083	0.20608	0	0	0	0

Table 2.3. Volume percent difference in biotite and chlorite at the chemical-in conditions for each sample followed by the compositional changes in each phase between the allowed vs. excluded phase diagram calculations for each sample. Molar proportions are included for all oxides present in the respective chemical system used to thermodynamically model each sample (see Table 2.1). *Indicates that only biotite (03-OC-04) or only chlorite (Sifnos) was present in the phase diagrams at the chemical-in conditions and included in the above table.

CHAPTER 3

Metamorphic Differentiation of the Haimanta Group Metasediments, Sutlej Valley, northwestern India: Implications for Microstructural Evolution

McCall, K.E., Caddick, M.J., and Law, R.D.

Abstract

Thin sections taken from Haimanta Group rocks, exposed in the eastern part of the Sutlej valley, NW Indian Himalaya, contain quartz-rich and mica-rich layers, with numerous garnet porphyroblasts appearing solely in the quartz-rich layers. We propose that these layers formed as the result of metamorphic differentiation, wherein protracted deformation leads to formation of a secondary foliation (S_2) along the axial planes of an earlier (S_1) foliation. We explain the presence of garnet porphyroblasts in the quartz-rich layers as recording the release of strain energy stored in the crenulated (S_1) foliation as the new, axial planar S_2 foliation developed.

The Elle Microstructural Modeling Program, Basil deformation code, and chemical zoning of garnet porphyroblasts were used to test metamorphic differentiation as the process responsible for these observed microstructures. Model results indicate that stress differences may have driven the metamorphic differentiation process and resulting dissolution and re-precipitation of quartz grains. We conclude that garnet growth only initiated during the (S_1-S_2) foliation transition, with no strong evidence for a high-grade (porphyroblast forming) pre-Himalayan metamorphic event unrelated to this deformation. This is in agreement with published monazite ages for these samples that also yield a Himalayan age for sampled garnets.

1. Introduction

Cambro-Ordovician to- Tertiary metasedimentary rocks forming the stratigraphically younger part of the Tethyan Sedimentary Series (TSS) are the structurally highest units within the Himalayan orogen. The TSS has been described by numerous authors as an unmetamorphosed to low-grade metamorphosed sequence (Harris and Massey, 1994; Godin et al., 2006; Aikman et al., 2008; Chambers et al., 2009), but in parts of the western Himalaya the basal unit of the TSS, the Haimanta Group, includes pelites metamorphosed up to amphibolite facies (e.g. Chambers et al., 2009). As the earliest orogen-wide units to be accreted to Asia, they are uniquely placed to retain information on the formative stages of Himalayan orogenesis (Aikman et al., 2008). However, deciphering their metamorphic evolution requires the interpretation that mineral phases reflect equilibration during the Himalayan orogen, with

microstructural observations suggesting that porphyroblast growth was controlled equally by deformational and thermal parameters.

A group of Haimanta Group metapelitic thin sections taken from the eastern part of the Sutlej Valley, northwest India, contain microstructures that are not consistent with normal petrographic observations and cannot readily be explained by simple, rock-wide equilibrium growth models. Distinct quartz-rich and mica-rich layering is present, with numerous garnet porphyroblasts appearing solely in the quartz-rich layers (Figures 3.1 and 3.2). This is contrary to typical observations that garnet porphyroblasts form in mineralogically nutrient-rich domains (Carlson et al. 1995; Carlson, 2011). The quartz-rich and mica-rich layers could either be a reflection of relict bedding or the product of metamorphic differentiation, the process by which a compositionally distinct, heterogeneous layering of alternating bands of contrasting mineralogy and/or fabric develop in metamorphic rocks undergoing deformation (Williams, 1972; Dewers and Ortoleva, 1990).

Pressure shadows, formed when dissolved silica created by pressure solution is transported from areas of high stress and precipitated adjacent to rigid grains (e.g. garnet crystals) are commonly observed in metamorphic tectonites. The microstructures preserved in the Haimanta Group samples appear to be similar to this pressure shadow effect, but while some garnet porphyroblasts display what appears to be a simple "pressure shadow" relationship with surrounding quartz grains (e.g. right side of garnet porphyroblast, Figure 3.1b and Figure 3.2b), other garnets are present within distinct, continuous quartz bands that are not confined to the areas immediately surrounding garnet porphyroblasts (Figures 3.1 and 3.2). The simplest conclusion is that garnets grew within these nutrient-poor domains, although the reasons for this are not immediately evident.

Our goal here is to use these microstructures to determine the tectono-metamorphic evolution of the Haimantas in one of the few areas where metamorphism reached a sufficiently high grade for the deformation history to be preserved by porphyroblast mineral phases. Chambers et al. (2009) published monazite ages that constrained timing of garnet growth in the Haimanta Group of the eastern Sutlej Valley as late as Oligocene to early Miocene. However, the Haimanta Group/TSS rocks from which these samples were collected are proximal to the Apka Granite, dated at ~ 480 Ma (Miller et al., 2001), raising the possibility that a metamorphic 'pre-print' may also be recorded. In the underlying Greater Himalayan Sequence, evidence suggests

pre-Himalayan tectono-metamorphic events associated with the ~ 500 Ma magmatic activity (Marquer et al., 2000; Thöni et al., 2012), and it is important to assess whether this may also be responsible for metamorphism of the overlying TSS. A major question addressed in this paper is then: are the garnet porphyroblasts present exclusively in quartz-rich layers a consequence of Himalayan deformation or unrelated to it, and can a genetic link be established between deformation and the spatial ordering of porphyroblasts?

The process of metamorphic differentiation is usually considered to initiate at sites of small initial inhomogenities, e.g. in originally slightly differentiated and/or layered sediments (Winter, 2010). We tested this with the microstructural simulation program Elle by creating a generic initial microstructure wherein the upper half of the numerical model was slightly segregated into thin-section scale quartz-rich and mica-rich layers and the lower half was composed of a heterogeneous mineral assemblage. This was done to ensure that if metamorphic differentiation (layering) developed during subsequently simulated deformation, it should only be present in the top portion of the model and not in the lower, heterogeneous portion. To our knowledge this is the first instance in which the Elle program has been used to study deformation in a complex polycrystalline aggregate composed of a heterogeneous distribution of mineral grains with markedly contrasting mechanical properties. Specifically, the complex numerically modeled system constructed contains 469 quartz grains and 436 micaceous grains in varying layer configurations. We then used the Basil deformation code to induce simple shear deformation over ~3,000,000 years at commonly cited average geologic strain rates (1×10^{-13} s^{-1}) and studied the resulting microstructural evolution.

We attempt to address the issue of natural garnet crystals occurring in quartz-rich layers by first numerically determining whether or not the microstructural driving force postulated for layer formation (metamorphic differentiation) can occur upon deformation at Himalayan strain rates and timescales. The numerical modeling parameters we track are stress, strain rate and dislocation density. Calculated stress values are examined to determine if the stress differences theorized to drive metamorphic differentiation do arise upon induced deformation, due to mineralogical heterogeneities. Next, measured strain rate and dislocation density values, used as a proxy for strain energy across the deforming microstructure, are examined to determine if the heterogeneous mineralogy could also lead to areas with different potential for garnet nucleation. More specifically, the areas in the microstructure with the highest values of strain rate and

dislocation density are related to the areas in the microstructure with the largest potential for garnet nucleation (the hypothesized fold hinges of the S_1 foliation), represented by the mica-rich layers in the numerical model.

Petrologic relationships are also used to determine if the observed mica-rich and quartz-rich layers formed as a result of Himalayan deformation and if so, could this differentiation (layering) have formed around pre-existing garnet crystals from an earlier (pre-Himalayan) metamorphic event. Lastly, chemical maps using the Energy Dispersive Spectrometer (EDS) of the Electron Microprobe are analyzed to search for evidence of multiple growth events preserved in the zoning patterns of garnet crystals.

2. Metamorphic Differentiation Theory and Proposed Microstructure Development

In their review of the thermodynamics of deformed metamorphic rocks (Hobbs et al., 2011) show through a combination of the first and second law of thermodynamics, that at tectonic strain-rates (1×10^{-12} s^{-1}), a body of rock up to about a meter in size remains approximately isothermal, so that the energy equation reduces to a set of coupled reaction-diffusion-deformation equations. These coupled chemical reactions are thought to cause chemically unstable behavior, leading to metamorphic differentiation and/or compositional zoning in growing mineral grains. On the larger scale, of about 1-100 m, the heat generated in a system by any dissipative process (e.g. deformation) diffuses out of a system in 10^6-10^{10}seconds, thus making the rock volume non-isothermal. Therefore no metamorphic differentiation should arise from reaction-diffusion processes at larger length-scales, unless the flux is aided by mass transport in a fluid (Hobbs et al., 2011).

A fundamental outcome of microstructures that form due to these coupled reaction-diffusion-deformation processes is that they are controlled in their orientation by the deformation rate tensor, and not the strain tensor. Thus, these fabrics reflect the symmetry of the kinematics and not geometrical aspects defined by strain (Hobbs et al., 2011; Sander, 1911) and can therefore be used as kinematic indicators in determining P-T-t history analysis. This allows us to use the microstructures (metamorphic differentiation) recorded in the Haimanta Group metasediments to make conclusions about the overall tectonic evolution of these rocks.

The driving force of the metamorphic differentiation process has been described in the literature as resulting from a difference in stress, pressure or in chemical potential between the limb and hinge regions of a crenulated foliation (Cosgrove, 1972, 1976; Williams, 1972; Stephansson, 1973; Vidale, 1974; Fletcher, 1977). The average stress acting on the more mobile phase (quartz) is different in these two regions because the mean stress on a grain is dependent upon the strength of the surrounding material, thus a quartz grain will have a lower mean stress imposed upon it if it is surrounded by (strong) quartz-rich material as opposed to (weaker) micaceous material (Cosgrove, 1976; Fletcher, 1977; Hobbs et al., 2011). A "stronger" phase, in this context implies one with greater elastic constants or greater resistance to intercrystalling slip (Dewers and Ortoleva, 1990). Chemical potential gradients develop in response to the difference in the mean stresses acting on the mobile solid phase in the hinge and limb regions of a crenulation (Fletcher, 1977), driving the metamorphic differentiation process and creating a positive feedback mechanism (Figure 3.3).

Here, we propose that during Himalayan (Tertiary) age deformation, compressional regional stresses resulted in crenulations or "kink" folds developing in an initially slightly segregated sedimentary protolith (S_1 foliation), that upon increased deformation led to a new foliation developing along the axial plane of the folded sediments (S_2) due to metamorphic differentiation processes (Figure 3.4). In fine-grained metamorphic rocks, small scale folds often develop in response to compressional stresses and we suggest that the presence of garnet porphyroblasts in quartz-rich layers can be explained by the release of strain energy, which may be key to the kinetics of garnet nucleation and growth during regional metamorphism (Gaidies et al., 2011), as the "kink" folds were overprinted and a new, axial planar foliation developed along the fold hinges as a result of metamorphic differentiation processes (Figure 3.4). We were unable to directly model the formation of crenulations or "kink" folds and the resulting axial planar foliation due to the limitation that only simple shear deformation was modeled in the studied microstructural evolution. Due to this, numerical modeling results can provide evidence for the driving forces of the metamorphic differentiation process, but the proposed deformation history of the Haimanta Group cannot be exactly re-created (i.e. crenulations did not form in the modeled microstructural evolution).

3. Evolution of the NW Himalaya (Metasediments of the Haimanta Group)

The Himalayan orogen was created by continent-continent (India-Asia) collision starting at ca. 50 Ma (Yin and Harrison, 2000; Ding et al., 2005; Zhu et al., 2005; Aitchison et al., 2007; Yin et al., 2010). The main tectonic discontinuities recognized in the central-eastern Himalaya are: the Main Boundary Thrust along which Lesser Himalayan Sequence rocks are placed over Tertiary sedimentary rocks, the Main Central Thrust along which the Greater Himalayan Sequence of metamorphic rocks is placed over the Lesser Himalayan Sequence, and the South Tibet Detachment along which the Tethyan Sedimentary Series is down-faulted against the underlying Greater Himalayan Sequence (Figure 3.5). The Tethyan Sedimentary Series (TSS) was tectonically separated from the underlying Greater Himalayan Sequence (GHS) during the Miocene by motion on the South Tibetan Detachment (STD), and records a protracted and complex history of deformation (Chambers et al., 2009). In the central Himalaya, the TSS is bounded to the north by the south-dipping Great Counter Thrust (GCT) and to the south by the north-dipping STD, and is commonly described as a deformed package of predominantly low-grade Paleoproterozoic to Eocene metasediments thought to have been deposited along the northern edge of the India continent (Brookfield, 1993; Liu and Einsele, 1994; Aikman et al., 2008).

In the TSS, the first phase of regional deformation is indicated by broadly E-W trending (NW-SE in the western Himalaya) isoclinal folds associated with a penetrative axial planar schistosity that most workers ascribe to Tertiary structural loading (Aikman et al., 2008). Folding and related cleavage development in these units completely transposed the original bedding during this early contractional event, as preserved in fine-grained metasedimentary rocks (Yin et al., 2010). The Haimanta Group, outcropping in the eastern part of the Sutlej Valley, northwest India, make up the basal unit of the TSS (Figure 3.6) and represent a thick succession of Proterozoic to early-Paleozoic chlorite-to-amphibolite-grade gneisses, schists and phyllites (Caddick, 2005). The Haimanta Group is intruded by the Apka Granite, a 480 Ma granitoid, with metamorphic grade decreasing away from the Apka Granite that lies in structural contact with the underlying STD (Miller et al., 2001; Caddick, 2005). Metamorphic grade traced up structural section in the Haimantas (Figure 3.6b) decreases from kyanite-staurolite-garnet mica schists at

the contact with the underlying granite, to greenschist facies rocks (Thakur and Tripathi, 2008; Chambers et al., 2009).

Th-Pb dating of monazites indicate that prograde metamorphism and peak conditions in GHS rocks near our study area (ES, Figure 3.6a) occurred at 40-22 Ma (Vannay et al., 2004; Caddick, 2005), although pre-Himalayan metamorphic mineral assemblages are locally preserved (Marquer et al., 2000; Thöni et al., 2012). Pre-Himalayan metamorphism in the GHS associated with ~ 500 Ma magmatic activity is overprinted by Tertiary metamorphism that produced garnet, monazite and zircon, as reported by Argles et al. (1999); Marquer et al. (2000); Godin et al. (2001); Catlos et al. (2002); Martin et al. (2007); and Thöni et al. (2012). To our knowledge, no isotopic evidence for pre-Himalayan metamorphism has been found in the overlying TSS.

3.1 Are Garnets in the Haimanta the Product of Himalayan Metamorphism?

Chambers et al. (2009) presented monazite ages of 34-28 Ma to constrain timing of garnet growth in the Haimanta Group and interpreted growth to have occurred during prograde Barrovian metamorphism at 610-620 °C and 7-8 kbars. Garnet was interpreted to have overgrown an early tectonic fabric (S_1), and decompression during heating to 640-660 °C at 6-7 kbars was associated with development of a pervasive crenulation cleavage (S_2). Our suggestion that the quartz-rich layers containing garnet porphyroblasts in the Haimantas may be the result of metamorphic differentiation processes and formation of the (S_2) foliation (rather than relic bedding) is in accord with this deformation history. This is also supported by the preferred orientation of micaceous minerals, exhibiting sweeping extinction (Figure 3.2a, 3.2d) and the observations of Caddick (2005), who reported a well-developed cleavage proximal to the Apka Granite in non-garnet bearing units at the base of the Haimanta Group (Figure 3.7).

The formation of a crenulation cleavage in the TSS has also been noted to the NW of our study area, in the Pin Valley, Spiti, by Wiesmayr and Grasemann (2002) who report a foliation cut by a later, shallow NE dipping asymmetric spaced crenulation cleavage mainly formed by domains of enhanced pressure solution. Godin (2003) also presented evidence for crenulation cleavage development in TSS rocks of the Kali Gandaki Valley (Nepal) located to the east of our study area. Godin (2003) attributed crenulation cleavage development to deformation associated

with large scale northeast-verging, tight, megascopic folds which on the microstructural scale produced an axial planar, penetrative schistosity defined by the preferred orientation of biotite, muscovite, and elongate quartz grains in pelitic layers or by a spaced cleavage in more competent layers.

The garnets analyzed from the Haimanta Group metasedimentary rocks for this study contain weak chemical zonation, with a slight Mn-enrichment at garnet rims (Figure 3.8: 1d-3d), that we attribute to resorption during exhumation in the late stages of prograde metamorphism. The apparent Fe-enrichment (Figure 3.8: 3b) and low Ca concentration (Figure 3.8:3a) in the center of garnet 3 is associated with an ilmenite inclusion (Figure 3.9). With the exception of this inclusion, chemical zonation patterns are similar for each of the three analyzed garnets, further supporting our suggestion that all garnet crystals effectively grew simultaneously from a similar bulk rock reservoir.

Thöni et al. (2012) have reported Sm-Nd evidence for pre-Himalayan garnet growth in a leucocratic layer from a biotite schist within the GHS, collected 1.5 km above the MCT, to the NW of Malana. They attribute the unexpectedly old garnet-whole rock "age" of 160 ± 6 Ma to Nd isotopic memory, caused by incomplete isotopic resetting as a result of mixing between young, Himalayan garnet with pre-Himalayan relic garnet (core) domains. Similar results have previously been reported by Argles et al. (1999) from another GHS leucogneiss. Evidence in support of Nd isotopic memory being responsible for the unexpectedly old garnet-whole rock "age" published by Thöni et al. (2012) is presented in the inhomogeneous distribution of Ca zoning within the sampled garnet, characterized by low Ca in the somewhat irregular core parts.

Our garnet samples from the Haimanta Group also display patchy Ca zoning (Figure 3.8: 1a-3a), but we attribute this to disequilibrium in Ca diffusion during prograde metamorphism (Chernoff and Carlson, 1997; Spear and Daniel, 2001; Hirsch and Carlson, 2006; Pattison and Tinkham, 2009). The interpretation of calcium zonation that does not appear to be in equilibrium with other major oxide zonation patterns means the observed patchy Ca zoning cannot be used as evidence for pre-Himalayan garnet (core) growth. This conclusion is supported by the proximity of our samples to those of Chambers et al. (2009) that yield a purely Himalayan age-signature and no geochronological evidence for pre-Himalayan metamorphism.

Furthermore, Thöni et al. (2012) have reported a strongly negative εNd_t value of -18.3 for the aforementioned pre-Himalayan garnet sampled from the GHS, NW of Malana, suggesting the

involvement of fairly old source material that escaped complete Himalayan-age Nd isotopic re-homogenization and potentially indicating the involvement of sources related to Lesser, rather than Greater Himalayan isotopic signatures. Large negative values in εNd_t signatures have also been reported by Ahmad et al. (2000) and Chambers et al. (2008) in discriminating between Lesser and Greater Himalayan isotopic signatures. This supports our claim that although the Ca zoning patterns from our sampled garnets are inhomogeneous, they are not the result of a relict garnet (core) domain produced during a pre-Himalayan metamorphic event.

Thöni et al. (2012) proposed a primary magmatic origin for samples collected from the Leo Pargil leucogranite (located to the east of the Sutlej Valley) and the Wangtu pegmatite (eastern Sutlej Valley), allowing garnet to be used to constrain the magmatic crystallization age at between 6.69 ± 0.81 and 32.6 ± 3.2 Ma, respectively. The Haimanta Group metasediments are intruded by the Apka Granite ~ 480 Ma (Miller et al., 2001). Therefore, if any evidence of pre-Himalayan metamorphism as a result of 500 Ma magmatic activity were preserved in the TSS, the Haimanta Group samples used for this study would be ideal preservation vessels, due to the potential lack of overprinting by leucogranites associated with Himalayan metamorphism. We conclude that the lack of a pre-Himalayan age signature in Haimanta Group samples, and the chemical zoning patterns in garnet porphyroblasts, imply that the Haimantas samples (the focus of our study) did not experience a high-grade, pre-Himalayan metamorphic event as a result of 500 Ma magmatic activity as reported by others for samples in the underlying GHS (Argles et al., 1999; Marquer et al., 2000; Catlos et al., 2002; Thöni et al., 2012).

4. Numerical Modeling of the Metamorphic Differentiation Process

4.1 Techniques I: Basil, Computing Stress and Deformation in a Viscous Material

Basil is a Finite Element code written predominantly in FORTRAN that computes internal stress-distribution, pressure, creep strain-rates and displacement rates for a prescribed set of internal forces, boundary tractions and an arbitrary internal distribution of creep strength (Houseman et al., 2008). The stress values calculated during the following experiment represent the deviatoric stress component of the total stress, and pressure is representative of the mean (isotropic) stress component of the total stress. A fixed confining pressure of 6.0 kbar is also

assigned during the following experiment. The code describes deformation in terms of 2-D, plane strain viscous flow fields. A major assumption of plane strain is that there is no strain in the third dimension, thereby reducing the 3-D strain matrix to a 2-D matrix. This is appropriate for thin section-scale deformation models because a major limitation of thin sections is that they also only define a rock body in two dimensions.

Although some processes in the Elle package permit anisotropy, the viscous deformation fields computed by Basil assume an isotropic constitutive relationship, meaning that the resistance to deformation is independent of the orientation or sign of the deviatoric stress field. This means that the Basil program assumes elastic (recoverable) deformation is present, but only computes viscous (non-recoverable) strain in an incompressible, viscous, non-elastic material undergoing irreversible deformation (Barr and Houseman, 1992; Piazolo et al., 2002; Houseman et al., 2008). We recognize, however, that in reality rocks deform by a combination of elastic and viscous processes. Furthermore, the viscous deformation implemented in Basil assumes that the shearing of a rock is isothermal so that viscous strain energy is dissipated quickly enough to avoid shear-heating and any feedback effects that this might have on rheology (Handy, 1994). This assumption is also essential to the coupling of the reaction-diffusion-deformation equations presented by (Hobbs et al., 2011) and key to the metamorphic differentiation theory presented above.

The total stress ($\sigma_{\alpha\beta}$) is defined in terms of the deviatoric stress ($T_{\alpha\beta}$), and pressure (p) or the mean (isotropic) stress, according to the following equation: $\sigma_{\alpha\beta} = p^*\delta_{\alpha\beta} + T_{\alpha\beta}$, wherein $\delta_{\alpha\beta} = 1$, if $\alpha = \beta$; or else = 0. The Basil code also assumes a constitutive law that relates the deviatoric stress ($T_{\alpha\beta}$) to the strain-rate ($\dot{E}_{ab}$), where the dot above the strain symbol indicates the time derivative and (η) denotes viscosity: $T_{\alpha\beta} = 2\eta^*\dot{E}_{ab}$ (Houseman et al., 2008).

The Basil program has been used to model deformation on all scales, from the evolution of convergent orogenic belts to the evolution of grain scale microstructures (Bons et al., 1997; Houseman et al., 2000; Piazolo, 2001; Piazolo et al., 2002) and the key to this versatility is that the program works with dimensionless variables (Table 3.1), leaving the scale of the problem as an arbitrary value. This versatility is also a key factor in our assumption that deformation histories preserved at the grain-scale in microstructures may provide useful information on mountain-scale deformation events.

The length of a Basil internal time step (IDT0, Table 3.1) determines the amount of simulation time for a finite strain of 1.0 to be reached. This was set to 20, giving the strain increment ($\Delta\gamma$, Table 3.1) a value of 0.05, and meaning that a finite strain of 1.0 was reached every 20 time steps. We chose to use a strain rate of ($\dot{e} = 1 \times 10^{-13}\ s^{-1}$, Table 3.1), in accordance with 'average' geologic strain rates (Pfiffner and Ramsay, 1982), and used the equation ($\dot{e} = e/t$) to calculate the time (t) in years undergone during simulated deformation.

The Basil code simulates simple shear boundary conditions by approximating simple shear deformation applied at an infinite distance from the rigid clast (Bons et al., 1997). Applied tangential velocities were (± 0.5) and normal velocities (0) in accordance with original experiments by Piazolo et al. (2002). The zero magnitude of the applied normal velocities (stresses) implies that only simple shear deformation (Figure 3.10, top) was applied to the microstructure, with no pure shear (compressional) component of deformation (Figure 3.10, bottom). This is a limitation of our model because deformation occurs in nature by a combination of simple shear and pure shear. Due to this, the calculated stress values in this experiment are presented only in terms of the deviatoric (shear) stress component (2^{nd} term, Figure 3.11) of the total stress. The normal stress values in this experiment are not exactly zero values due to the assigned viscosity heterogeneity, but relative to the deviatoric stress values they are much smaller in magnitude.

For plane strain deformation, components of pure shear and simple shear can be quantified in terms of the kinematic vorticity number, Wk (Means et al., 1980). In this experiment, Wk would have a value of 1.0 because only simple shear deformation is applied. However, in natural systems, flow is often instead characterized by non-steady state deformation using the mean kinematic vorticity number (Wm) in which the vorticity of flow is integrated over space and time (Passchier and Urai, 1988). Law et al. (2013) reports vorticity data for Sutlej transects that indicate Wm values in the 0.90-0.95 range, signifying a sub-simple shear with an approximately 28-20% pure shear component (Law et al., 2004), providing an error estimate for our simulation that assumes a 0% pure shear component.

4.2 Techniques II: Implementation into Elle

The program Elle (Jessell et al., 2001; Bons et al., 2008) can be used to model the 2-D evolution of a microstructure by utilizing separate growth algorithms that have the ability to all act on a single 'data structure'. The data structure can be thought of as a thin section view that divides a 2-D microstructure into a system of interconnected nodes that constitute polygons (grains) and can contain information on the structure and attributes of the 2-D array, or on specific properties of the nodes and polygons (Bons et al., 2008). A central program then controls the evolution of extrinsic variables such as temperature, and defines the history of metamorphic processes by passing the data structure to distinct processing algorithms (Bons et al., 2008). These individual algorithms can interact with the data structure by: 1) using it to determine the local values of driving forces, 2) repositioning, creating and removing nodes, 3) reconnecting boundary segments and 4) altering attributes (Jessell et al., 2001; Piazolo et al., 2002). Each process algorithm is written to be independent of any particular driving force, allowing several independent driving forces to be used to describe a process (Jessell et al., 2001).

The Elle program uses the Basil code to calculate the stress field and instantaneous deformation rates, and then updates the spatial coordinates of the mesh defining the grain boundary structure using the following elle executable files: elle2poly.exe→ basil.exe→ basil2elle.exe→ reposition.exe. Elle2poly.exe first transforms the microstructure into a format that the Basil Finite Element code can understand; then basil.exe is run and after basil2elle.exe is implemented to transform the Finite Element output back into an Elle-compatible format. Last, reposition.exe transforms the deformed microstructure file so that all nodes lie within the original bounding box; possible because all Elle models have cyclic boundaries (Bons et al., 2008).

Our experiment is based on models described by (Piazolo et al., 2002), who looked at microstructural features resulting from deformation-induced dynamic recrystallization through studying the effects of the following processes on microstructural evolution: viscous deformation, lattice rotation, subgrain formation, rotational recrystallization, nucleation of new grains from strongly strained grains, and recovery. Their models did not take into account the effects of grain boundary sliding, which may play a significant role in the development of steady-state microstructures. Piazolo et al. (2002) determined that the two dominant microstructural processes in deformation-induced dynamic recrystallization were subgrain

rotation and grain boundary migration. Law et al. (2013) have inferred the same two recrystallization mechanisms for quartz in samples from the Sutlej Valley. Although our experiment involves a heterogeneous mineral assemblage, we propose the driving forces (recrystallization mechanisms) for grain scale processes should be similar for the Haimanta Group metasediments due to their proximity to the samples studied by Law et al. (2013).

The base model files for our experiment can be found in Experiment 16a in the Elle Microdynamics Simulation book (Bons et al., 2008) and are described in the first experiment of Group A by Piazolo et al. (2002), consisting of an initially fine-grained microstructure. In other experiments, Piazolo et al. (2002) assigned larger values of grain boundary mobility (M_{gb}), and modeling results showed an increase in the grain size of recrystallized grains and a decrease in aspect ratios upon induced deformation. We observed little evidence of grain size increase (e.g. bulging grain boundaries) in quartz grains in the studied microstructure (Figure 3.1 and 3.2), and therefore chose to model our experiment after Group A of Piazolo et al. (2002), wherein microstructures were assigned a low grain boundary mobility value (M_{gb}) of (1×10^{-12} $m^2s^{-1}J^{-1}$; Table 3.1). Furthermore, Piazolo et al. (2002) reported that simulated dislocation density values decreased, and the distribution of dislocations became more homogeneous, when larger values of grain boundary mobility were assigned. Because our goal was to determine which parts of the microstructure were most affected by deformation due to heterogeneous mineral distributions, Group A was the most applicable model base.

Viscosity can be defined as the resistance to progressive deformation by shear stress or tensile stress (Van der Pluijm and Marshak, 2004). We chose to assign quartz grains a viscosity of (3.15×10^{18} Pa-s, Table 3.1) to be in accordance with viscosities typical for greenschist to amphibolite facies conditions used in the original experiment by Piazolo et al. (2002). However, our experiments differ in that we assigned a viscosity of (3.15×10^{17} Pa-s, Table 3.1) to grains serving as proxies for phyllosilicates, in order to produce the contrasting mica-rich (less resistant), quartz-rich (more resistant), and heterogeneous (both) layers in the simulated microstructure (Figure 3.12). The elle_viscosity.exe process algorithm recalculates viscosity upon deformation using the base viscosity (η_0), dislocation density (ρ), and a mineral specific parameter (v), using the following equation: $\eta = (\eta_0 + v\rho^{1/2})$. In our deformation simulations we chose *not* to implement the elle_viscosity.exe process algorithm, although it was used in the original experiments by Piazolo et al. (2002). This was done to circumvent the effects of the

elle_viscosity.exe algorithm that assumes a monomineralic aggregate of quartz grains. If implemented, over time all viscosity values would have tended to the same value, and by ignoring this algorithm and thereby forcing the assigned viscosity values to remain constant through time, we are instead focusing on the effect the assigned *differences* in viscosity (i.e. the contrasting properties of multiple mineral phases) would have had on microstructural development. By holding viscosity constant we do, however, ignore the effective viscosity (η_e) that develops with increasing stress and strain rate according to the equation: $\eta_e = \sigma/\dot{e}$ (Bons et al., 2008).

The elle_split.exe process algorithm allows grains to 'split' into subgrains. We used the initially fine-grained starting microstructure (Piazolo et al., 2002); due to the limitations of the original model, the "allowed" subgrain size in this simulation was (3.12×10^{-4} to 1.25×10^{-3} mm^2). The elle_angle_rx.exe process algorithm allows a subgrain to undergo recrystallization by rotation if all of its subgrain/low angle boundaries develop into grain/high angle boundaries and the "allowed" recrystallized (rotational) grain size during the experiment was ($0.8\text{-}1 \times 10^{-2}$ mm^2). Piazolo et al. (2002) report that in the initially fine-grained microstructure that was assigned a low value of M_{gb} (Group A), the mean grain size during simulated deformation remained constant because the "allowed" subgrain size and the recrystallized (rotational) grain size were too similar to the original grain size and therefore no grain size reduction could occur during recrystallization by nucleation and/or rotation.

Furthermore, when the elle_split.exe process algorithm was allowed to interact with the modeled microstructure in our experimental runs, the simulation failed almost immediately and we therefore decided to not include the elle_split.exe process algorithm in the experiment results presented below. According to Piazolo et al. (2002), the rate of subgrain formation has a direct effect on the rate of rotation recrystallization, as rotational recrystallization can only occur if subgrains are present. This means that the elle_angle_rx.exe process algorithm, responsible for rotational recrystallization, although turned on in our experiment, should not have affected the microstructural evolution. The elle_disloc_rx.exe process algorithm allows nucleation by recrystallization to occur if dislocation density values reach a threshold value, but the driving force for this process is the strain energy of the grain or subgrain, calculated in the elle_split.exe process algorithm. Because this algorithm was excluded from our experiment, the

elle_disloc_rx.exe algorithm should also not affect the development of the simulated microstructure, although it was turned on during the experiment.

Law et al. (2013) report microstructures present in a quartz-rich paragneisses collected from the Sutlej Valley transect nearest our study area (ES, Figure 3.6a) that are indicative of high-temperature, grain boundary migration recrystallization. Of the two dominant microstructural processes in deformation-induced dynamic recrystallization (subgrain rotation and grain boundary migration) used by Piazolo et al. (2002), this observation supports our decision to focus on the effects of grain boundary migration as the dominant microstructural process during numerically simulated deformation which serves as a proxy for evolution of the Haimanta Group metasedimentary rocks.

The elle_tbh.exe process algorithm calculates lattice rotation and dislocation density values using the stress field generated by the Basil code to model the development of a crystallographic preferred orientation (CPO) that develops as a result of deformation (Bons et al., 2008). The calculation of the crystal lattice rotation and the work done to accomplish these microstructural processes was calculated using the Taylor-Bishop-Hill method (Taylor, 1938; Bishop and Hill, 1951a, b; Lister and Patterson, 1979; Piazolo et al., 2002; Bons et al., 2008). This algorithm calculates the work done to rotate grains and uses these data to determine new dislocation density values. The assumption of plane strain deformation means that no lattice reorientation due to rigid body rotation was taken into account during the simulated deformation. The Critical Resolved Shear Stress (CRSS) file in the original experiment contained values for different quartz slip systems (assuming all grains were quartz deformed under greenschist to lower amphibolite facies conditions). These CRSS values were used to determine the work done to accomplish crystal lattice rotation (Piazolo et al., 2002). We used the original input file for our experiment, but must acknowledge that these values are unlikely to be representative of CRSS for phyllosilicates present in the simulated microstructure.

Dislocation density represents the amount of defects present in a mineral grain and can be thought of as the small offsets that occur at the edges of crystals, used as nucleation sites during mineral growth (Van der Pluijm and Marshak, 2004). The accumulated dislocations were calculated using the work term from the elle_tbh.exe process algorithm according to the following equation: ($\rho_{new} = 0.4 \times \rho_{initial} + 0.7 \times W$), where ($\rho_{initial}$) is the initial dislocation density of a grain, (ρ_{new}) is the new dislocation density value after induced deformation, and (W) is the

work required for deformation of the grain according to the Taylor-Bishop-Hill code. The units of dislocation density (ρ, Table 3.1) are derived from the total length of dislocations per unit volume (ρ = length/volume; $\rho = m/m^3 = m^{-2}$). Because a low M_{gb} value was assigned, differences in dislocation density of adjacent grains should arise because the migration of grain boundaries into high dislocation density regions is limited. One caveat to this method is that at the rim of a grain, stress perturbations occur due to different crystallographic orientations and viscosities of adjacent grains, resulting in differences in the work necessary to deform a grain as simulated by the Taylor-Bishop-Hill code and preferred recrystallization (higher dislocation density values) at the rims of large grains. To address this issue, we randomly assigned viscosity values (Figure 3.12) to ensure no preliminary relationship existed between grain size and viscosity in the experiment (i.e. large grains were not automatically assigned a viscosity value associated with quartz or phyllosilicates).

Surface free energy of a crystal face is a measure of the change in free energy involved with creating a new surface area as crystals re-arrange their faces to minimize surface free energy (Winter, 2010). The elle_gbm.exe process algorithm utilizes the reduction in surface energy as the driving force for grain boundary migration. In this algorithm, surface energy is a function of the c-axis misorientation angle between two adjacent grains, and migration occurs due to the difference in stored internal strain energy and in chemical potential due to the curvature between adjacent grains (Bons et al., 2008). The algorithm incorporates the effect of growth anisotropy, taking into account different growth rates of crystal surfaces because some lattice orientations are more favorable for growth, leading to competition between adjacent grains (Bons, 2001) and a distinct CPO to developing in the 'winner' grains.

The elle_recovery.exe process algorithm removes thermodynamically unfavorable lattice defects by reducing the dislocation density of each grain or subgrain per time step using the following equation: ($\rho_{new} = \rho_{initial} R_{recover}$), where ($R_{recover}$, Table 3.1) is a temperature dependent recovery factor. We assigned a value of 0.94 to be in accordance with the original model by Piazolo et al. (2002) and acknowledge that due to the temperature difference between our experiment (550 °C) and the original experiment (450 °C), the recovery factor value is likely to be slightly inappropriate in our calculations. We stress again though that we are most interested in constraining how contrasting phase properties control microstructural evolution, rather than absolute properties of any one phase. The elle_check_angle.exe process algorithm was

implemented last during the experiment and is used to check for small angle vertices that are thermodynamically unfavorable and remove them from the microstructure file.

4.3 Model Inputs

We chose to assign a temperature of 550 °C and a confining pressure of 6.0 kbar to represent the early stages of proposed garnet growth in the Haimanta Group metasedimentary rocks that reached 610-620 °C at 7-8 kbars (Chambers et al., 2009). The upper half of the initial modeled microstructure is representative of the suggested protolith for the Haimanta Group metasedimentary rocks, being slightly segregated into thin-section scale quartz-rich and mica-rich layers (Figure 3.12). The bottom half of the microstructure, composed of a heterogeneously distributed assemblage of quartz and phyllosilicate 'grains', represents the control for the experiment where we did not expect the metamorphic differentiation process to ensue upon simulated deformation. All grain parameters except viscosity (discussed above), pressure, and temperature were kept the same as those in the original input file for Experiment 16a in the Elle Microdynamics Simulation book (Bons et al., 2008) to be in accordance with the experiment by Piazolo et al. (2002). This includes keeping the assigned mineral ID of quartz for all grains, instead of changing the value for grains representative of phyllosilicates because the elle_tbh.exe process algorithm is based on the CRSS input file that assumes all grains are quartz. The experiment ran to a lasttime of 197 before failing. To determine the finite strain (e) reached during the experiment, the following equation was used: (Lasttime/IDT0 = e); (197/20 = 9.85). To determine the time (in years) undergone during the experiment, the following equation was used: (t= e/ė); ($t = 9.85/(1x10^{-13}s^{-1})$) $= 9.85x10^{13}s \approx 3{,}127{,}000$ years of deformation.

5. Results

Because the Basil code works with dimensionless variables, to determine the dimensions of the calculated deviatoric stress and dislocation density values, the τ_{scale} and ρ_{scale} values (Table 3.1) were used according to Piazolo et al. (2002). The dimensions of the xy component of the strain rate were based on the strain rate (ė, Table 3.1) assumed during this experiment. This parameter represents the component of strain rate oriented parallel to the x-axis, acting on a

plane perpendicular to the y-axis. We chose to present this component because shear stresses also act parallel to the x-axis and therefore the maximum resulting strain effects on the microstructure should be recorded in this component of the strain rate tensor.

After 400,000 years of deformation, stress "halos" are observed around quartz grains in the uppermost layer, rich in mica grains (Figure 3.13: 2b). The largest strain rate and dislocation density values are also observed in this layer (Figure 3.13: 3b, 4b), while the lowest initial stress, strain rate and dislocation density values are observed in the underlying quartz-rich layer, and a heterogeneous distribution is present in the bottom layer. Interestingly, the strain rate and dislocation density values are larger in the uppermost, mica-rich layer than in the lowermost, heterogeneous layer that also contains abundant mica 'grains', indicating the influence that surrounding different mineral grains may have on deformation.

After 800,000 years of deformation, the large quartz grain in the middle of the mica-rich layer (Figure 3.13: 1c-4c) is surrounded by high values in stress, strain rate and dislocation density. Upon progression to the next image (Figure 3.13: 1d-4d), the values of stress, strain rate and dislocation density outside the grain all decrease as the grain boundary migration process algorithm works to model dissolution of this highly strained grain, visually represented by the grain size decrease between these images. Furthermore, the strain rate and dislocation density values *within* the grain also decrease between these images (Figure 3.13: 3c-d and 4c-d, respectively).

Note that the strain rate and dislocation density values do not continue to increase with time during the simulated deformation. They decrease in response to the grain boundary migration process algorithm, as migration occurs due to the differences in stored internal strain energy and chemical potential due to the curvature between adjacent grains (Bons et al., 2008). Unlike the strain rate parameter, decreasing outside and within the quartz grain (Figure 3.13: 3c-d), the stress value *within* the grain, (Figure 3.13: 3c-d) remains constant and stress effects are only noted outside quartz 'grains' present in the mica-rich layer. We attribute this to being the result of the mean stress on a grain depending upon the strength of the surrounding material (Cosgrove, 1976; Fletcher, 1977; Hobbs et al., 2011), also key to the metamorphic differentiation theory presented above.

The grain boundary migration process algorithm, responsible for the dissolution of the highly strained quartz grains, mirrors the dissolution and re-precipitation of quartz into the fold

hinges of the developing S_2 foliation in our Haimanta Group samples, interpreted to have formed by metamorphic differentiation. This numerical simulation was accomplished by the elle_tbh.exe process algorithm that uses the stress field generated by the Basil code to first calculate the work done to achieve crystal lattice rotation and then uses these values to determine new dislocation density values (Bons et al., 2008). These terms are then used as a driving force for the grain boundary migration process algorithm.

After 1.2 Myr of numerically simulated deformation, the number of quartz 'grains' present in the mica-rich layer is reduced from 9 to 3 (Figure 3.13: 1a, 1d). A similar pattern is observed in the micaceous minerals present in the quartz-rich layer below, although less prevalent due to this layer being initially slightly more enriched in 'mica' grains. The mica grains present in the quartz-rich layer are associated with the lowest values of stress, strain rate and dislocation density due to their presence in the resistant, quartz-rich layer (Figure 3.13: 1b-4b). Much like inclusions preserved within a porphyroblast, the quartz-rich layer appears to buffer the effects of deformation (stress, strain rate, dislocation density) on the less resistant minerals present within them, further highlighting the influence different surrounding mineral grains have on deformation.

Figure 3.13: 1e displays simulated microstructures similar to "mica-fish" around the uppermost quartz grain, a commonly observed shear sense indicator in metamorphic textures. These microstructures are only present in the layer dominated by weak grains and not in the quartz-rich or heterogeneous layers below, once again highlighting the influence different surrounding minerals have on deformation. After 2.0 Myr of deformation (Figure 3.13: 1f-4f), there is only one quartz grain remaining in the uppermost, mica-rich layer. This grain is again surrounded by a high stress "halo", accompanied by large values in strain rate and dislocation density that all decrease in value as the grain continues to dissolve through the end of the simulated deformation (Figure 3.13: 1h-4h).

After 2.8 Myr of deformation, there appears to be little evidence of distinct CPO developed in any of the microstructural layers (Figure 3.13: 1h-4h). A CPO develops in response to shearing because of different crystal lattice orientations and their response to induced stress upon deformation (Bons, 2001). We attribute the lack of a well-developed CPO to be the result of the heterogeneous distribution of different mineral phases (resistance) assigned during the

simulated deformation having a greater effect on microstructural evolution than the assigned crystal lattice orientation values.

6. Discussion

The simulated deformation allows us to model the high stress halos that form around quartz grains in the mica-rich layer and act as the driving force for the dissolution and reprecipitation of quartz into the adjacent quartz-rich layer at later (higher shear strain) stages in the simulation. By extension, we suggest that the stress differences produced in our simple shear experiments may also provide some insight into the processes of crenulation cleavage formation in general. With respect to our Haimanta Group samples, we attribute these stress differences to be evidence for the metamorphic differentiation process associated with formation of S_2 foliation as a result of the dissolution and reprecipitation of quartz into fold hinges during folding of S_1 foliation (Figure 3.4). We propose that the dissolution mechanisms associated with the metamorphic differentiation process aided in the transport of garnet-forming components along crenulation fold limbs to the fold hinges during the formation of the new, axial planar (S_2) foliation, eventually resulting in the formation of garnet porphyroblasts in the quartz-rich layers that define this foliation (Figure 3.1 and 3.2). The interpretation of porphyroblast growth occurring during crenulation of a previously developed foliation that lies at a high angle to the newly developing foliation is not unique to these samples. Similar interpretations have been made in many other orogenic settings (e.g. Aerden et al., 2013; Bell et al., 1995; Bell and Hayward, 1991; Bell et al., 1998; Bell et al., 2013; Hayward, 1991; Sanislav and Bell, 2011; Sayab, 2005; Shah et al., 2011).

Further support for our metamorphic differentiation model is present in the measured strain rate and dislocation density values in the modeled microstructure. Deformation is known to assist nucleation by building up strain energy in the reactant phases, contributing to the energy needed to overcome activation energy barriers, and by providing energetically favourable sites for nucleation (Pattison and Tinkham, 2009). In fine-grained metamorphic rocks, small scale folds often develop due to application of compressional stresses and we suggest that the growth of garnet porphyroblasts in the quartz-rich layers was also aided by the release of strain energy as the “kink” folds were overprinted and a new, axial planar (S_2) foliation developed in the fold

hinges as a result of metamorphic differentiation (Figure 3.4). The large values of strain energy and dislocation densities interpreted to be present in the fold hinges of the crenulated S_1 foliation, aiding the crystallization process, are indicated by the largest values of the xy component of strain rate and dislocation density values present in the mica-rich layer in the simulated microstructure (Figure 3.13: 3a-h and 4a-h, respectively). Note again that this experiment was limited to simple shear deformation and therefore we could not simulate the actual formation of crenulations, or "kink" folds and instead use the mica-rich layer in the simulated microstructure as being representative of the metamorphic mineral assemblage defining the crenulations in the Haimanta Group samples.

The heterogeneous strain rate and dislocation density values across the simulated microstructure, interpreted to relate to the magnitude of strain energy built up during deformation, should mean that different driving forces for nucleation (growth potential) were also present during microstructural evolution in the Haimanta Group samples. Physical and chemical heterogeneities are not uncommon in metamorphic systems and are known to lead to local equilibrium being set up over small areas in a sample, even across each layer in a layered rock (White et al., 2008). This supports our suggestion that domains with different nucleation potential could have developed during deformation of the Haimanta Group rocks, as indicated by the heterogeneous strain rate and dislocation density values developed across layers in the modeled microstructure with their different mineral phase proxies (resistance). Furthermore, Piazolo et al. (2002) noted in their numerical simulations that an increase in the buildup of internal strain energy resulted in a higher rate of recrystallization by nucleation because an increased number of grains exhibited high dislocation densities, allowing subgrains to nucleate. This is in accordance with our suggestion that as strain builds up in some parts of a microstructure, the free energy of formation needed to nucleate a new grain should be smaller in areas of high strain, leading to more "favorable" domains for growth across any given microstructure (here in the mica-rich layers), representative of crenulation fold hinges.

6.1 Comparison of Model Results to Himalayan Stress Estimates

Law et al. (2013) report flow stresses of between 28-7 MPa in quartz-rich units from the GHS sampled in the western part of the Sutlej Valley (Figure 3.6a) at 70-1150 m above the Main

Central Thrust. These flow stress estimates were based on the grain size of dynamically recrystallized quartz using the piezometer of Stipp and Tullis (2003) with corrections for experimental calibration by Holyoke and Kronenberg (2010). There is an order of magnitude difference between the *differential* stress values published by Law et al. (2013) and the *deviatoric* stress values calculated in our numerical experiments. Due to the more hinterland position of the Haimanta Group samples used in this study than in the Law et al. (2013) samples (Figure 3.6a), structural relationships would suggest that the Haimanta Group samples should have far lower differential stress values and *not* the much higher values calculated during our numerical experiments. We determined the units of the deviatoric stress values presented in the above figures based on the τ_{scale} value (Table 3.1) according to Piazolo et al. (2002). Piazolo et al. (2002) did not present an equation as to how this value was determined, but we assume they used the relationship that allows the stress components to be *non-dimensionalized* using the dimensionless variables in the Basil program (Houseman et al., 2008) according to the equation: (η_0/ T_0). This equation is in agreement with the published t_{scale} and η_0 values (Table 3.1) to determine the stress scaling factor: (3.15 x 10^{18} Pa-s)/(3.15 x 10^{10} s) = 10^8 Pa. Furthermore, the deviatoric stress values (reported as differential stress) published by (Piazolo et al., 2002) are between 150-190 MPa, comparable to the maximum deviatoric stress values calculated during this experiment: ($\leq$ 266 MPa).

In an attempt to determine the reason for the order of magnitude difference between the stress estimates published by Law et al. (2013) and those calculated in our experiment according to Piazolo et al. (2002), we found that the "real world strain rate" ($\dot{e}_{Piazolo}$, Table 3.1) is on the (10^{-12} s^{-1}) order of magnitude. Strain rate is a dimensionless variable in the Basil code (Table 3.1), but is defined as ($1/T_0$). If a time scaling factor in agreement with this strain-rate was substituted into the equation above to solve for the stress scaling factor, making the T_0 value on the order of 10^{12} (in lieu of 10^{10}), the stress scaling factor, (originally 10^8 Pa) would be reduced to (10^6 Pa). Furthermore, the Basil code relates the deviatoric stress ($T_{\alpha\beta}$) to the strain-rate ($\dot{E}_{ab}$), through the following equation: $T_{\alpha\beta} = 2\eta^*\dot{E}_{ab}$ (Houseman et al., 2008). Substituting in the values of $\dot{e}_{Piazolo}$ and η_0 from Piazolo et al. (2002), the resulting deviatoric stress, ($T_{\alpha\beta}$) would be: 2(3.15 x 10^{18} Pa-s)*(1.6 x 10^{-12} s^{-1}) = 1.0 x 10^7 Pa (10 MPa or 100 bars). This stress value is an order of magnitude lower than the stress scaling factor presented in the paper and further calls into question the accuracy of the published stress scaling factor of 10^8 Pa.

Lastly, according to Mohr circle relationships, the maximum shear stress, (σ_s) is defined by the radius of the circle: $\frac{1}{2}(\sigma_1 - \sigma_3)$, meaning the differential stress, (σ_D) should be twice the magnitude of the maximum shear stress - at least within the brittle field of deformation. Flow stresses of 28 to 7 MPa were estimated by Law et al. (2013) for the hanging wall of the MCT exposed in the western part of the Sutlej valley (Figure 3.6a), yielding a range of maximum shear stress values between 14 and 3.5 MPa based on the above Mohr-circle reasoning. Furthermore, differential stress values in the crust are expected to reach maximum values of a few hundred MPa (Van der Pluijm and Marshak, 2004), yielding maximum expected shear stresses during crustal deformation of half of this value, much smaller than our calculated maximum values of 266 MPa. All of these parameters call into question the validity of the magnitude of the calculated deviatoric stress values presented in Figure 3.13 and we instead choose to focus not on the units of the deviatoric stress values, but on the magnitude of the *difference* in deviatoric stress values present across the deforming microstructure due to the heterogeneous distribution of mineral phase (resistance) assigned to the numerical simulations.

This order of magnitude discrepancy between stress values calculated in our experiment and those estimated by Law et al. (2013) using natural samples highlights the common disconnect between natural datasets and numerical models. In our numerical modeling, the most likely 'culprit' responsible for the disconnect between our calculated stress values and those of Law et al. (2013) is the t_{scale} value (Table 3.1) used to determine the τ_{scale} value of 10^8 Pa (Table 3.1) in the original experiments by Piazolo et al. (2002). If we had assigned a lower τ_{scale} value (e.g. 10^7 or 10^6 Pa), the calculated deviatoric stress values would be (0 to 26.6 or 0 to 2.66 MPa, respectively), resulting in much lower and potentially more realistic stress values for numerically simulated deformation. However, the actual magnitude of the stress values (i.e. 0 to 266 MPa or 0 to 2.66 MPa) is not as important of a factor in interpreting our results as is the observation of heterogeneities in stress values that arise in our numerical simulations due to the location of a grain in a surrounding aggregate of different mineral grains (e.g. quartz or micas) thereby driving the metamorphic differentiation process.

7. Conclusions

The deformation simulation presented above indicates that domains having different values of stress, strain rate and dislocation density develop across the evolving microstructure due to the contrasting properties of initially assigned layered starting textures (quartz-rich, mica-rich or heterogeneous mineral distribution). A major limitation of the deformation model is that only shear stresses (simple shear deformation) were imposed on the simulated microstructure. These models do not account for compressional stresses (pure shear deformation) and we acknowledge that deformation in natural systems occurs through a combination of simple shear and pure shear. Another limitation of this model is that it does not take into account the effects of hydrolytic weakening, known to reduce the yield strengths of silicate minerals (Kirby, 1983). The chemical effects of H_2O, including: a) pressure-enhanced diffusivity or solubility of water into silicate grains, b) pressure solution, c) bulk solid and grain boundary diffusion, and d) enhanced dislocation creep, recovery and recrystallization (Carter and Tsenn, 1987) were not taken into account in this model. Furthermore, we were unable to simulate the actual nucleation of garnet, interpreted to have arisen on highly strained mica grains in the fold hinges of crenulations on the release of strain energy during the formation of a new, axial planar foliation during the metamorphic differentiation process.

This project does, however present evidence for grain-scale stress differences and resulting dissolution and re-precipitation of quartz grains, driving metamorphic differentiation in our numerical simulations. These models represent the first instance in which the Elle program has been used to study the effects of deformation in a complex polycrystalline aggregate composed of two mineral phases. Large deviatoric stress values develop around quartz grains present in the mica-rich layer in this simulation, resulting in the dissolution and re-precipitation of quartz into the adjacent quartz-rich layer below at later stages in the deformation. This supports the suggestion that differences in stress between the limb and hinge regions of a crenulated foliation drive the metamorphic differentiation process due to the mean stress on a grain being dependent upon the strength of the surrounding material, in agreement with the theorized driving forces for the process (Cosgrove, 1972, 1976; Williams, 1972; Stephansson, 1973; Vidale, 1974; Fletcher, 1977; Hobbs et al., 2011).

These models also provide evidence for the large values in strain energy we interpret to have built up in the crenulation fold hinges, present in the uppermost mica-rich layer of the modeled microstructure. This supports our claim that, although crenulations do not develop in the modeled microstructure, the large magnitudes of strain rate and dislocation density that develop in the mica-rich layers should relate to mica-rich layers in naturally deformed rocks. These areas are interpreted to be representative of the fold hinges of crenulations that acted as nucleation sites for garnet growth as these fold hinges were overprinted during the S_1-S_2 foliation transition. We propose that the heterogeneities in strain rate and dislocation density that arise across the simulated microstructure as a result of the heterogeneous mineral distributions are large enough to suggest the early break down of mica grains in some parts of the microstructure. This would promote nucleation in specific locations, such as the fold hinges of crenulations, as observed in our Haimanta Group samples.

The free energy of a metamorphic reaction (e.g. garnet growth) can be described by the following equation: $\Delta G = V\Delta P - S\Delta T$ and equilibrium thermodynamics predicts that a reaction will only occur if the free energy change (ΔG) associated with the reaction is negative. We suggest that the domains containing the largest values of strain rate and dislocation density should represent the parts of the microstructure with the largest driving force for garnet nucleation (growth potential) as a result of the release of strain energy during the (S_1-S_2) foliation transition, allowing this energy to be utilized in garnet-forming reactions. If these proposed energy differences were present during deformation of the Haimanta Group metasedimentary rocks, the microstructural areas with largest values of strain energy should also be the areas with the most negative values in the free energy of the garnet-forming reaction, resulting in localized areas across the deforming microstructure with a larger potential for chemical reaction (i.e. porphyroblast growth).

The deformation simulation presented above shows that an originally slightly segregated, relatively low-grade metamorphic rock can be transformed into a texture with well-developed compositional banding solely through the differentiation processes. Our results also show that during this process, sufficient energy heterogeneities can develop and act simultaneously with pressure (stress) gradients that drive the metamorphic differentiation process to explain formation of garnet porphyroblasts in specific parts of the microstructure. If the process of metamorphic differentiation is responsible for formation of garnet porphyroblasts in only the

quartz-rich layers in the Haimanta Group samples, meaning that growth only occurred during formation of the new, axial planar (S_2) foliation along fold hinges of the crenulated (S_1) foliation, then the microstructures most likely record a single, prograde deformation history associated with garnet growth (Figure 3.14).

With respect to the tectonic setting of our Haimantas Group samples, the 34-28 Ma ages obtained by Chambers et al. (2009) from both monazite inclusions in garnet and matrix monazite grains indicate that foliation formation and mineral growth must be of Himalayan age rather than being associated with intrusion of the ~480 Ma Apka Granite. Specifically, garnet formation in the Haimantas must also therefore be of Himalayan age and the associated microstructures preserve evidence of a singular, prograde deformation history resulting in garnet formation (Figure 3.14).

References

Aerden, D. G. A. M., Bell, T. H., Puga, E., Sayab, M., Lozano, J. A., and Diaz de Federico, A., 2013, Multi-stage mountain building vs. relative plate motions in the Betic Cordillera deduced from integrated microstructural and petrological analysis of porphyroblast inclusion trails: Tectonophysics, v. 587, p. 188-206.

Ahmad, T., Harris, N., Bickle, M., Chapman, H., Bunbury, J., and Prince, C., 2000, Isotopic constraints on the structural relationships between the Lesser Himalayan Series and the High Himalayan Crystalline Series, Garhwal Himalaya: Geological Society of America Bulletin, v. 112, no. 3, p. 467-477.

Aikman, A. B., Harrison, T. M., and Lin, D., 2008, Evidence for Early (N44 Ma) Himalayan Crustal Thickening, Tethyan Himalaya, southeastern Tibet: Earth and Planetary Science Letters, v. 274, p. 10.

Aitchison, J. C., Ali, J. R., and Davis, A. M., 2007, When and where did India and Asia collide?: Journal of Geophysical Research-Solid Earth, v. 112, no. B5.

Argles, T. W., Prince, C. I., Foster, G. L., and Vance, D., 1999, New garnets for old? Cautionary tales from young mountain belts: Earth and Planetary Science Letters, v. 172, no. 3-4, p. 301-309.

Barr, T. D., and Houseman, G. A., 1992, Distribution of deformation around a fault in a nonlinear ductile medium: Geophysical Research Letters, v. 19, no. 11, p. 1145-1148.

Bell, T. H., Forde, A., and Wang, J., 1995, A new indicator of movement direction during orogenesis: measurement technique and application to the Alps.: Terra Nova, v. 7, p. 500-508.

Bell, T. H., and Hayward, N., 1991, Episodic metamorphic reactions during orogenesis: the control of deformation partitioning on reaction sites and duration: Journal of Metamorphic Geology, no. 9, p. 619-640.

Bell, T. H., Hickey, K. A., and Upton, G. J. G., 1998, Distinguishing and correlating multiple phases of metamorphism across a multiply deformed region using the axes of spiral, staircase and sigmoidally curved inclusion trails in garnet.: Journal of Metamorphic Geology, v. 16, p. 767-794.

Bell, T. H., Rieuwers, M. T., Cihan, M., Evans, T. P., Ham, A. P., and Welch, P. W., 2013, Inter-relationships between deformation partitioning, metamorphism and tectonism: Tectonophysics, v. 587, p. 119-132.

Bishop, J. F. W., and Hill, R., 1951a, A theoretical derivation of the plastic properties of a polycrystalline face-centered metal: Philosophical Magazine, v. 42, p. 1298-1307.

Bishop, J. F. W., 1951b, A theory of plastic distortion of a polycrystalline aggregated under combined stresses: Philosophical Magazine, v. 42, p. 147-161.

Bons, P. D., 2001, Development of crystal morphology during unitaxial growth in a progressively widening vein: I. The numerical model: Journal of Structural Geology, v. 23, p. 8.

Bons, P. D., Barr, T. D., and ten Brink, C. E., 1997, The development of δ-clasts in non-linear viscous materials: a numerical approach: Tectonophysics, v. 270, p. 13.

Bons, P. D. D., Koehn, D., and Jessell, M. W., 2008, Microdynamics Simulation, Springer.

Brookfield, M. E., 1993, The Himalayan passive margin from Precambrian to Cretaceous times: Sedimentary Geology, v. 84, no. 1-4, p. 1-35.

Caddick, M., 2005, PhD: University of Cambridge.

Carlson, W. D., 2011, Porphyroblast crystallization: linking processes, kinetics, and microstructures: International Geology Review, v. 53, no. 3-4, p. 406-445.

Carlson, W. D., Denison, C., and Ketcham, R. A., 1995, Controls on the nucleation and growth of porphyroblasts: Kinetics from natural textures and numerical models: Geological Journal, v. 30, no. 3-4, p. 207-225.

Carter, N. L., and Tsenn, M. C., 1987, Flow properties of continental lithosphere: Tectonophysics, v. 136, no. 1-2, p. 27-63.

Catlos, E. J., Harrison, T. M., Manning, C. E., Grove, M., Rai, S. M., Hubbard, M. S., and Upreti, B. N., 2002, Records of the evolution of the Himalayan orogen from in situ Th-Pb ion microprobe dating of monazite: Eastern Nepal and western Garhwal: Journal of Asian Earth Sciences, v. 20, no. 5, p. 459-479.

Chambers, J. A., Argles, T. W., Horstwood, M. S. A., Harris, N. B. W., Parrish, R. R., and Ahmad, T., 2008, Tectonic implications of Palaeoproterozoic anatexis and Late Miocene metamorphism in the Lesser Himalayan Sequence, Sutlej Valley, NW India: Journal of the Geological Society, v. 165, p. 725-737.

Chambers, J., Caddick, M., Argles, T., Horstwood, M., Sherlock, S., Harris, N., Parrish, R., and Ahmad, T., 2009, Empirical constraints on extrusion mechanisms from the upper margin of an exhumed high-grade orogenic core, Sutlej valley, NW India: Tectonophysics, v. 477, p. 16.

Chernoff, C. B., and Carlson, W. D., 1997, Disequilibrium for Ca during growth of pelitic garnet: Journal of Metamorphic Geology, v. 15, no. 4, p. 421-438.

Cosgrove, J. W., 1972, The development and interrelationships of microfolds and crenulation cleavage.

Cosgrove, J. W., 1976, The formation of crenulation cleavage: Geological Society of London Journal, v. 132, p. 23.

Dewers, T., and Ortoleva, P., 1990, Geochemical self-organization. III: a mechano-chemical model of metamorphic differentiation: American Journal of Science, v. 290, p. 49.

Ding, L., Kapp, P., and Wan, X. Q., 2005, Paleocene-Eocene record of ophiolite obduction and initial India-Asia collision, south central Tibet: Tectonics, v. 24, no. 3.

Fletcher, R. C., 1977, Quantitative theory for metamorphic differentiation in development of crenulation cleavage: Geology, v. 5, p. 3.

Gaidies, F., Pattison, D. R. M., and de Capitani, C., 2011, Toward a quantitative model of metamorphic nucleation and growth: Contributions to Mineralogy and Petrology, v. 162, no. 5, p. 975-993.

Godin, L., 2003, Structural evolution of the Tethyan sedimentary sequence in the Annapurna area, central Nepal Himalaya: Journal of Asian Earth Sciences, v. 22, p. 19.

Godin, L., Grujic, D., Law, R. D., and Searle, M. P., 2006, Channel Channel flow, ductile extrusion and exhumation in continental collision zones: an introduction, v. 268, p. 23.

Godin, L., Parrish, R. R., Brown, R. L., and Hodges, K. V., 2001, Crustal thickening leading to exhumation of the Himalayan metamorphic core of central Nepal: Insight from U-Pb Geochronology and Ar-40/Ar-39 Thermochronology: Tectonics, v. 20, no. 5, p. 729-747.

Handy, M. R., 1994, Flow laws for rocks containing two non-linear viscous phases: a phenomenological approach: Journal of Structural Geology, v. 16, no. 3, p. 15.

Harris, N., and Massey, J., 1994, Decompression and anatexis of Himalayan metapelites: Tectonics, v. 13, no. 6, p. 10.

Hayward, N., 1991, Orogenic processes, deformation and mineralization history of portions of the Appalachian Orogen, USA, based on microstructural analysisUnpublished PhD thesis]: James Cook University.

Hirsch, D. M., and Carlson, W. D., 2006, Variations in rates of nucleation and growth of biotite porphyroblasts: Journal of Metamorphic Geology, v. 24, no. 8, p. 763-777.

Hobbs, B. E., Ord, A., and Regenauer-Lieb, K., 2011, The thermodynamics of deformed metamorphic rocks: A review: Journal of Structural Geology, v. 33, p. 61.

Holyoke, C. W., III, and Kronenberg, A. K., 2010, Accurate differential stress measurement using the molten salt cell and solid salt assemblies in the Griggs apparatus with applications to strength, piezometers and rheology: Tectonophysics, v. 494, no. 1-2, p. 17-31.

Houseman, G. A., Barr, T., and Evans, L., 2008, 3.8 Basil: stress and deformation in a viscous material, Microdynamics Simulation, Springer, p. 138-154.

Houseman, G. A., Neil, E. A., and Kohler, M. D., 2000, Lithospheric instability beneath the Transverse Ranges of California: Journal of Geophysical Research, v. 105, no. B7, p. 14.

Jessell, M., Bons, P., Evans, L., Barr, T., and Stuwe, K., 2001, Elle: the numerical simulation of metamorphic and deformation microstructures: Computers & Geosciences, v. 27, no. 1, p. 17-30.

Kirby, S. H., 1983, Rheology of the lithosphere: Reviews of Geophysics, v. 21, no. 6, p. 1458-1487.

Law, R. D., Searle, M. P., and Simpson, R. L., 2004, Strain, deformation temperatures and vorticity of flow at the top of the Greater Himalayan Slab, Everest Massif, Tibet: Journal of the Geological Society, v. 161, p. 305-320.

Law, R. D., Stahr, D. W., Francsis, M. K., Ashley, K. T., Grasemann, B., and Ahmad, T., 2013, Deformation temperatures and flow vorticities near the base of the Greater Himalayan Series, Sutlej Valley and Shimla Klippe, NW India: Journal of Structural Geology, v. 54, p. 21-53.

Lister, G. S., and Patterson, M. S., 1979, The simulation of fabric development during plastic deformation and its application to quartzite: fabric transitions: Journal of Structural Geology, v. 1, p. 99-115.

Liu, G., and Einsele, G., 1994, Sedimentary history of the Tethyan Basin in the Tibetan Himalayas: Geologische Rundschau, v. 83, no. 1, p. 32-61.

Marquer, D., Chawla, H. S., and Challandes, N., 2000, Pre-alpine high-grade metamorphism in High Himalaya crystalline sequences: Evidence from Lower palaeozoic Kinnaur Kailas granite and surrounding rocks in the Sutlej Valley (Himachal Pradesch, India): Eclogae Geologicae Helvetiae, v. 93, no. 2, p. 207-220.

Martin, A. J., Gehrels, G. E., and DeCelles, P. G., 2007, The tectonic significance of (U,Th)/Pb ages of monazite inclusions in garnet from the Himalaya of central Nepal: Chemical Geology, v. 244, no. 1-2, p. 1-24.

Means, W. D., Hobbs, B. E., Lister, G. S., and Williams, P. F., 1980, Vorticity and non-coaxiality in progressive deformations: Journal of Structural Geology, v. 2, no. 3, p. 371-378.

Miller, C., Thöni, M., Frank, W., Grasemann, B., Klotzli, U., Guntli, P., and Draganits, E., 2001, The early Palaeozoic magmatic event in the Northwest Himalaya, India: source, tectonic setting and age of emplacement: Geological Magazine, v. 138, no. 3, p. 237-251.

Ortoleva, P., Merino, E., Moore, C., and Chadam, J., 1987, Geochemical self-organization I; reaction-transport feedbacks adn modeling approach: American Journal of Science, v. 287, p. 28.

Passchier, C. W., and Urai, J. L., 1988, Vorticity and strain analysis using Mohr diagrams: Journal of Structural Geology, v. 10, no. 7, p. 755-763.

Pattison, D. R. M., and Tinkham, D. K., 2009, Interplay between equilibrium and kinetics in prograde metamorphism of pelites: an example from the Nelson aureole, British Columbia: Journal of Metamorphic Geology, v. 27, no. 4, p. 249-279.

Pfiffner, O. A., and Ramsay, J. G., 1982, Constraints on geological strain rates - arguments from finite strain states of naturally deformed rocks: Journal of Geophysical Research, v. 87, no. NB1, p. 311-321.

Piazolo, S., 2001, Shape fabric development during progressive deformation. [PhD: Berichte aus der Geowissenschaft.

Piazolo, S., Bons, P. D., Jessell, M. W., Evans, L., and Passchier, C. W., 2002, Dominance of microstructural processes and their effect on microstructural development: insights from numerical modelling of dynamic recrystallization: Geological Society of London, Special Publications, v. 200, p. 22.

Sander, B., 1911, Uber Zusammenhange zwischen Teilbewegung und Gefuge in Gesteinen: Tscher. Miner. Petrog., v. 30, p. 23.

Sanislav, I. V., and Bell, T. H., 2011, The inter-relationships between long-lived metamorphism, pluton emplacement and changes in the direction of bulk shortening during orogenesis: Journal of Metamorphic Geology, v. 29, no. 5, p. 513-536.

Sayab, M., 2005, Microstructural evidence for N-S shortening in the Mount Isa Inlier (NW Queensland, Australia): the preservation of early W-E-trending foliations in porphyroblasts revealed by independent 3D measurement techniques: Journal of Structural Geology, v. 27, no. 8, p. 1445-1468.

Searle, M. P., Simpson, R. L., Law, R. D., Parrish, R. R., and Waters, D. J., 2003, The structural geometry, metamorphic and magmatic evolution of the Everest massif, High Himalaya of Nepal-South Tibet: Journal of the Geological Society, v. 160, p. 345-366.

Shah, S. Z., Sayab, M., Aerden, D., and Khan, M. A., 2011, Foliation intersection axes preserved in garnet porphyroblasts from the Swat area, NW Himalaya: A record of successive crustal shortening directions between the Indian plate and Kohistan-Ladakh Island Arc: Tectonophysics, v. 509, no. 1-2, p. 14-32.

Spear, F. S., and Daniel, C. G., 2001, Diffusion control of garnet growth, Harpswell Neck, Maine, USA: Journal of Metamorphic Geology, v. 19, no. 2, p. 179-195.

Spry, A., 1969, Metamorphic Textures, London, Pergamon Press Ltd., 350 p.:

Stephansson, O., 1973, Stress-induced diffusion during folding: Tectonophysics, v. 22, p. 18.

Stipp, M., and Tullis, J., 2003, The recrystallized grain size piezometer for quartz: Geophysical Research Letters, v. 30, no. 21.

Taylor, G. I., 1938, Plastic strain in metals: Journal of the Institute of Metals, v. 62, p. 307-324.

Thakur, S. S., and Tripathi, K., 2008, Regional metamorphism in the Haimanta Group of rocks, Sutlej river valley, NW Himalaya, India: Current Science, v. 95, no. 1, p. 104-109.

Thöni, M., Miller, C., Hager, C., Grasemann, B., and Horschinegg, M., 2012, New geochronological constraints on the thermal and exhumation history of the Lesser and Higher Himalayan Crystalline Units in the Kullu-Kinnaur area of Himachal Pradesh (India): Journal of Asian Earth Sciences, v. 52, p. 98-116.

Van der Pluijm, B. A., and Marshak, S., 2004, Earth Structure, New York, W.W. Norton & Company, Inc.

Vannay, J. C., Grasemann, B., Rahn, M., Frank, W., Carter, A., Baudraz, V., and Cosca, M., 2004, Miocene to Holocene exhumation of metamorphic crustal wedges in the NW Himalaya: Evidence for tectonic extrusion coupled to fluvial erosion: Tectonics, v. 23, no. 1.

Vidale, R., 1974, Metamorphic differentiation layering in pelitic rocks of Dutchess County, New York: Carnegie Institute Washington, v. 634, p. 13.

White, R. W., Powell, R., and Baldwin, J. A., 2008, Calculated phase equilibria involving chemical potentials to investigate the textural evolution of metamorphic rocks: Journal of Metamorphic Geology, v. 26, no. 2, p. 181-198.

Wiesmayr, G., and Grasemann, B., 2002, Eohimalayan fold and thrust belt: Implications for teh geodynamic evolution of the NW-Himalaya (India): Tectonics, v. 21, no. 6, p. 8.

Williams, P. F., 1972, Development of metamorphic layering and cleavage in low-grade metamorphic rocks at Bermagui, Australia: American Journal of Science, v. 272, no. 47, p. 1.

Winter, J. D., 2010, An introduction to igneous and metamorphic petrology, New Jersey, Pearson Education, Inc., 702 p.:

Yin, A., Dubey, C. S., Kelty, T. K., Webb, A. A. G., Harrison, T. M., Chou, C. Y., and Celerier, J., 2010, Geologic correlation of the Himalayan orogen and Indian craton: Part 2. Himalaya Structural geology, geochronology, and tectonic evolution of the Eastern Himalaya: Geological Society of America Bulletin, v. 122, no. 3-4, p. 37.

Yin, A., and Harrison, T. M., 2000, Geologic evolution of the Himalayan-Tibetan orogen: Annual Review of Earth and Planetary Sciences, v. 28, p. 211-280.

Zhu, B., Kidd, W. S. F., Rowley, D. B., Currie, B. S., and Shafique, N., 2005, Age of initiation of the India-Asia collision in the east-central Himalaya: Journal of Geology, v. 113, no. 3, p. 265-285.

Figures

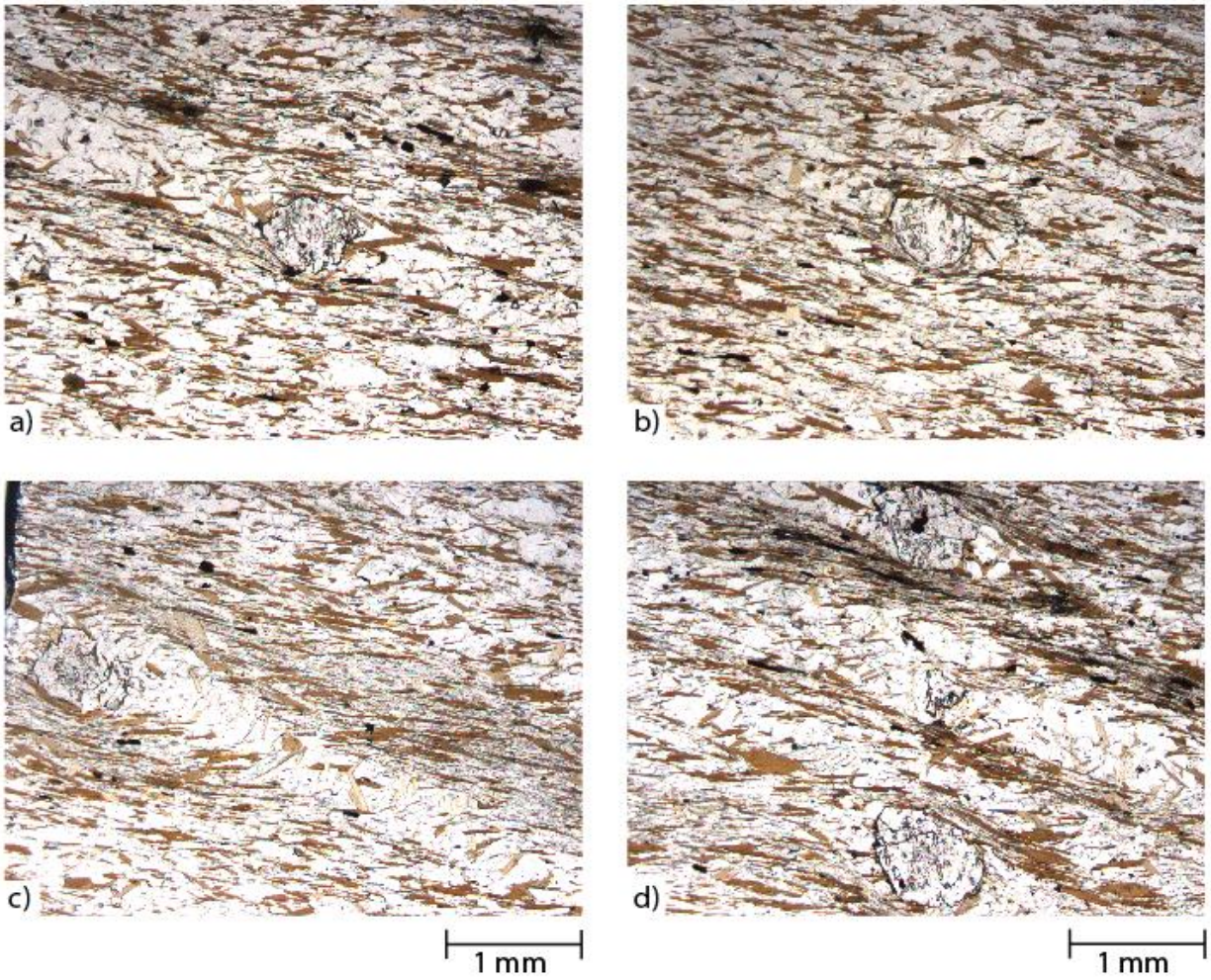

Figure 3.1. Microstructures preserved in the Haimanta Group metasediments in plane polarized light photomicrographs at 2.5x magnification.

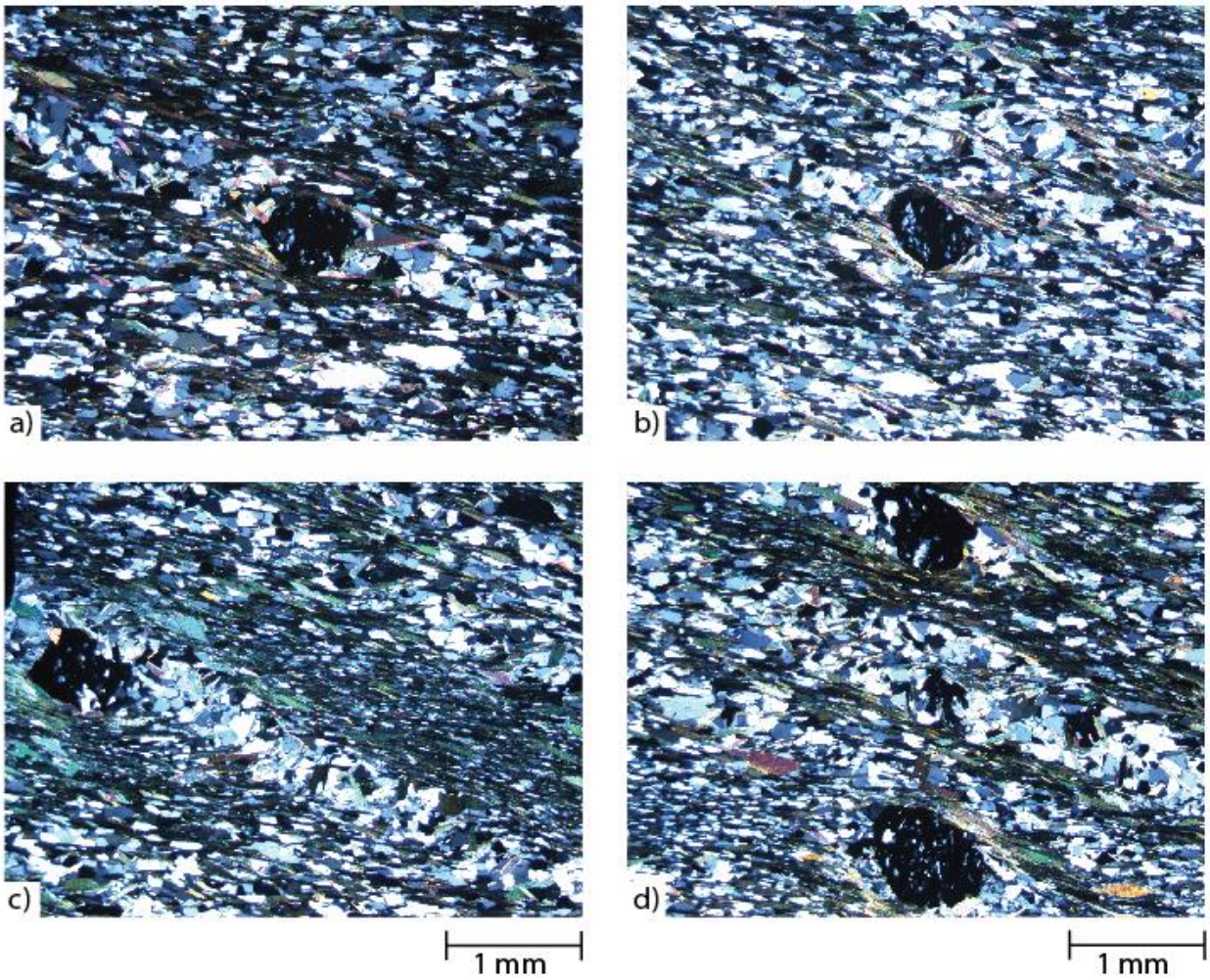

Figure 3.2. Microstructures preserved in the Haimanta Group metasediments in cross polarized light photomicrographs at 2.5x magnification.

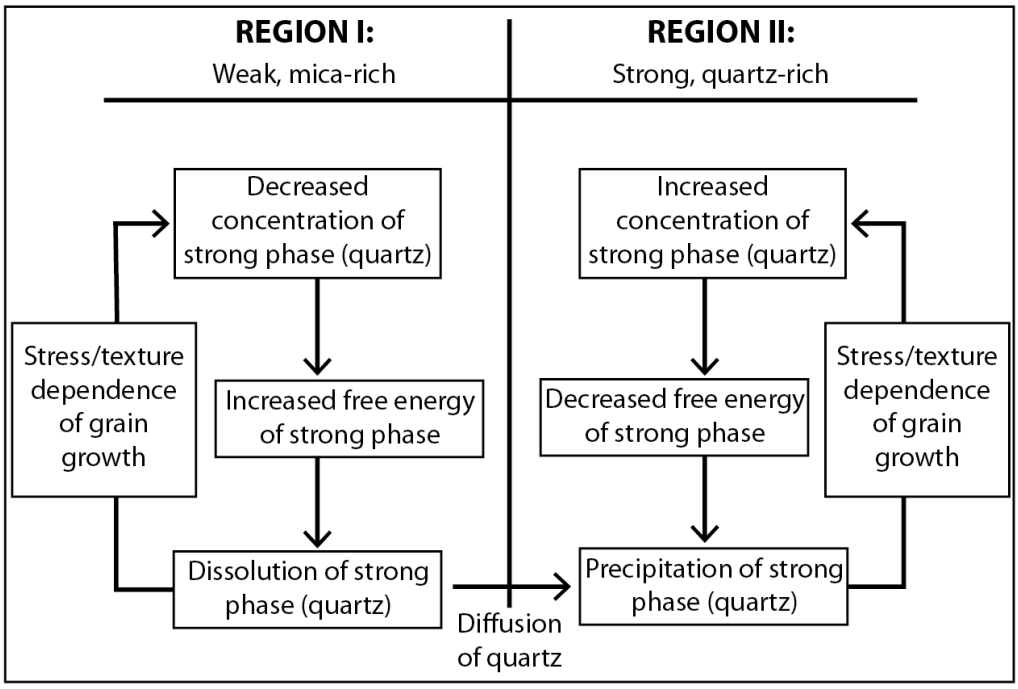

Figure 3.3. Box diagram schematic to depict the positive reinforcement of grain growth (precipitation) or dissolution of the strong phase (quartz) in response to being embedded in a mixture with an initial concentration rich in micaceous minerals or quartz. After Ortoleva et al. (1987) and Hobbs et al. (2011).

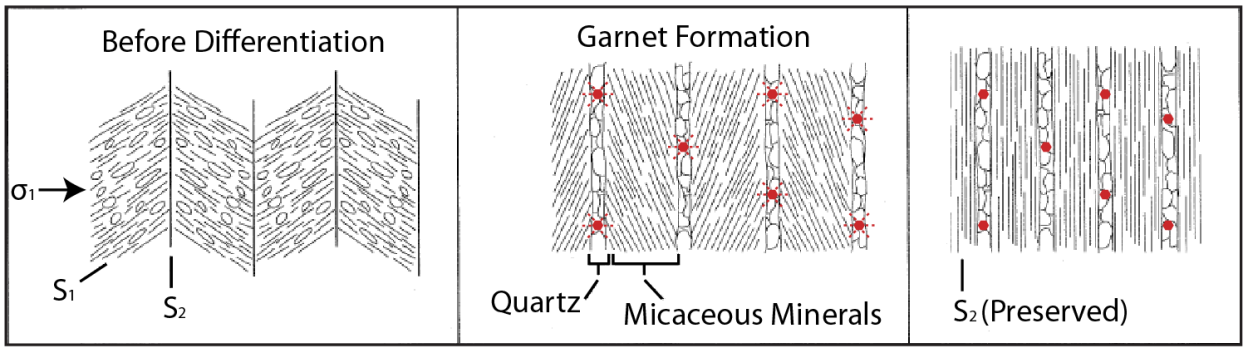

Figure 3.4. Diagram showing the metamorphic differentiation process during which a new, axial planar foliation (S_2) develops as a result of the folding of a pre-existing foliation (S_1). Red polygons represent the hypothesized location of garnet nucleation in the fold hinges of crenulations defined by micaceous minerals that are overprinted during the transition from the S_1 to the S_2 foliation. After Van der Pluijm and Marshak (2004).

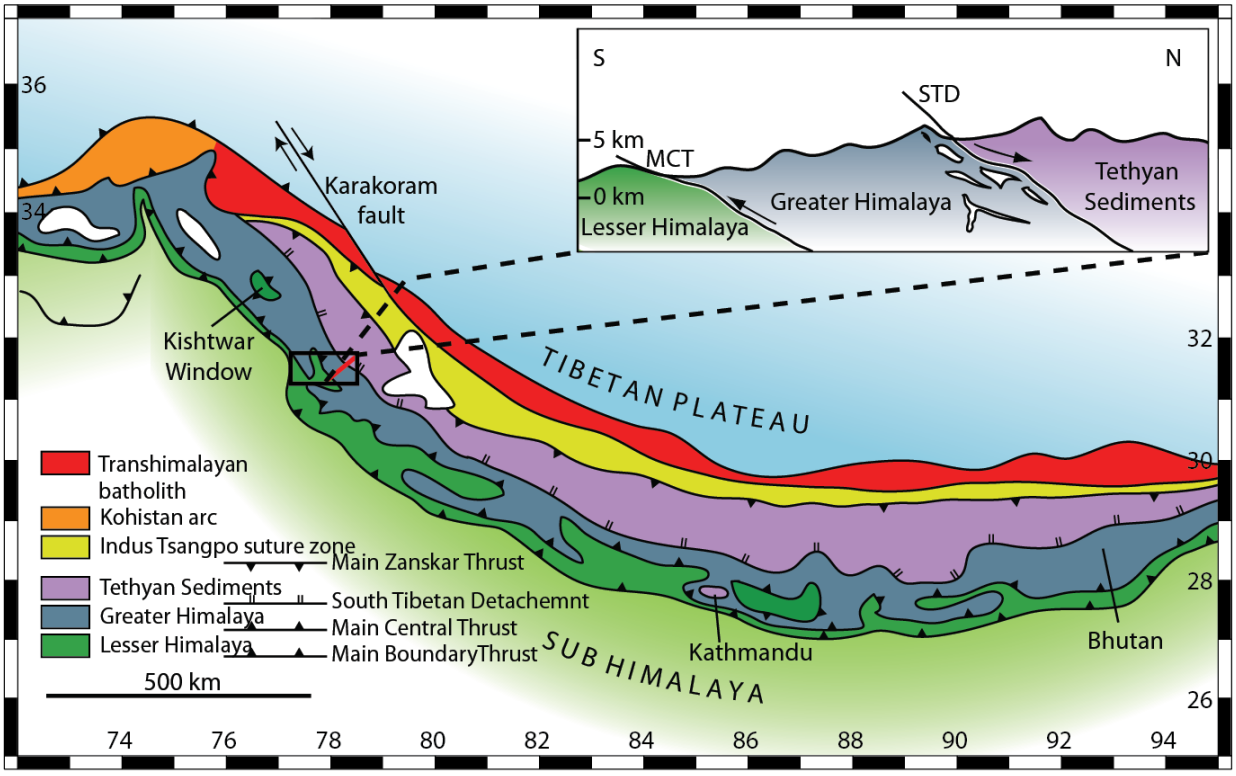

Figure 3.5. Generalized geologic map of the Himalaya. Black box represents the location of the Sutlej Valley in Figure 3.6 and red line represents cross section line depicting the general structural relationships in the Sutlej Valley. After Searle et al. (2003).

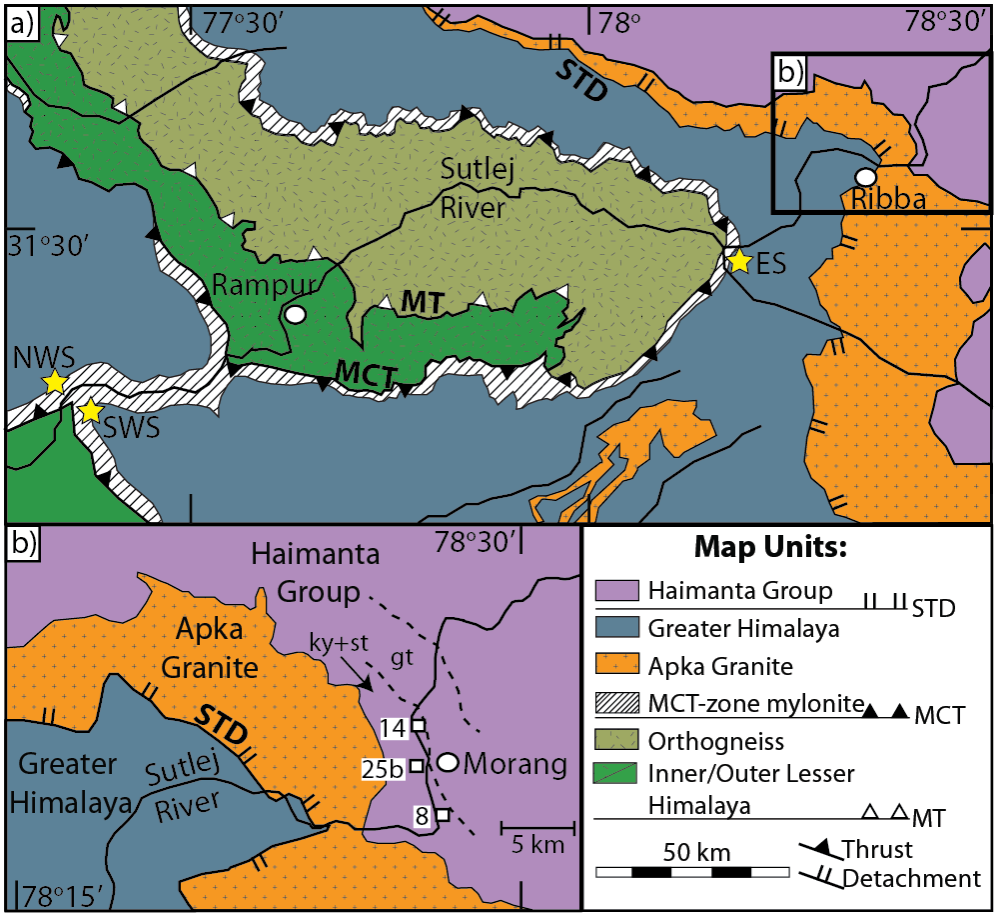

Figure 3.6. (a) Geologic map of the Sutlej Valley (Law et al., 2013; Vannay et al., 2004). STD, South Tibetan Detachment; MCT, Main Central Thrust; MT, Munsiari Thrust; yellow stars highlight the location of the Northwest Sutlej (NWS), Southwest Sutlej (SWS) and Eastern Sutlej (ES) traverses used to calculate deformation temperatures in Law et al. (2013). Black box highlights location of inset (b) Detailed geology of the study area (Chambers et al., 2009). The sample locality for this study (25b) and the samples used for P-T-t path determination (8 and 14) and metamorphic isograds (dashed lines) by Chambers et al. (2009) are labeled. Gt, garnet; st, staurolite; ky, kyanite.

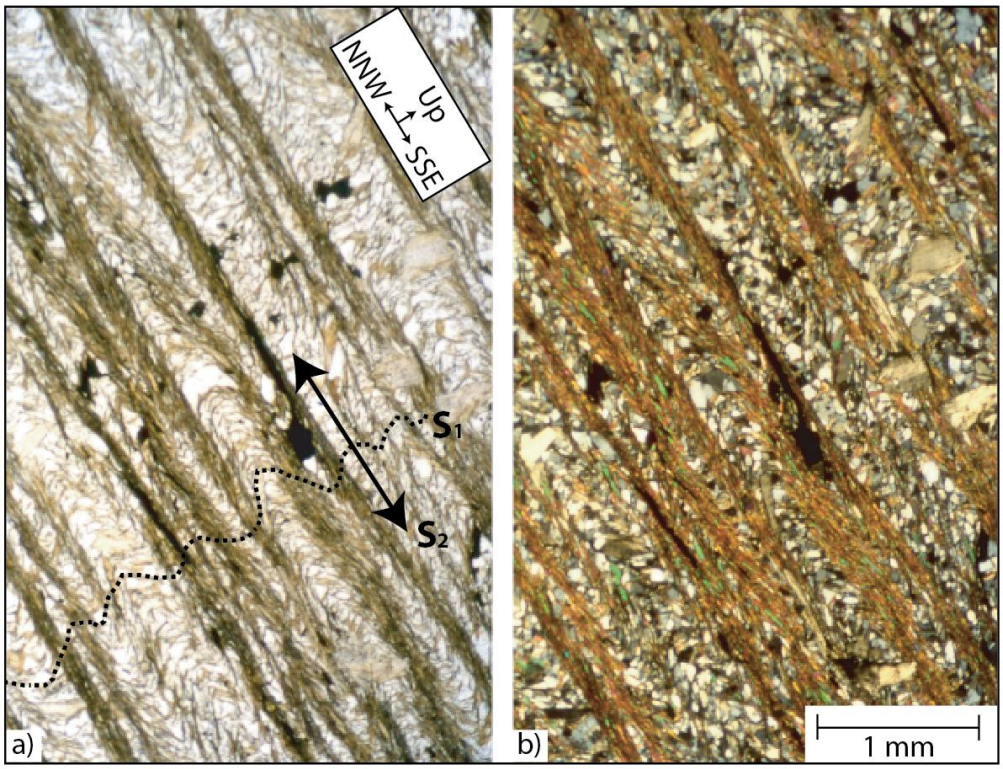

Figure 3.7. Fabrics recorded in the Haimanta Group metasediments, after Caddick (2005). Diagrams (a) and (b) are plane polarized and cross polarized light photomicrographs, respectively. The orientation of the S_2 foliation, defined by the mica-rich and quartz-rich domains, is denoted by arrows and the S_1 foliation (folded) is annotated with a dashed line.

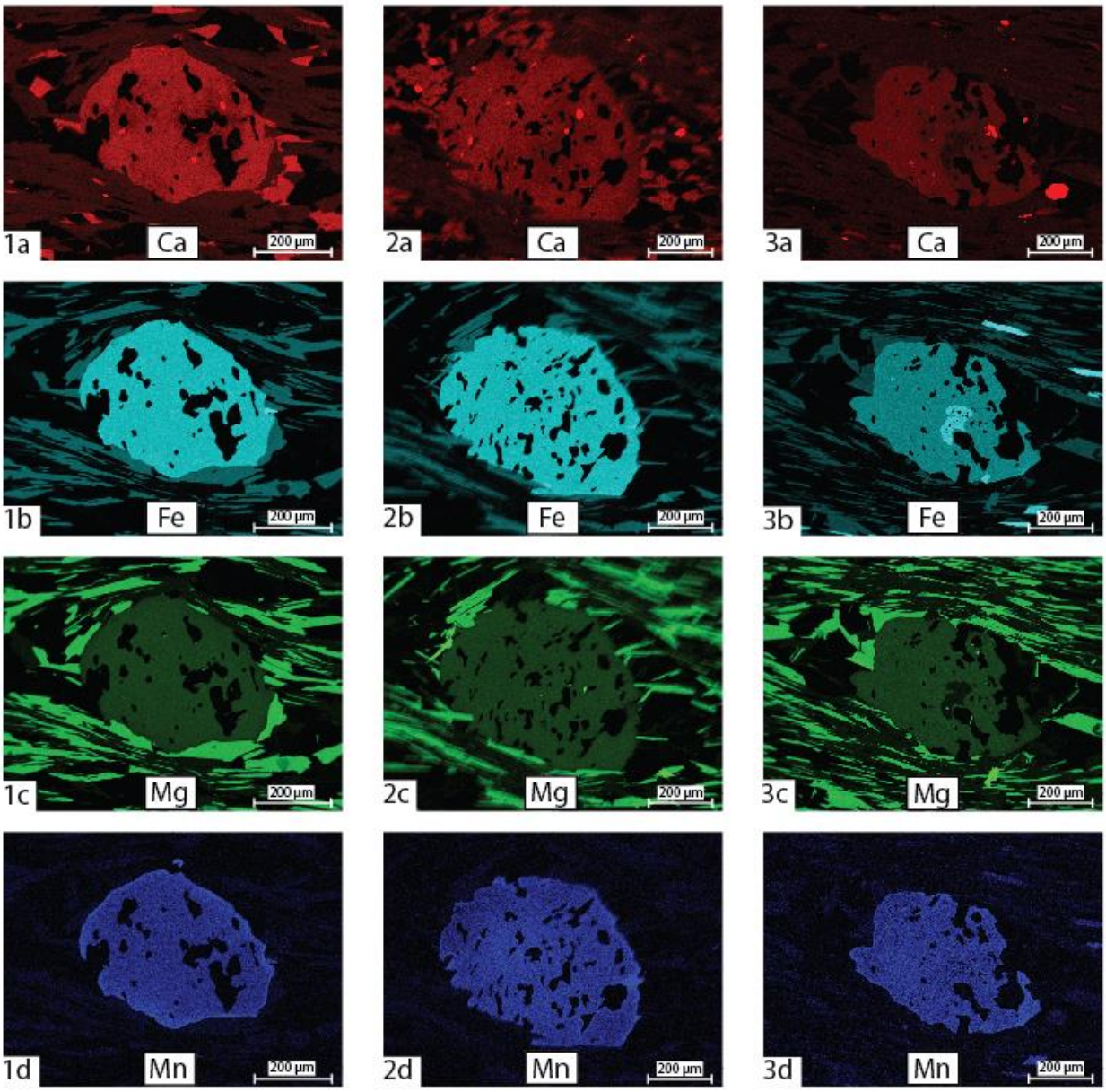

Figure 3.8. Energy Dispersive Spectrometer (EDS) chemical zonation maps from three garnet porphyroblasts sampled from the Haimanta Group. Increasing brightness in color represents increasing concentration of each respective cation, labeled in the bottom center of each figure.

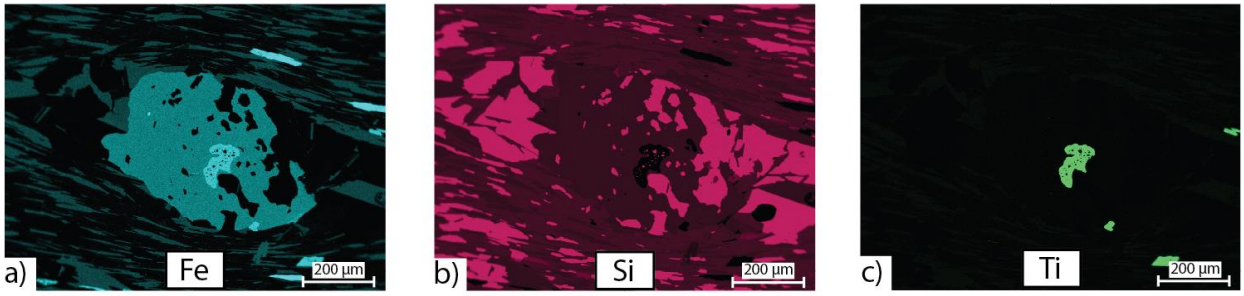

Figure 3.9. Energy Dispersive Spectrometer (EDS) chemical zonation maps for a single garnet (3, Figure 3.8). Increasing brightness in color represents increasing concentration of each respective cation, labeled in the bottom center of each figure.

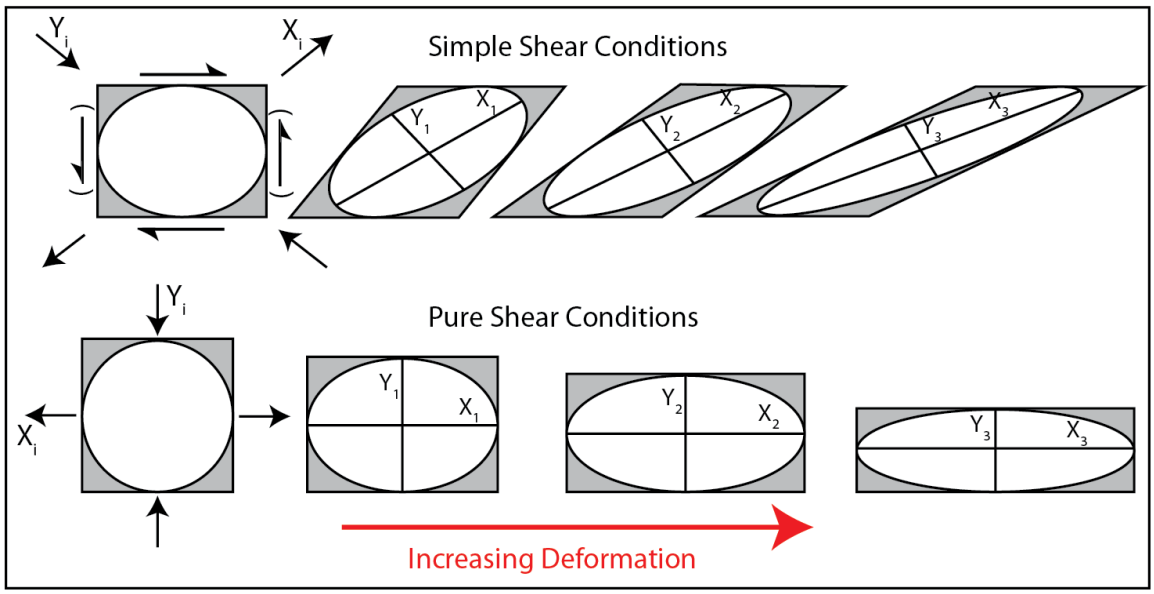

Figure 3.10. Simple shear conditions, non-coaxial strain (top) and pure shear conditions, coaxial strain (bottom). After Van der Pluijm and Marshak (2004).

$$[\sigma_{ab}] = \begin{bmatrix} \sigma_m & 0 \\ 0 & \sigma_m \end{bmatrix} + \begin{bmatrix} \sigma_{11} - \sigma_m & \sigma_{12} \\ \sigma_{21} & \sigma_{22} - \sigma_m \end{bmatrix}$$

$$\sigma_m = (\sigma_{11} + \sigma_{22})/2$$

Figure 3.11. The total stress $[\sigma_{ab}]$ separated into the mean (isotropic) stress component matrix (1st term) and the deviatoric stress component matrix (2nd term). Adapted from the 3-D stress matrix of Van der Pluijm and Marshak (2004) to be in accordance with plane strain, (2-D) deformation conditions.

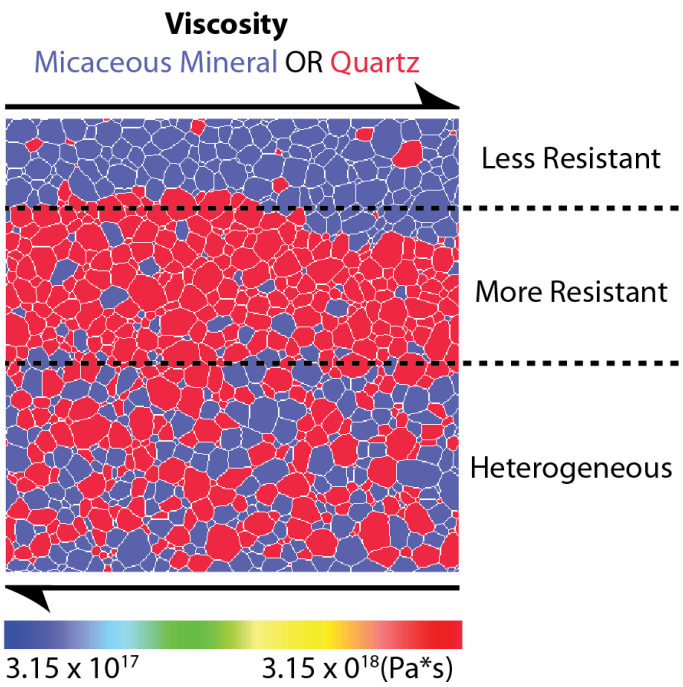

Figure 3.12. Initial microstructural configuration for the experiment. Slightly segregated (mica-rich, less resistant and quartz-rich, more resistant) and heterogeneous mineral phase distribution domains are highlighted by dashed lines. Colorbar represents the viscosity value (mineralogy) assigned to each grain.

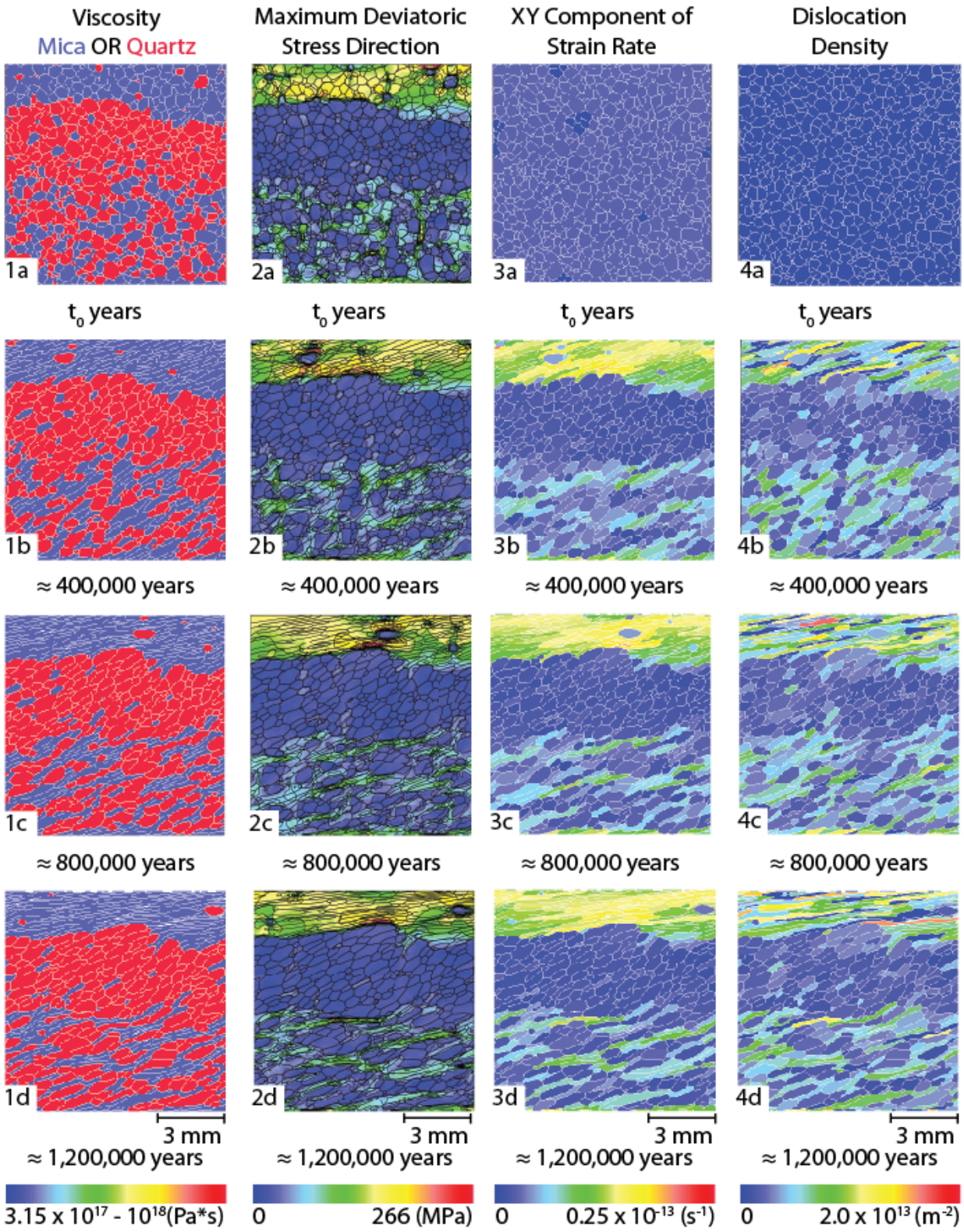
Viscosity
Mica OR Quartz
Maximum Deviatoric Stress Direction
XY Component of Strain Rate
Dislocation Density
1a
2a
3a
4a
t0 years
t0 years
t0 years
t0 years
1b
2b
3b
4b
≈ 400,000 years
≈ 400,000 years
≈ 400,000 years
≈ 400,000 years
1c
2c
3c
4c
≈ 800,000 years
≈ 800,000 years
≈ 800,000 years
≈ 800,000 years
1d
2d
3d
4d
3 mm
3 mm
3 mm
3 mm
≈ 1,200,000 years
≈ 1,200,000 years
≈ 1,200,000 years
≈ 1,200,000 years
3.15 x 10^17 - 10^18(Pa*s)
0
266 (MPa)
0
0.25 x 10^-13 (s^-1)
0
2.0 x 10^13 (m^-2)

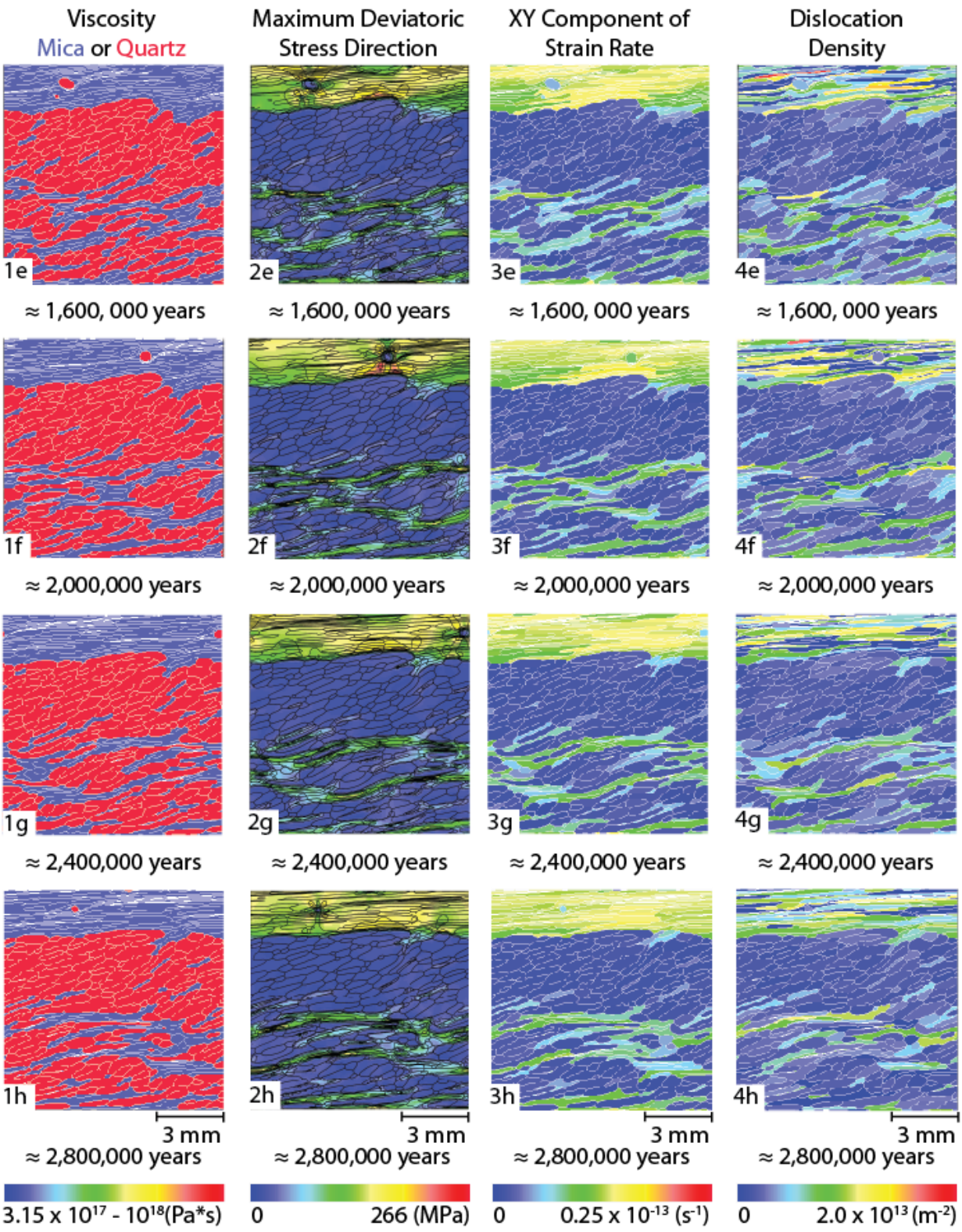

Figure 3.13. Specific microstructural properties after simulated deformation over 2.8 Myr. Labels at the top of each column represent the individual property measured and each sequential image in a column represents an increase of 400,000 years. Model has cyclic boundaries.

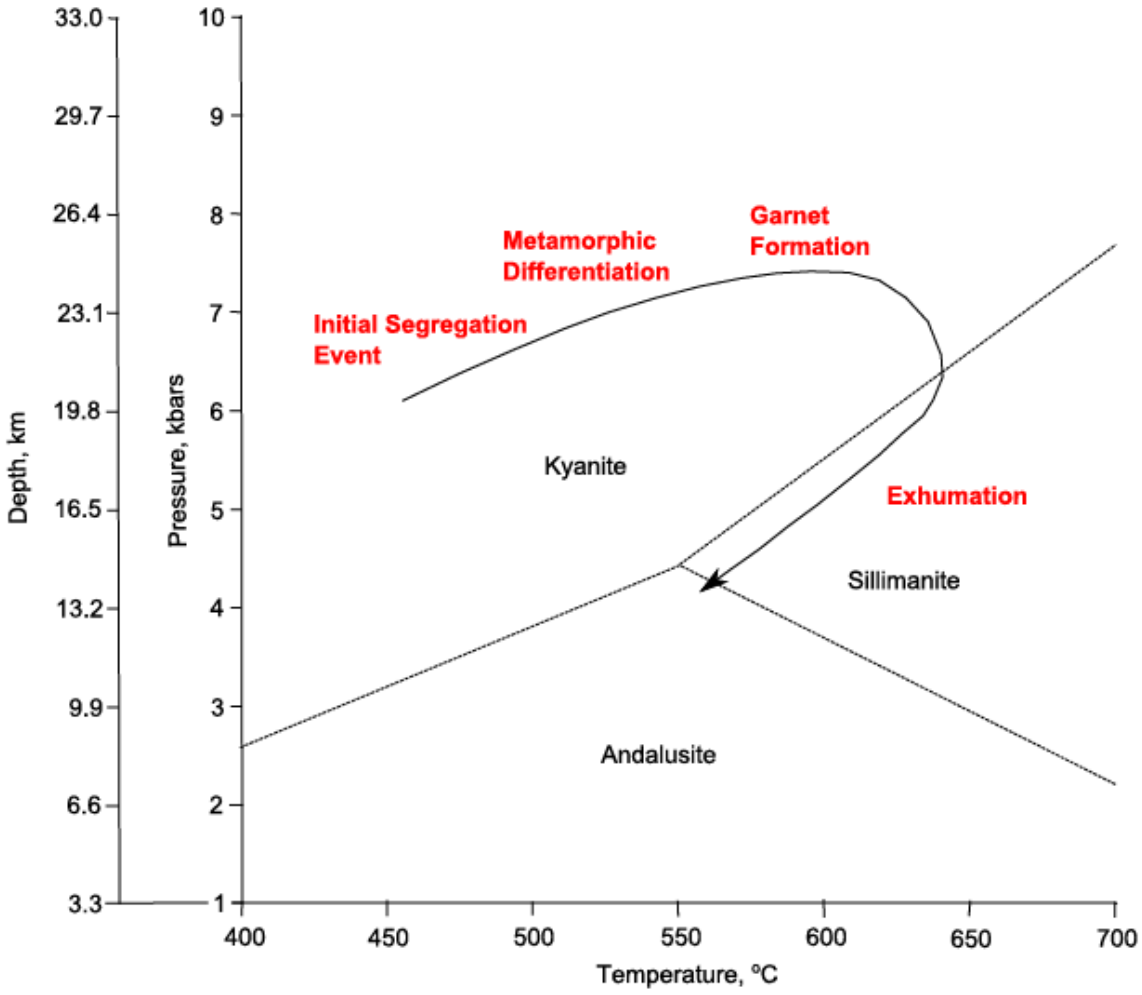

Figure 3.14. Proposed P-T evolution of the Haimanta Group metasediments in terms of garnet formation. Red text represents timing of important metamorphic events. After Chambers et al. (2009).

Parameter	Symbol	Unit	Source
Distance	L	Dimensionless	(Houseman et al.,
Strain-rate	$1/ T_0$	(Basil)	2008)
Velocity	L/ T_0		
Density	ρ_0		
Viscosity	η_0		
Basil internal timestep	IDT0	20	(Piazolo et al.,
Strain increment	$\Delta\gamma$	0.05	2002)
Strain rate	$\dot{e}$	$1 \times 10^{-13} s^{-1}$	(Law et al., 2013)
Real world strain rate	$\dot{e}_{Piazolo}$	1.6×10^{-12} s-1	(Piazolo et al.,
Grain boundary mobility	M_{gb}	1×10^{-12} $m^2 s^{-1} J^{-1}$	2002)
Base viscosity (quartz)	η_0	3.15×10^{18} Pa-s	
Base viscosity (mica)	η_0	3.15×10^{17} Pa-s	
Dislocation density	ρ	m^{-2}	
Recovery factor	$R_{recover}$	0.94	(Piazolo et al.,
Stress scaling factor	τ_{scale}	10^8 Pa	2002)
Density scaling factor	ρ_{scale}	10^{13} m^{-2}	
Time scaling factor	t_{scale}	3.1536×10^{10} s	
Length scaling factor	l_{scale}	10^{-3} m	

Table 3.1. Parameters used in the modeling experiment with units and source (if any).

APPENDIX

The Effects of Diffusion, Grain Boundary Migration and Temperature on the Garnet-Biotite Exchange Reaction

McCall, K.E. and Caddick, M.J.

1. Creation of an Elle File

To create the simulated microstructure, consisting of the typical mineralogy in a layered pelitic schist (biotite, garnet, and quartz) used in the following experiments, instructions laid out in the Elle Microstructural Modeling book (Bons et al., 2008) and described in detail below, were used. The Gimp 2.8© image manipulation program was first used to create a raster data file of the microstructural configuration and because the Elle program maps any rectangular bounding box as a square, a square box with dimensions of 100 x 100 pixels, as suggested in the Elle book (Bons et al., 2008) was used. Each patch of pixels with a unique color is considered a single grain (flynn in Elle terminology) and therefore light gray and dark gray were chosen to represent quartz grains, light yellow and dark yellow to represent biotite, and red to represent garnet (Figure A.1). To create the rectangular biotite grains (yellow) and square garnet grains (red) the rectangular select tool from the Gimp toolbox and was used and then the bucket fill tool to fill in the desired area. The same was done for quartz grains (gray), but using the circle select tool to create the grain outline. The pencil tool (pixel size set to 1.00) was then used to fill in any missing spaces in the microstructure so that all grains were touching in the 100 x 100 pixel box. An important step to remember when creating Elle-compatible image files is that you must not draw the grain boundaries as separate lines and instead allow the created grain shapes to define grain boundaries in order to minimize the total number of (x,y) coordinate positions in the pixel system. Furthermore, created grains wrap around horizontal and vertical boundaries, meaning the dark yellow biotite grain in the top of the microstructure continues to the bottom of the microstructure (Figure A.1).

To save the raster file and convert to an Elle-compatible format (.elle), the file was exported as a .png file. Then, using the elle executable file: (ppm2elle.exe), located in the file extension: C:\elle\elle\binwx, the newly created file was loaded and saved as a new Elle-compatible file (.elle). The next step in the process was to run tide.exe by loading the newly created Elle file, selecting: Run→Run Options and changing "Stages" to 1 and the UserData field 1 to 0.01 (all the other Userdata values to 0). This step was done to ensure the spacing between the points that make up the grain boundaries was 0.01 Elle units (as suggested in the Elle book). After the above step, the number of run "Stages" was changed to 100 to allow the microstructure to fully evolve before making any more changes to the Elle file. The newly

created .elle file is simply a text file used to describe the geometric, physical and chemical characteristics of the created microstructure and can therefore be modified with any text editor (Bons et al., 2008).

The Options, Flynns, Bnodes and Unodes Blocks were then edited using the guidelines in the Elle Microstructural Modeling book (Bons et al., 2008). The first few lines of the .elle text file represent the Options block. The Options block is used to define global parameters that affect all elements of the microstructure file (e.g. temperature, pressure, time). Details for how this block can be changed are found on page 397 in the Microdynamics Simulation book (Bons et al., 2008). The Flynns block of the text file represents the characteristics within the individual grains that make up the microstructure. The MINERAL attribute field (Figure A.2) assigns different grain properties dependent on the assigned mineralogy. A default value of QUARTZ was assigned to all grains unless otherwise specified. The numbers following the default assignment (Figure A.2) correspond to the individual grains (flynns) that were given either a MICA (biotite) or a GARNET mineral ID. The DISLOCDEN term represents the dislocation density, or the starting crystallographic defects (irregularities) within an individual grain. Following this are the grain boundary nodes (Bnodes) and concentration marker nodes (Unodes) blocks. They are similar to the Flynns block, but bnodes represent the boundary coordinates (x,y) that outline grains (flynns) and undoes define an (x,y) location and concentration. The first number in the Bnodes block, indicated by the text "LOCATION" in Figure A.2 is the bnode ID, followed by the (x,y) coordinates that define each grain boundary location. Each was given an initial default value of 5.00000000e-02 using the parameter CONC_A to indicate (X_{Fe} = 0.05). To input concentration values *within* individual grains (flynns), specific (x,y) coordinates were assigned using unodes. Those that fell within biotite were given an X_{Fe} concentration of 6.00000000e-02 and within garnet a concentration of 8.00000000e-02. All other undoes (within quartz) were given a default concentration of 0.00000000e-02 using the parameter U_CONC_A.

2. The Garnet-Biotite Cation Exchange Reaction

The experiments below are modeled after Experiment 5 in the Elle Microdynamics Simulation book (Bons et al., 2008) that was created to study the garnet-biotite cation exchange reaction [Fe-garnet + Mg-biotite ←→Mg-garnet + Fe-biotite]. Bons et al. (2008) infer five major

grain-scale processes controlling this exchange: (1) volume diffusion within garnets, (2) cation exchange between a garnet and its grain boundaries, (3) grain boundary diffusion, (4) cation exchange between a biotite and its grain boundaries and (5) volume diffusion within biotites. The Fe and Mg diffusion constants are assumed to be equal for these simulations, allowing the consideration of only one component (Fe) as being representative of the system behavior (Fe and Mg). The diffusion coefficient (K_D) is one widely used in geothermometry, experimentally estimated by (Ferry and Spear, 1978) and the relationship between temperature, K_D and diffusivities of cations according to Cygan and Lasaga (1985) and Hoffman et al. (1974). The diffusion-related processes were calculated using the guidelines put forth in Park et al. (2003), and the exchange-related processes between garnet, biotite and the grain boundary calculated using Martin and Doherty (1976). Reaction progress is always in the direction that lowers the Gibbs free energy within the system and once the direction is decided, the overall reaction is determined by the five sub-processes (Bons et al., 2008).

We attempted to model the compositional changes in garnet and biotite that develop during prograde metamorphism as temperature increases because of the changes in partitioning behavior of Fe/Mg ions in order to better understand diffusion processes as a result of the exchange reaction. These diffusion processes are then related to the potential for mineral growth during the evolution of microstructures in prograde metamorphic conditions. Our experiments differ from those presented in the Microdynamics Simulation book (Bons et al., 2008) with the added complexity of a microstructure consisting of multiple biotite and garnet grains present during the exchange reaction, in comparison to studying the interaction between one garnet and one biotite grain as done in Experiment 5. Furthermore, their experimental runs utilized a constant temperature or a cooling temperature to analyze the results of the exchange reaction, but never an increasing temperature as imposed in our experiments. Lastly, we added in the effects of grain boundary migration to determine the effects (if any) on the exchange reaction during prograde metamorphism.

The garnet-biotite exchange reaction is driven by instabilities due to disequilibrium in chemical free energy (Bons et al., 2008) and we hope that by understanding the processes during the exchange reaction, we can better understand the chemical driving forces for the diffusion processes controlling this reaction. It is known that the chemical components whose chemical potentials vary across the texture, control its development (White et al., 2008) as material

diffuses from regions of high chemical potential to regions of low chemical potential. Diffusion is controlled by these gradients in chemical potential and the rate that these species can diffuse in different parts of the rocks (e.g. intracrystalline vs. intergranular diffusion rates) (Fisher, 1973; Joesten, 1977; Brady, 1983; Carlson, 2002; Carlson and Gordon, 2004; White and Powell, 2011). The left y-axis of Figure A.3 represents the mole fraction of Fe inputted in the .elle file (unode concentrations). There is a zero starting concentration in quartz (Figure A.3) of both diffusing components (Fe and Mg), meaning no chemical gradient is present *within* quartz grains in these simulations. This schematic diagram represents the chemical driving force for the garnet-biotite exchange reaction and explains why there is never a change in the intragranular concentration of quartz grains in the following experiments because the exchange process is driven by the chemical potential gradients between Fe and Mg that are only present in biotite and garnet (Figure A.3). The lack of a compositional gradient between quartz and these minerals means quartz acts as a passive marker in the following simulations that experiences diffusion around its grain boundaries, but never *within*.

In a completely equilibrated mineral assemblage, all chemical potentials are equal and a lack of equilibrium on whatever scale implies the existence of chemical potential gradients that have not been flattened by diffusion (Thompson, 1959; Carlson, 2002; White et al., 2008; White and Powell, 2011). This means that in the following experiments, once an equilibrated mineral assemblage has been reached, there should be no evidence for diffusive processes still occurring. Because diffusion involves climbing an energy barrier by atoms between two stable states, temperature is thought to have the strongest effect on diffusion coefficients (Ganguly, 2002) and diffusion rates are known to increase exponentially with absolute temperature (Carlson, 1999). Another goal of the following experiments is to observe how different starting temperatures affect the exchange reaction between garnet and biotite in an evolving microstructure.

2.1 Grain-Scale Processes Considered

Each process algorithm in the Elle program is written to be independent of any particular driving force, allowing for the use of several independent driving forces to describe a process (Jessell et al., 2001). The following experiments are based on Experiment 5c in the Elle Microdynamics Simulation book (Bons et al., 2008) that utilized the elle_gbdiff.exe and

elle_exchange.exe process algorithms. The elle_gbdiff.exe algorithm performs a finite difference grain boundary diffusion calculation for a uniform-width grain boundary network and constant diffusivity, set to diffuse the property: CONC_A (default value of 0.05). This algorithm only calculates concentration differences along grain boundaries (bnodes), limiting this process to only modeling intergranular diffusion. The elle_gbdiff.exe code utilizes Effective Binary Diffusion, that works to diagonalize the diffusion matrices by reducing a multicomponent system to the mathematical forms of binary diffusion (Ganguly, 2002), treating the diffusing species (Fe) as the solute and the rest of the solution as the solvent, creating a binary mixture (Chakraborty and Ganguly, 1992). The Kappa parameter for the elle_gbdiff.exe code is set to (2.0e-9) and represents the pre-exponential factor used to calculate the diffusion coefficient D(T) using the Arrhenius equation $D(T) = Kappa*exp(-E_a/(RT))$. In this code, the activation energy for diffusion (E_a) has been set to 239 kJ/mol and diffusion stages set to 500.

The elle_exchange.exe process algorithm is used to simulate lattice diffusion *within* grains and cation exchange between the boundary and grains using a finite difference lattice diffusion calculation that is based on the property: U_CONC_A. Only grain margins are directly involved in the (Fe/Mg) exchange reaction as the model changes the Fe/Mg ratio toward the value of an experimentally determined K_D value (Bons et al., 2008). The Kappa parameter for the elle_exchange.exe algorithm is set to (30.90528) and the temperature increment is (+ 0.5), changed from (- 0.5) in the original Elle experiment (5c). Both are used to calculate diffusion using the Arrhenius equation $D(T)=Kappa*exp(-E_a/RT))$. The activation energy for diffusion (E_a) has the same value used for the elle_gbdiff.exe algorithm (239 kJ/mol) and exchange stages are also set to 500.

The effects of grain boundary migration were not considered in the original garnet-biotite exchange experiment presented in the Microdynamics Simulation book (Bons et al., 2008), although grain boundary migration is thought to be a major process controlling the development of microstructures undergoing deformation-induced dynamic recrystallization, especially in quartz-rich samples (Urai et al., 1986; Drury and Urai, 1990; Piazolo, 2001; Piazolo et al., 2002). In Experiment 1 the effects of grain boundary migration were not considered in the garnet-biotite exchange reaction, but in Experiment 2, the addition of the Elle process algorithm elle_gbm.exe was included to account for the effects of grain boundary migration during the exchange reaction in the evolution of the microstructure. The elle_gbm.exe algorithm utilizes the reduction in

surface energy as the driving force for grain boundary migration to achieve local minimum surface energy. Surface energy is a function of the c-axis misorientation angle between two adjacent grains or subgrains and migration occurs due to the difference in stored internal strain energy (zero initially) as indicated by the DISLOCDEN field in Figure A.2 and in chemical potential due to the curvature between adjacent grains (Bons et al., 2008). This algorithm, employed in other simulations by Bons (2001) and Piazolo et al. (2002), takes four trial displacements at a small distance from the original node positions and the displacement producing the maximum energy dissipation is chosen as the movement direction using the following equation: $\sigma_{gbm} = v/m$; the driving stress (σ_{gbm}) or the driving force per unit area of grain boundary, the velocity of the boundary (v) and the grain boundary mobility (m), in units of m/J-s.

3. Experiments

Figure A.4 displays the starting configuration for the microstructure used in the following experiments. The dimensions of the simulated microstructure are 10 mm x 10 mm. The left image represents the mineral identity of each grain and the right image represents the corresponding initial composition within each grain and the compositions along the grain boundaries. In Experiment 5c, the simulation lasts 1200 timesteps to achieve 50 Myr of microstructural evolution (Bons et al., 2008). We used this same time frame as our guideline, meaning each timestep in an experiment represents 41,666.67 years. Our simulations differ in that the temperature increment for the elle_exchange.exe algorithm is set to (+ 0.5), compared to (- 0.5) in Experiments 5c, so that each timestep in the following experiments involves an increase in temperature by 0.5 °C to simulate the exchange reaction occurring during prograde metamorphism conditions. Pressure was kept at a constant value of 5 kbar for both simulations to simulate average conditions during prograde metamorphism and not increased with increasing temperature because in prograde metamorphism, pressure increase is negligible when compared to temperature (Carlson, 1989).

3.1 Experiment 1: No Grain Boundary Migration

In this experiment, only the Elle process algorithms elle_gbdiff.exe and elle_exchange.exe were considered, making this experiment the most similar to Experiment 5c described above. The experiment processes allow for concentrations to migrate within grains (unodes) and around grains through the grain boundary network (bnodes), but does not allow for the migration of grain boundaries. Four experimental runs were tested with starting temperatures of 400, 500, 600, and 700 °C at a constant pressure of 5 kbar.

3.1.1 Results

In Figure A.5: 1b, the initial concentrations in garnet and biotite are maintained, unlike figure A.4b, at a higher starting temperature. It appears that at lower starting temperatures, grain boundary diffusion processes dominate initially, as a result of the initial concentrations within the garnet and biotite grains. This is represented by the increase in concentration (yellow) of the grain boundaries between 1a and 1b and only after do the concentrations within the individual grains begin to change. Figure A.5: 4b displays the highest concentrations (0.1) in the garnet rim. This high Fe concentration in garnet rims is a result of the exchange reaction occurring along the grain boundaries due to the change in Fe/Mg ratio as garnet loses some Fe to biotite. At this higher starting temperature, it appears grain boundary diffusion and intragranular exchange within the garnet crystals are occurring simultaneously. This is not the case for intragranular diffusion within the biotite grains at a lower starting temperature that retain the 0.06 initial concentrations (yellow) after 41,667 years (Figure A.5:1b-4b). For all starting temperatures, first grain boundary concentrations increase, indicated by the initial green color (0.05) changing to yellow after 41,667 years (Figure A.5: 1a-4a). The only grain boundaries exempt from this change are the concentrations around garnet grains that decrease to blue (0) immediately and the concentrations between adjacent quartz grains that appear to keep the starting concentration (0.05) up to 41,667 years. This implies that the areas between quartz grains are the locations in the microstructure with the smallest initial chemical potential gradients. The opposite is true for the areas surrounding garnet grains that appear to have the strongest initial concentration

gradient between Fe and Mg (Figure A.3) and should parallel the highest gradient in chemical potential, thus the largest driving force for diffusion.

In Figure A.5: 1b, the grain boundary concentrations are a darker yellow color (higher concentration) compared to the lighter yellow grain boundaries in 4b. All grain boundary concentrations tend to 0 after the initial increase (to yellow) from the 0.05 concentration, but it appears that with a lower starting temperature, the decrease process also happens at a slower rate due to slower diffusion rates with a lower starting temperature. By 83,333 years for all simulations (Figure A.5: 1c-4c) all of the Fe has been transported through the grain boundary network from garnet to biotite, signifying the end of the Fe/Mg exchange reaction: (Fe-garnet + Mg-biotite ←→Mg-garnet + Fe-biotite) and a reaching of equilibrium conditions. As each experimental run trends to equilibrium, the composition of all grain boundaries tend to 0, intragranular concentrations within biotite grains tend to 0.1, within garnet tend to 0 and within quartz stay at 0 (consistent through entire experiment). The concentration within biotite grains (0.1) at the end of each simulation is different than the concentration within garnet grains (0) because a chemical gradient remains in the system, although the gradient in chemical potential driving the exchange reaction and resulting diffusion is no longer present. All simulations reach equilibrium over less than 125,000 years (Figure A.5: 1d-4d) regardless of starting temperature. This implies that the exchange reaction happens very quickly when grain boundary migration is not considered and that the driving force for the exchange reaction between garnet and biotite in prograde metamorphism is large if initial chemical gradients are present. In terms of the initial nucleation of metamorphic minerals (prior to the exchange reaction), these results imply that nucleation will also happen quickly once a gradient is established due to rapid diffusion to remove chemical potential gradients.

3.2 Experiment 2: Grain Boundary Migration Turned On

In this experiment, the Elle process algorithms: elle_gbdiff.exe, elle_exchange.exe, and elle_gbm.exe were implemented. With the addition of the elle_gbm.exe process algorithm, the garnet-biotite exchange reaction happened at a much slower rate than in the previous experiment. To account for this, concentrations presented in the following results include the entire 50 Myr

timespan (based on Experiment 5c) for starting temperatures of 400 °C and 500 °C at a constant pressure of 5 kbar.

3.2.1 Results (400 °C)

After 0.25 Myr (Figure A.6a) diffusion along grain boundaries is evident in the depletion halos (blue) around garnet-rich areas in the microstructure. At this stage, the lowermost garnet displays a zero intragranular concentration (blue) in contrast to the other two garnet grains that retain the initial (0.08, orange) concentration within. No migration of grain boundaries is observed at this early stage of the simulation. The bottom garnet in the microstructure that loses its starting intragranular concentration first represents the place in the microstructure with the highest initial chemical potential gradient because it is the location of the first exchange reaction as the system moves towards an equilibrium configuration of Fe-poor garnet and Fe-rich biotite. With the decrease in concentration around the garnet-rich area of the microstructure, the concentrations within the surrounding biotite grains also decrease (Figure A.6a).

Throughout the first 4 Myr of the simulation (Figure A.6), very little change in the grain boundary concentrations occurs after the initial concentration gradients are established due to the breakdown of the lowermost garnet. It appears that after the first period of intragranular exchange and resultant diffusion along grain boundaries, grain boundary migration processes take over. After 1.25 Myr (Figure A.6e), the grain boundaries of adjacent quartz grains in the garnet-rich area begin to migrate from their initial configuration (Figure A.4). Later in the experiment, after 2.5 Myr, the adjacent quartz grain boundaries not touching garnet grains also begin to show evidence of grain boundary migration (Figure A.6j). The only grain boundaries that migrate in the simulated microstructure are those of adjacent quartz grains. This is due to the higher grain boundary mobility value (m) in grains with the mineral ID of quartz compared to the less mobile phases in the microstructure: garnet and biotite. After the initial 4 Myr of the exchange reaction (Figure A.6), grain boundary migration processes appear to stop and diffusion processes regain dominance. This could be because of the introduction of a new energetic driving force as a result of the energy released due to the migration of quartz grain boundaries in the earlier stages of deformation, or the result of increased temperature later in the experiment, causing faster diffusion rates.

In Figure A.7, with 3.125 Myr between each image, a much clearer change in the grain boundary concentrations is observed, especially after the concentrations within the remaining two garnet grains begin to change (Figure A.7d). With a change in the garnet rim concentrations, the surrounding grain boundary concentrations also increase (blue to green), as the garnets begin to "give up" more Fe to the surrounding grain boundaries. This represents the stage in the microstructure development where intragranular exchange and grain boundary diffusion are once again the driving force for grain-scale processes. The difference in timing between the loss of intragranular (Fe) concentration of the lowermost garnet grain (reducing to zero) after 0.25 Myr (Figure A.6a), and the other two garnet grains after 46.875 Myr (Figure A.7o) implies two separate periods of diffusion as a result of the garnet-biotite exchange reaction occurring across the microstructure instead of a singular, more gradual diffusion response.

After the initial decrease in intragranular concentration of the biotite grains surrounding garnet grains (Figure A.6a), no change is observed in biotite concentrations until 34.375 Myr (Figure A.7k) wherein the left biotite grain displays a decrease in concentration (yellow to green) in the third concentration marker (unode) in the middle row. This is followed by other concentration markers within biotite beginning to show a decrease in concentration as all of the garnet grains experience a simultaneous decrease in concentration. The decrease in biotite concentrations is the first step towards an eventual equilibrium configuration for the microstructure that should look similar to that of the end results from Experiment 1 (Figure A.5), wherein the concentration within garnet grains is (0) and within biotite (0.1) after the exchange reaction has run to completion. The zero concentration (blue) along all grain boundaries in the following step (Figure A.7l), represent conditions of metastable equilibrium wherein there is still a chemical potential gradient that will drive future diffusion, but without the loss of some component (Fe) from within a garnet grain, no diffusion along grain boundaries is occurring at this stage in the simulation. After 40.625 Myr (Figure A.7m) only one garnet retains an interior concentration greater than zero. This garnet grain is unique in that only one side is exposed to the surrounding biotite grains (Figure A.4) as opposed to the other two garnets grains that have two sides touching biotite grains. This means that the other two garnets were exposed to higher chemical driving forces for diffusion (chemical potential gradients) because of a larger interaction with adjacent biotite grains and thus reached an equilibrium configuration before this other garnet. After 50 Myr (Figure A.7p) all of the garnets grains have reached an intragranular

concentration of 0 and the internal composition of the biotite grains are now the driving force for grain boundary diffusion as this system moves towards equilibrium, but never fully reaches these conditions (the end of the garnet-biotite exchange reaction) during the simulation.

3.2.2 Results (500 °C)

If the starting temperature is increased from 400 °C to 500 °C, there are two major observable changes in the microstructure evolution: first, there is a smaller initial depletion halo in Fe concentration around the garnet-rich area of the microstructure (Figure A.8a). This is a result of the bottom garnet not losing its initial concentration by 0.25 Myr, leading to a smaller driving force for diffusion being established during the early stages of this simulation than in the 400 °C starting temperature experiment. Early in the microstructure development history, the lowest concentrations are still present in the grain boundaries surrounding the garnet-rich portion of the microstructure (Figure A.8a), implying this is still the area with the highest chemical potential gradient early on in the evolution of the microstructure, regardless of the starting temperature. The other major difference between these two simulations is that with an increase in starting temperature, there is no evidence for the effects of grain boundary migration processes at any point during the microstructure development and instead diffusion processes dominate though the entire simulation. Throughout the modeled 50 Myr during the exchange reaction, grain boundaries between adjacent quartz grains never change position from their initial configuration (Figure A.4). The lack of any evidence for grain boundary migration when the starting temperature is increased by 100 °C implies that at 500 °C, diffusion processes as a result of the exchange reaction are a greater driving force for grain-scale processes than grain boundary migration processes, driven by surface area minimization. This observation is further supported by the more evident change in the concentrations along grain boundaries from 0.25 Myr to 0.5 Myr (Figure A.8a-b) when all concentrations display a slight increase.

This change in grain boundary concentrations then stops until the intragranular concentrations of garnet crystals start to increase from the initial concentration at about 2.25 Myr (Figure A.8i). This is at 527 °C for the (T_I = 500 °C) simulation. This temperature is similar to the temperature when the increase in intragranular concentration is observed for the (T_I = 400 °C) simulation. In fact, Figure A.7d and Figure A.8p (550 °C and 548 °C, respectively) show a

similar pattern in garnet concentrations when ignoring the bottom garnet that experiences an early loss of Fe concentration for only the 400 °C starting temperature simulation. The consistent change in the interior concentration of the garnet crystals around 550 °C and 5 kbar for both simulations represents the point where garnet is predicted to begin to breakdown in prograde metamorphism as temperature increases and diffusion of components within garnet proceeds more rapidly. If garnet nucleation was suppressed until up temperature for some reason in nature, this could also represent the conditions where components began to diffuse fast enough to overcome kinetic barriers to nucleation and growth to grow a new crystal.

Through the last 2 Myr of the early microstructure development (Figure A.8i-p), the garnet concentrations slowly increase at the rim with no noticeable changes occurring in the concentrations along the surrounding grain boundaries of the garnet crystals, or anywhere else in the microstructure. Between 0.75 Myr (Figure A.8c) and 4.0 Myr (Figure A.8p), there is a slight observable difference in grain boundary concentrations, but no major change is seen over this ~3 Myr time span. In Figure A.9, the timespan between each image is 3.125 Myr, as opposed to 0.25 Myr in Figure A.8 and as a result, the diffusion of concentrations through grain boundaries in response to the increase in concentration of Fe at garnet rims is more apparent. The diffusion of Fe through grain boundaries away from garnet is evidenced in the first changes in grain boundary concentrations occurring around quartz grains that are touching garnet crystals, while quartz grain boundaries that are not touching garnet grains remain at their previous concentration (Figure A.9a-b). This indicates the direction the Fe concentration is migrating (from garnet to biotite) along the grain boundaries in between as this system attempts to reach equilibrium through the garnet-biotite exchange reaction.

As the exchange reaction continues, the lowest grain boundary concentrations (blues and greens) surround the garnet-rich areas of the microstructure and the highest concentrations are in the biotite-rich area, bottom vs. top of microstructure (Figure A.9d). The first garnet to lose its intragranular composition is the uppermost garnet in the simulated microstructure (Figure A.9i). This represents the area this microstructure with the highest initial chemical potential gradient, resulting in the highest driving force for diffusion processes as the system moves to remove the concentration gradients within garnet crystals. The center garnet is the last to lose its interior concentration in both experiments and in the 500 °C starting temperature simulation, the lowest grain boundary concentrations remain around this garnet (blue) as the grain boundary

concentrations around the other garnets begin to increase (green), Figure A.9e. In the lower temperature simulation, this garnet loses its concentration at 925 °C (Figure A.7n) versus this simulation at 913 °C (Figure A.9k). The proximity of these two temperatures, regardless of starting temperature is interpreted to represent the conditions in the microstructural evolution when Fe-Mg compositional gradients in garnet should be expected to be removed in natural samples.

The size of the chemical potential gradient established between Fe and Mg is directly related to the time it takes the concentration gradient (in garnet in biotite) to be removed because the chemical potential gradient between components (Fe and Mg) drives the diffusion processes between the two minerals during the exchange reaction. After 37.5 Myr (Figure A.9l), all of the concentrations within garnet crystals have been reduced to zero and the concentration within biotite grains becomes the driving force for the diffusion processes because it is the only mineral left that has a chemical potential gradient remaining. This simulation is different from the lower temperature simulation because here, there is no evidence for intragranular exchange in biotite grains (concentration changes) before intragranular Fe concentrations in garnet are removed. After 46.875 Myr of diffusion (Figure A.9o), the interior concentrations in biotite grains begin to display a decrease in concentration. This continues to the end of the simulation with no change in the interior garnet concentrations. If recorded for longer, we predict these interior concentrations would eventually increase to 0.1, signifying the end of the garnet-biotite exchange reaction, similar to the end configuration for Experiment 1 (Figure A.5).

4. Conclusions

The experiments above allow a look into the interaction between temperature, diffusion and grain boundary migration during the development of microstructures undergoing the garnet-biotite exchange reaction that occurs too slowly to be observed in natural settings. The experimental results improve our ability to interpret the driving forces for grain-scale processes in natural samples that formed over millions of years and also highlight the importance of grain boundary migration on the timescale of diffusion during the garnet-biotite exchange reaction. Reaction time can be estimated using the above models by determining how long it took for the initial diffusion curves (Figure A.3) to “smooth out” (Carlson, 2006). In every experiment,

diffusion occurs along grain boundaries in response to the initial intragranular concentrations in garnet and biotite (Figure A.4) to complete the garnet-biotite exchange reaction: (Fe-garnet + Mg-biotite ←→Mg-garnet + Fe-biotite). Both experiments display lower grain boundary concentrations around garnet grains during early stages of microstructure development and higher grain boundary concentrations around biotite grains because garnet is losing Fe to biotite as the system attempts to reach an equilibrium state. This diffusion along grain boundaries is driven by chemical potential gradients established as a result of the initial different concentrations within these two minerals (0.08 vs. 0.06, Figure A.3). Because of the higher initial Fe composition within garnet grains, garnet-rich areas in the microstructure have a higher chemical driving force for diffusion and undergo intragranular exchange, resulting in grain boundary diffusion first, as a result of the changing garnet compositions. This is later followed by biotite, after the initial compositional gradients within garnet have been removed.

When grain boundaries are allowed to migrate (Experiment 2), the results look different in the initial diffusion stages (Figure A.6 and A.8) than the results of Experiment 1 (Figure A.5), where grain boundary migration processes were not allowed to occur. In Experiment 1, the concentrations between adjacent quartz grains remain at the initial concentration (0.05, Figure A.5: 1b-4b) as the other grain boundaries begin to change in concentration. In Experiment 2, in the T_I = 400 °C simulation (Figure A.6a) the adjacent quartz grain boundaries follow the general pattern of the surrounding grain boundary concentration changes. However, in the T_I = 500 °C simulation, only the grain boundary concentrations in adjacent quartz grains that *also* touch garnet grains remain green initially (Figure A.8a), and not quartz grain boundaries elsewhere in the microstructure. This difference in the quartz grain boundary concentration pattern between simulations with different starting temperatures in Experiment 2 is a result of the combination of diffusion and grain boundary migration processes affecting quartz grain boundaries that appears to be stronger in the lower starting temperature simulation (T_I = 400 °C), as evidenced by the larger discrepancy between the adjacent quartz grain boundary concentrations observed for this simulation when compared to the results from Experiment 1. The results of Experiment 2, wherein grain boundary migration processes were allowed to occur, suggest that grain boundary migration processes only affect the microstructural evolution at lower temperatures (T_I = 400 °C) and at higher temperatures (T_I = 500 °C), exchange processes and resultant grain boundary diffusion dominate the microstructural evolution with no observable migration of grain

boundaries. For observation of natural samples, this means the effects of grain boundary migration are less important when attempting to understand the evolution of microstructures developed as a result of the garnet-biotite exchange reaction at higher temperatures.

The consistent change in the interior concentration of garnet crystals around 550 °C and 5 kbar for both starting temperatures in Experiment 2 represents the conditions where garnet is predicted to begin to breakdown in prograde metamorphism if grain boundary migration processes are considered. In Experiment 2, only in the T_I = 400 °C simulation does the bottom garnet lose its starting intragranular concentration after 0.25 Myr (Figure A.6a). Furthermore, in the T_I = 400 °C simulation, the lowermost garnet is the first to lose its intragranular concentration, but in the T_I = 500 °C simulation, the top garnet is the first to experience a decrease to zero in Fe concentration. Both garnet crystals have two sides exposed to surrounding biotite grains and thus are expected to have similar chemical potential gradients established between Fe and Mg, driving diffusion processes. The different pattern between simulations with identical process algorithms imposed, but different starting temperatures, highlights the importance of temperature on the interpretation of microstructure development. Results show that different temperature conditions can not only affect the grain-scale processes (i.e. if grain boundary migration processes will occur), but also which crystal has the highest chemical potential gradient established and hence the fastest diffusion to remove these gradients.

While these simulations are limited in that they do not simulate the initial growth of garnet, biotite, or any other metamorphic mineral before the exchange reaction begins between garnet and biotite, by simulating the breakdown of garnet once it is formed we can better understand the overall diffusion processes occurring during the development of a pelitic microstructure that should also control the diffusion of necessary components to a growing nucleus. In order to form a porphyroblastic microstructure, (e.g. garnet, staurolite, andalusite), a substantial barrier to the nucleation of new phases is usually required. This nucleation difficulty is known to be an important and possibly leading cause of reaction overstepping in metamorphic systems (Rubie, 1998; Waters and Lovegrove, 2002; Pattison and Tinkham, 2009). The rates of three key processes are thought to control crystal growth: heat flow, intergranular diffusional transport and accretion on growth surfaces (Fisher, 1978; Carlson, 2011).

If nucleation of a porphyroblast was suppressed in nature until up temperature because of limited intergranular diffusional transport, the point in the simulated microstructure development

wherein components begin to diffuse fast enough to remove chemical gradients in garnet could be representative of suitable conditions to overcome kinetic barriers to nucleation and growth (if present) in nature for a particular pelitic rock assemblage. Additionally, the potential for nucleation across an evolving microstructure can be observed on the basis of chemical potential gradients that are mirrored in the diffusion profiles in the presented models. Locations with small initial chemical potential gradients should represent locations with small nucleation potential early in the prograde history (pre-garnet growth) and locations with high initial chemical potential gradients should represent locations with large nucleation potential (garnet locations) in the above simulations.

References

Bons, P. D., 2001, Development of crystal morphology during unitaxial growth in a progressively widening vein: I. The numerical model: Journal of Structural Geology, v. 23, p. 8.

Bons, P. D. D., Koehn, D., and Jessell, M. W., 2008, Microdynamics Simulation, Springer.

Brady, J. B., 1983, Intergranular diffusion in metamorphic rocks: American Journal of Science, v. 283-A, p. 181-200.

Carlson, W. D., 1989, The significance of intergranular diffusion to the mechanisms and kinetics of porphyroblast crystallization: Contributions to Mineralogy and Petrology, v. 103, no. 1, p. 1-24.

Carlson, W.D., 1999, The case against Ostwald ripening of porphyroblasts: Canadian Mineralogist, v. 37, p. 403-413.

Carlson, W. D., 2002, Scales of disequilibriumn and rates of equilibration during metamorphism: American Mineralogist, v. 87, p. 185-204.

Carlson, W. D., 2006, Rates of Fe, Mg, Mn, and Ca diffusion in garnet: American Mineralogist, v. 91, no. 1, p. 1-11.

Carlson, W. D., 2011, Porphyroblast crystallization: linking processes, kinetics, and microstructures: International Geology Review, v. 53, no. 3-4, p. 406-445.

Carlson, W. D., and Gordon, C. L., 2004, Effects of matrix grain size on the kinetics of intergranular diffusion: Journal of Metamorphic Geology, v. 22, no. 8, p. 733-742.

Chakraborty, S., and Ganguly, J., 1992, Cation diffusion in aluminosilicate garnets - experimental-determination in spessartine-almandine diffusion couples, evaluation of effective binary diffusion-coefficients, and applications: Contributions to Mineralogy and Petrology, v. 111, no. 1, p. 74-86.

Cygan, R. T., and Lasaga, A. C., 1985, Self-diffusion of magnesium in garnet at 750^{o} to 950^{o}: American Journal of Science, v. 285, no. 328-350.

Drury, M. R., and Urai, J. L., 1990, Deformation-related recrystallization processes: Tectonophysics, v. 172, p. 235-253.

Ferry, J. M., and Spear, F. S., 1978, Experimental calibration of the partitioning of Fe and Mg between biotite and garnet: Contributions to Mineralogy and Petrology, v. 66, p. 113-117.

Fisher, G. W., 1973, Non-equilibrium thermodynamics as a model for diffusion-controlled metamorphic processes: American Journal of Science, v. 273, p. 897-924.

Fisher, G. W., 1978, Rate laws in metamorphism: Geochimica Et Cosmochimica Acta, v. 42, no. 7, p. 1035-&.

Ganguly, J., 2002, Diffusion kinetics in minerals: Principles and applicatinos to tectono-metamorphic processes: EMU Notes in Mineralogy, v. 4, p. 39.

Hoffman, A. W., Giletti, B. J., Hinthorne, J. R., Anderson, C. A., and Comaford, D., 1974, Ion microprobe analysis of a potassium self-diffusion experiment in biotite: Earth and Planetary Science Letters, v. 24, no. 48-52.

Jessell, M., Bons, P., Evans, L., Barr, T., and Stuwe, K., 2001, Elle: the numerical simulation of metamorphic and deformation microstructures: Computers & Geosciences, v. 27, no. 1, p. 17-30.

Joesten, R., 1977, Evolution of mineral assemblage zoning in diffusion metasomatism: Geochimica Et Cosmochimica Acta, v. 41, no. 5, p. 649-670.

Martin, J. W., and Doherty, R. D., 1976, Stability fo microstructure in metallic systems: Cambridge University Press.

Park, Y., Park, D., Evans, L., and Ree, J. H., 2003, An Elle-based 2-D model for cation exchange reaction between garnet adn biotite: J Virtual Explorer, v. 15, p. 14.

Pattison, D. R. M., and Tinkham, D. K., 2009, Interplay between equilibrium and kinetics in prograde metamorphism of pelites: an example from the Nelson aureole, British Columbia: Journal of Metamorphic Geology, v. 27, no. 4, p. 249-279.

Piazolo, S., 2001, Shape fabric development during progressive deformation. [PhD: Berichte aus der Geowissenschaft.

Piazolo, S., Bons, P. D., Jessell, M. W., Evans, L., and Passchier, C. W., 2002, Dominance of microstructural processes and their effect on microstructural development: insights from numerical modelling of dynamic recrystallization: Geological Society of London, Special Publications, v. 200, p. 22.

Rubie, D. C., 1998, Disequilibrium during metamorphism: the role of nucleation kinetics, *in* Taylor, P. J., and Obrien, P. J., eds., What Drives Metamorphism and Metamorphic Reactions?, Volume 138, p. 199-214.

Thompson, J. B., 1959, Local equilibrium in metasomatic processes, Wiley, New York, Researches in Geochemistry.

Urai, J. L., Means, W. D., and Lister, G. S., 1986, Dynamic recrystallization of minerals: American Geophysical Union Geophysical Monograph, v. 36, p. 161-199.

Waters, D. J., and Lovegrove, D. P., 2002, Assessing the extent of disequilibrium and overstepping of prograde metamorphic reactions in metapelites from the Bushveld

Complex aureole, South Africa: Journal of Metamorphic Geology, v. 20, no. 1, p. 135-149.

White, R. W., and Powell, R., 2011, On the interpretation of retrograde reaction textures in granulite facies rocks: Journal of Metamorphic Geology, v. 29, no. 1, p. 131-149.

White, R. W., Powell, R., and Baldwin, J. A., 2008, Calculated phase equilibria involving chemical potentials to investigate the textural evolution of metamorphic rocks: Journal of Metamorphic Geology, v. 26, no. 2, p. 181-198.

Figures

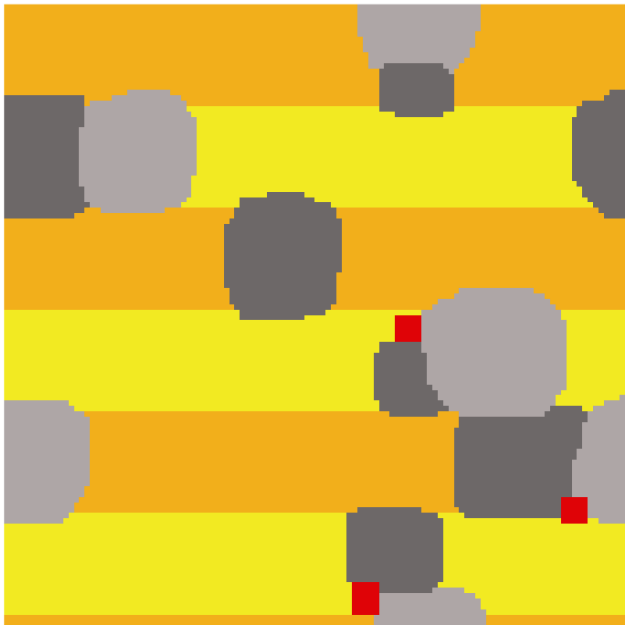

Figure A.1. Raster image of the simulated layered pelitic schist microstructure created using Gimp 2.8©

```
MINERAL
Default QUARTZ
1 MICA
5 MICA
7 MICA
9 MICA
10 GARNET
14 MICA
15 GARNET
17 MICA
18 GARNET
DISLOCDEN
Default 0.00000000e+00
LOCATION
0 0.5700431034 0.9892241379
CONC_A
Default 0.05000000e+000
UNODES
0 0.018433 0.983871
U_CONC_A
Default 0.00000000e-002
```

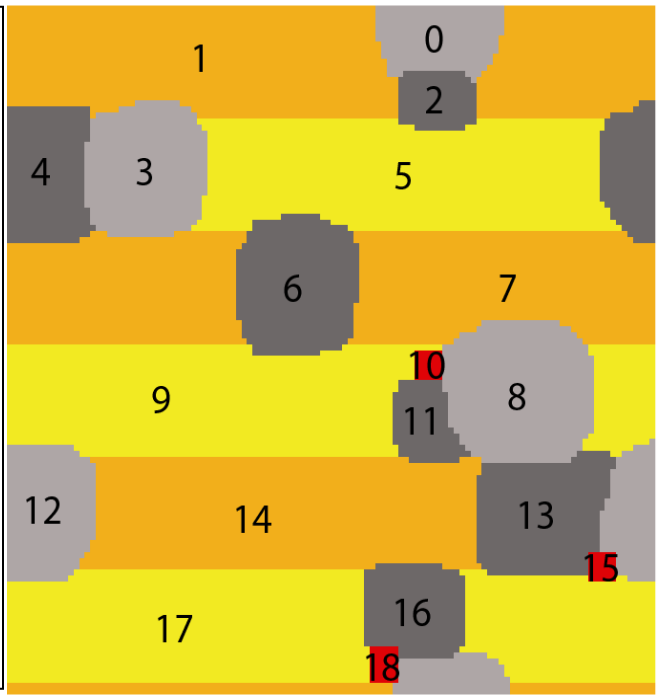

Figure A.2. Expert taken from the OPTIONS block of the created .elle text file. Grain (flynn) identities used to create this microstructure are numbered, followed by the (x,y) coordinates and compositions of the boundary nodes (bnodes), and (x,y) coordinates and compositions of the concentration markers (unodes).

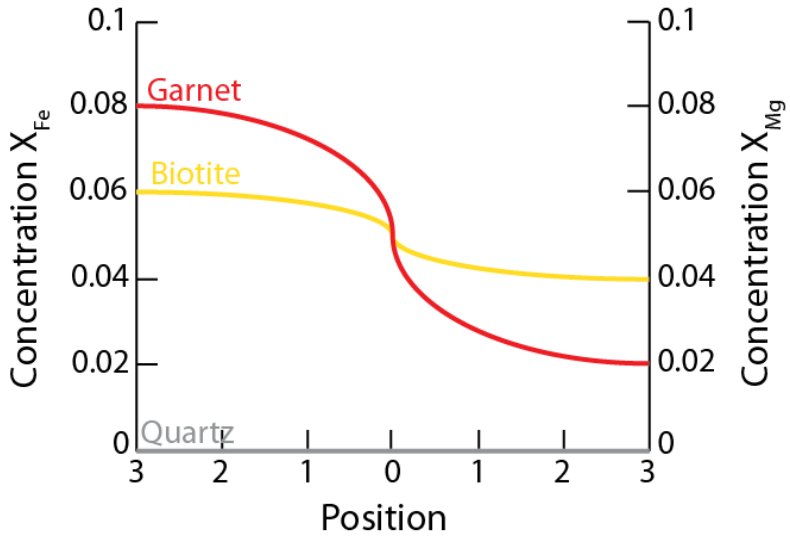

Figure A.3. Diffusion profile for garnet, biotite and quartz grains at initial conditions. Concentrations on the y-axis are in mole fraction of the major diffusing components (Fe and Mg) for the Effective Binary Diffusion system.

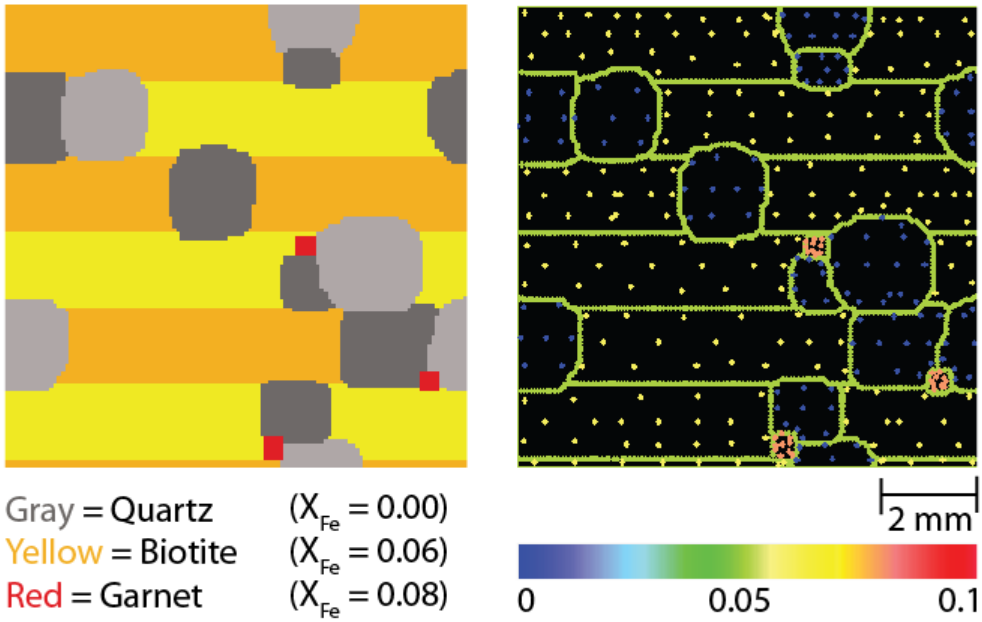

Figure A.4. Starting configuration and compositions for experiments. Colorbar indicates the initial concentrations for the figure on the right: initial grain boundary (bnode) concentration (0.05), initial intragranular concentrations (unode) within garnet (0.08), within mica (0.06), and within quartz (0.0).

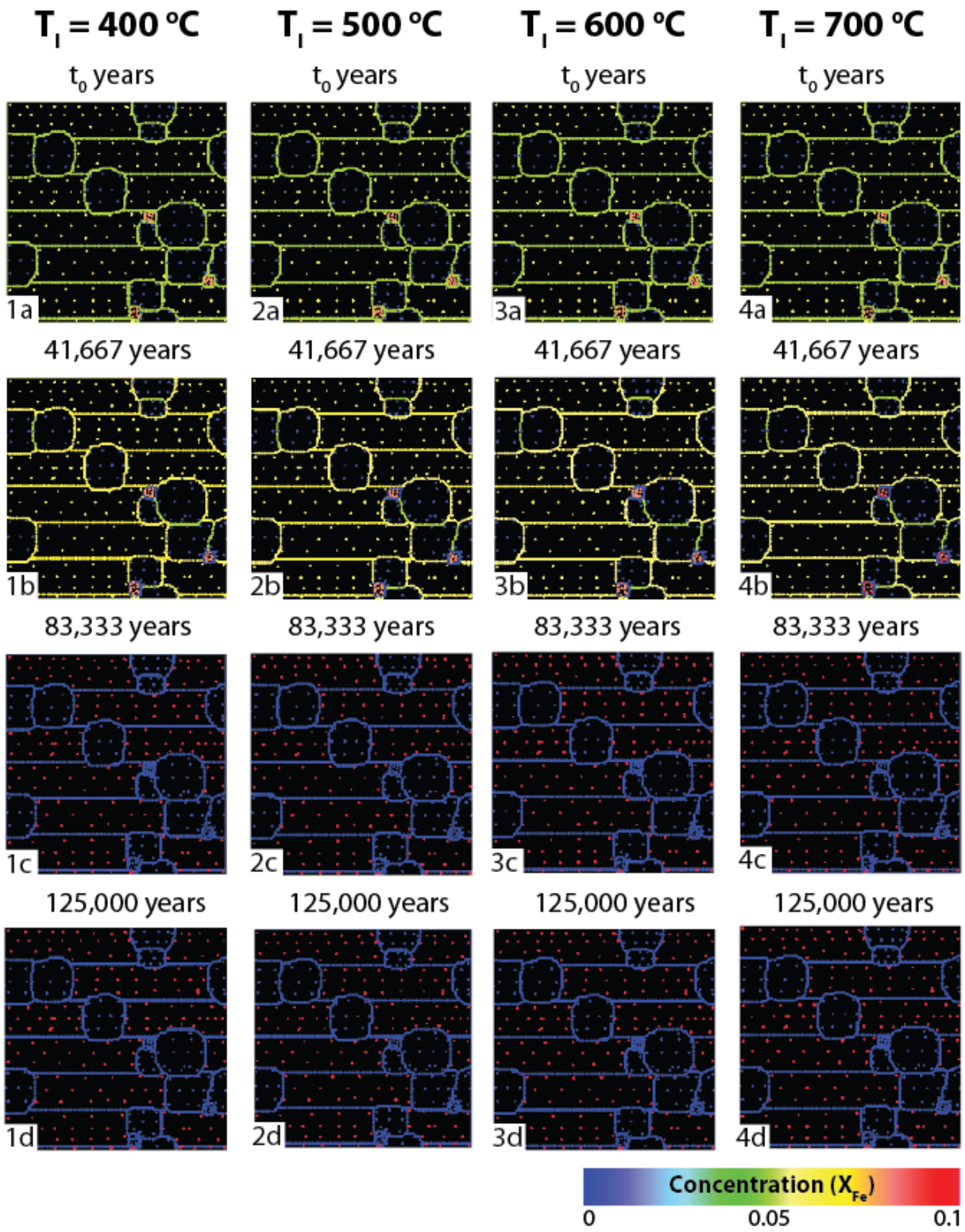

Figure A.5. Concentrations at different starting temperatures for 0 - 125,000 years of diffusion for Experiment 1. T_I denotes the starting temperature for each column. Each sequential image in a column represents an increase from the initial temperature by 0.5 °C (1.5 °C over the course of each simulation run).

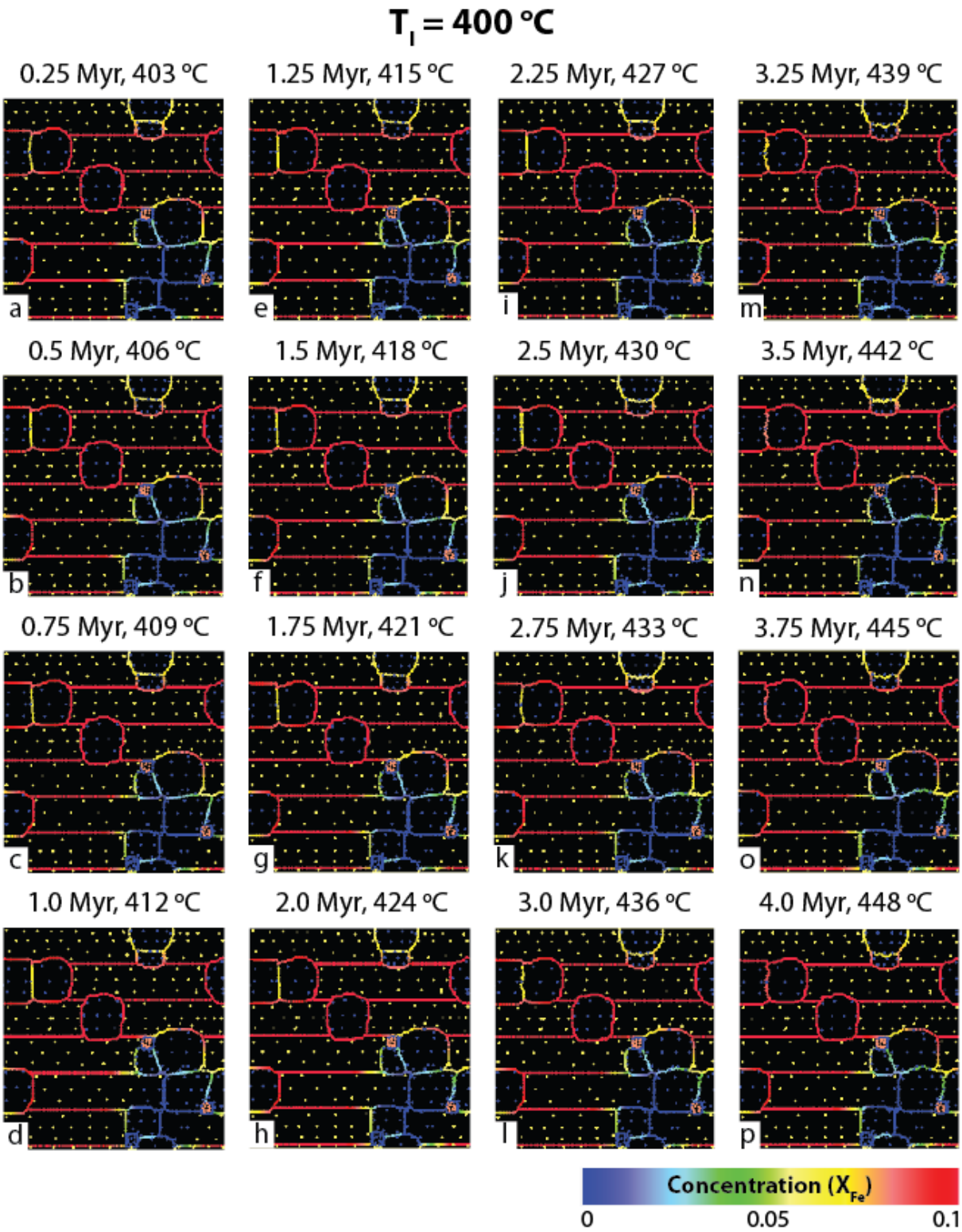

Figure A.6. Concentrations for Experiment 2 (starting temperature, T_I = 400 °C) for 0 - 4.0 Myr of diffusion. Each sequential image (a - p) represents an increase from the initial temperature by 3.0 °C per 0.25 Myr of diffusion (45 °C over 4.0 Myr).

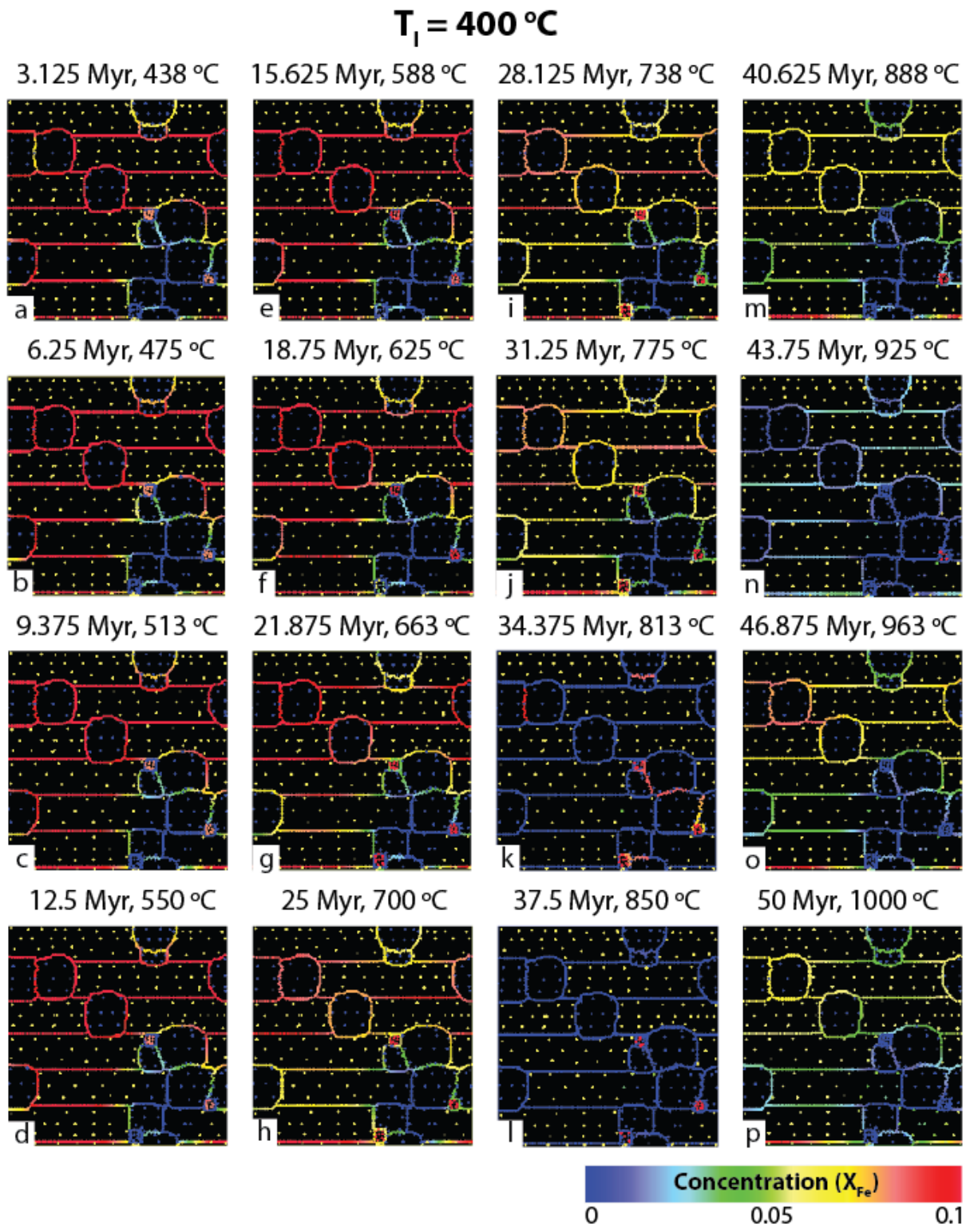

Figure A.7. Concentrations for Experiment 2 (starting temperature, T_I = 400 °C) for 0 - 50 Myr of diffusion. Each sequential image (a - p) represents an increase from the initial temperature by 38 °C per 3.125 Myr of diffusion (600 °C over 50 Myr).

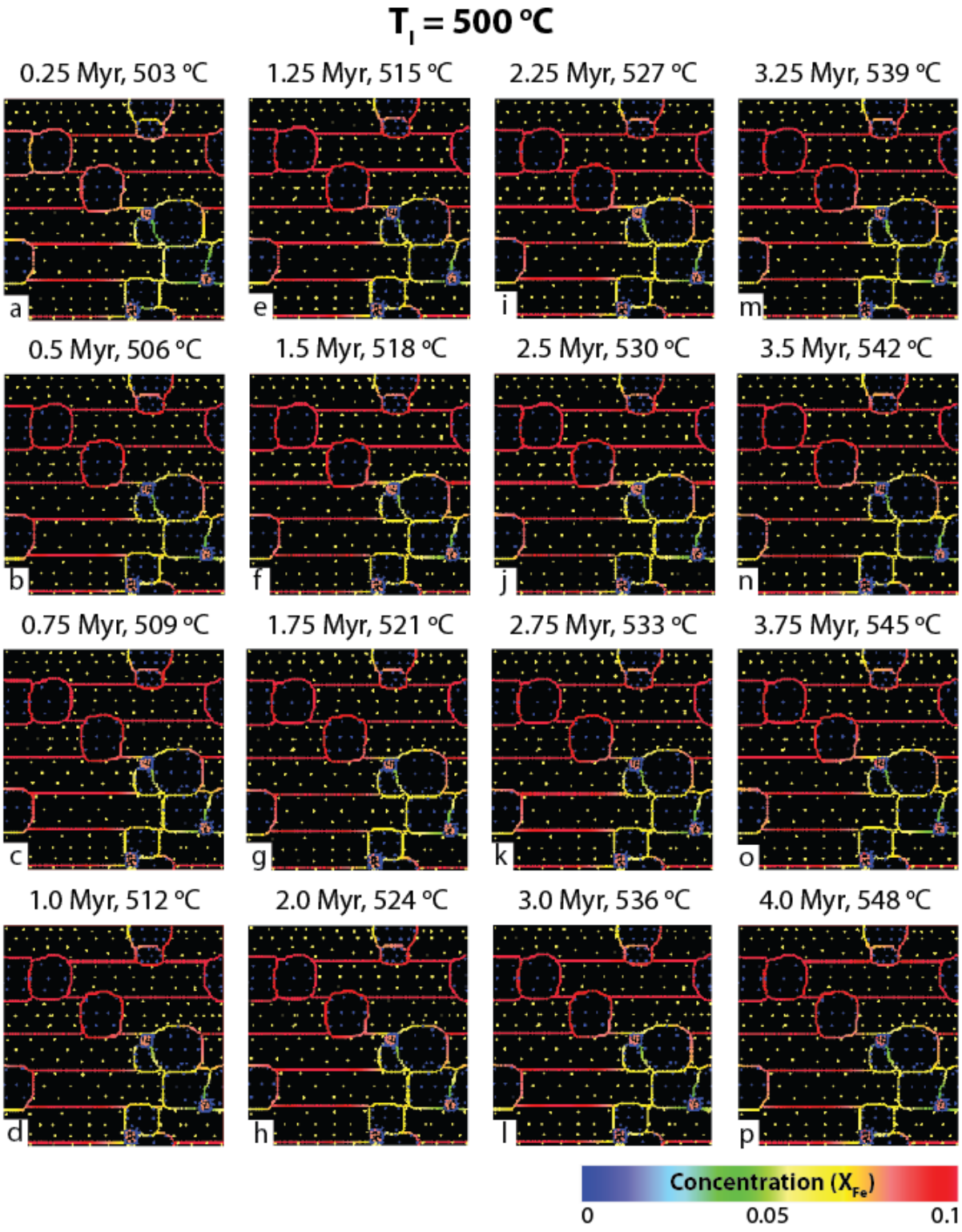

Figure A.8. Concentrations for Experiment 2 (starting temperature, T_I = 500 °C) for 0 - 4.0 Myr of diffusion. Each sequential image (a - p) represents an increase from the initial temperature by 3.0 °C per 0.25 Myr of diffusion (45 °C over 4.0 Myr).

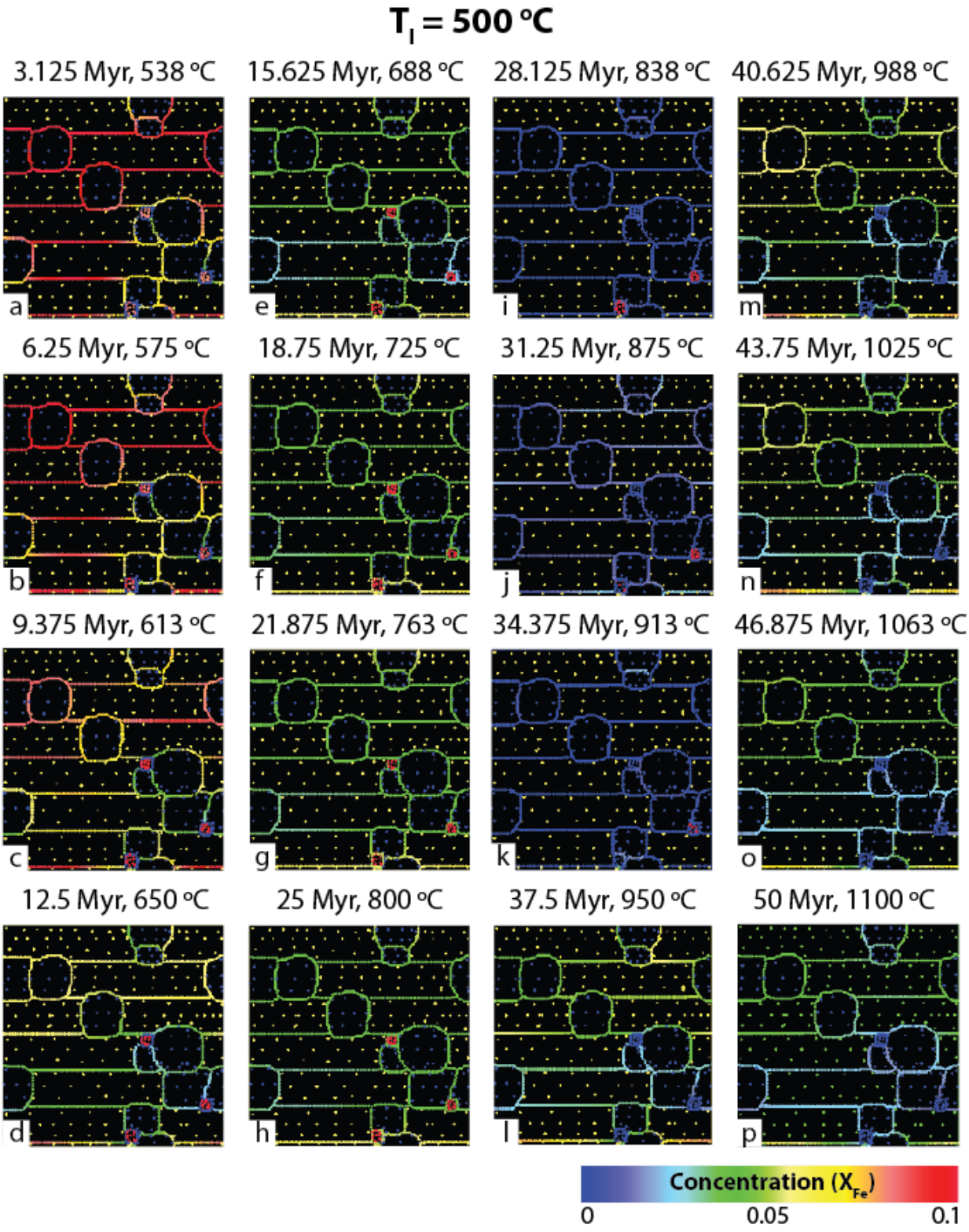

Figure A.9. Concentrations for Experiment 2 (starting temperature, T_I = 500 °C) for 0 - 50 Myr of diffusion. Each sequential image (a - p) represents an increase from the initial temperature by 38 °C per 3.125 Myr of diffusion (600 °C over 50 Myr).